Parsec and Sub-Parsec-Scale Structure and Evolution in Nearby Compact Radio Sources and Relationships to Emission at Other Wavelengths

Steven J. Tingay

A thesis submitted for the degree of

Doctor of Philosophy
of The Australian National University

Mount Stromlo and Siding Spring Observatories
The Institute of Advanced Studies
The Australian National University
Canberra, Australia

1996 May

Disclaimer

I hereby declare that the work in this thesis is that of the candidate alone, except where indicated below. The co-authors of resulting papers contributed to the text of those papers.

Chapters 3, 4, 5, 6, 7, and 8: The Southern Hemisphere VLBI Experiment team contributed to the observations of radio sources described in these chapters.
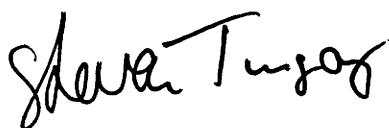
Chapter 3: The VLBI data from 1991 March 13 were correlated and calibrated by D.W. Hoard (JPL) and J.E. Reynolds (ATNF).

Chapter 4: The VLBI data for PKS 0208−512, PKS 0438−436, PKS 0521−365, PKS 0537−441, and PKS 0637−752 were correlated partly by T.D. van Ommen (JPL).

Chapter 5: Correlation of VLBI data from 1991 March 6, 1991 November 24, 1992 March 26, and 1992 November 22 was undertaken by T.D. van Ommen, M, St. John, and D.W. Hoard (JPL). Fringe-fitting of VLBI data from 1991 March 6, 1991 November 24 and 1992 March 26 was undertaken by D.W. Hoard, M. St. John, and D.L. Meier (JPL). Calibration of VLBI data from 1991 March 6 and 1991 November 24 was undertaken by J.E. Reynolds (ATNF).

Chapter 6: The calibration files for the VLBI observations were prepared by J.E. Reynolds. Part of the correlation of the VLBI data was undertaken by A.K. Tzioumis (ATNF).

Chapter 7: The 22 GHz Tidbinbilla observations were conducted by E.A. King (ATNF) and P. Harbison (British Aerospace Australia). The ATCA imaging observations were supervised by A. Koekemoer (MSSSO).

Steven John Tingay
May 1996

Acknowledgements

At the completion of this work I take great pleasure in thanking and acknowledging the people who have supported me over the eight years of my university education, and in particular the last four years.

I could not have started down this path without the support and understanding of my family and my wife. Their encouragement has enabled me to pursue my goals with vigour. I hope that they can take as much pleasure from this finished work as I do.

I thank my PhD thesis supervisor, Dr David L. Jauncey of the Australia Telescope National Facility. His guidance and insight has helped shape this work into what it is, and his careful proof reading of draft papers and the final thesis manuscript was very much appreciated. I am also grateful for the input of my advisor, Dr Geoffrey V. Bicknell of the Mount Stromlo and Siding Spring Observatories

I would like to thank the members of the Astronomical Measurements Group at the Jet Propulsion Laboratory in Pasadena, led by Dr Robert A. Preston. A substantial fraction of my time over the last 4 years has been spent at JPL, working in the AMG, without a doubt providing the most productive and enjoyable periods of my thesis.

Many other people have been involved in the work presented here, without whom the final results could not have been achieved. I refer here to the numerous people who have staffed the SHEVE telescopes over the last four years, changing tapes, making equipment work, and dealing with the logistics of getting an *ad hoc* VLBI array up and running a few times per year with a great deal of success. These people are too many to thank individually but Dr John E. Reynolds and Dr Anastasios K. Tzioumis deserve special mention; they are the driving force behind much of what happens in the SHEVE operation.

Finally, this work was supported financially by an Australian Postgraduate Award. Financial support for travel was provided by the Mount Stromlo and Siding Spring Observatories, the Jet Propulsion Laboratory, the Australia Telescope National Facility student program, and the Department of Industry, Science, and Tourism. I am grateful for the generous financial support of the organisers of the workshop "Jets from Stars and AGN" held in Bad Honnef, Germany, in particular Dr Wolfgang Kundt. Generous financial support provided by Dr Phillip Hardee allowed me to attend the workshop on "Energy Transport in Radio Galaxies and Quasars" in Tuscaloosa, USA. An IAU grant allowed me to attend IAU 175, "Extragalactic Radio Sources", in Bologna, Italy. These conferences and workshops have provided invaluable opportunities for me to present some of the results of my work and learn from the wider international community.

This research has made use of the NASA/IPAC Extragalactic Database (NED) which is operated by the Jet Propulsion Laboratory, California Institute of Technology, under contract with the National Aeronautics and Space Administration. Part of this research was carried out at the Jet Propulsion Laboratory, California Institute of Technology, under contract with the National Aeronautics and Space Administration.

Abstract

Presented here is the systematic Very Long Baseline Interferometry (VLBI) imaging study of extragalactic radio sources with $z < 0.06$, S_{VLBI} greater than 1 Jy, $\delta < 0°$, and $|b| > 10°$. This Southern Hemisphere investigation allows, for the first time, observations of a "Whole-Sky" sample of the nearest bright and compact radio sources to be assembled. The "Whole-Sky" sample defined here consists of 12 sources with $z < 0.06$, $S_{VLBI} > 1$ Jy, and $|b| > 10°$. Six of these sources lie in the Southern Hemisphere and are investigated in detail for the first time here.

In contributing 6/12 sources to a "Whole-Sky" sample of nearby, bright, and compact radio sources the two major aims of this thesis have been fulfilled:

1] To use VLBI observations to determine the parsec and sub-parsec-scale structure of these radio sources and to search for evolution at high spatial resolution.

2] To investigate the relationships between the structure/evolution of the compact radio sources and emission at other wavelengths.

Each of the six sources are discussed in detail, according to the two aims given above on a chapter-per-source basis, revealing a rich diversity in their VLBI properties and also in the properties of the host galaxies. In conclusion, the "Whole-Sky" sample is assembled and its VLBI characteristics are discussed.

Also included in this thesis is an extensive comparison between the VLBI properties of radio sources identified by the Energetic Gamma-Ray Experiment Telescope (EGRET) as sources of greater than 100 MeV gamma-ray emission and the VLBI properties of similar radio sources which have not been identified by EGRET. This investigation was motivated by the EGRET identification of PKS 0521−365 (one of the low red shift sources) and recent theoretical and observational efforts to understand the gamma-ray emission from AGN.

Finally, this thesis contains the detailed description of a VLBI imaging study of GRO J1655−40, the Galactic X-ray nova discovered in 1994 July.

Contents

List of Figures

List of Tables

Chapter 1

Introduction

1.1 Motivation

The work presented in this thesis was motivated by several considerations, the first being a practical one. By 1992, when this work was initiated, the Southern Hemisphere VLBI Experiment (SHEVE) array had been developed to the point at which it was operating at frequencies between 2.3 and 8.4 GHz, with up to seven stations participating in imaging experiments, and with maximum baseline lengths of close to 10,000 km yielding angular resolutions for imaging of less than one milliarcsecond (mas). The fact that the array was operating reliably and regularly meant that, for the first time, systematic, high quality imaging studies of compact radio sources could be undertaken from the Southern Hemisphere. At this time several projects were initiated, including an imaging survey of peaked-spectrum radio sources [King 1994], a survey of gravitational lens candidates [Lovell 1996], and the work presented here.

The scientific motivation for the study of a sample of nearby, bright, and compact radio sources was two-fold. Firstly, defining samples of compact radio sources, observing a representative number of them, and attempting to elucidate their properties is a well demonstrated tool for understanding the compact radio source population (e.g. Pearson & Readhead 1988; Polatidis *et al.* 1995). By choosing to study the brightest, nearest compact radio sources in the Southern Hemisphere, a "Whole-Sky" sample of such sources can be assembled for the first time. Since only a handful of these sources are accessible from each hemisphere, Southern Hemisphere VLBI observations are a valuable addition to the Northern Hemisphere observations which have been available for some time.

Secondly, for the purposes of investigating the detailed behaviour of individual sources, or classes of sources, rather than the gross properties of the entire source population, multi epoch and multi frequency campaigns aimed at single targets are required. The "Whole-Sky" sample consists of the brightest, nearest compact radio sources, providing unprecedented opportunities for parsec (pc) and sub-pc-scale spatial resolution VLBI imaging campaigns. Furthermore, because the radio sources are nearby, their host galaxies are generally prominent and well studied at radio wavelengths at arcsecond resolution, as well as at optical wavelengths, and even extending to X-ray and gamma-ray wavelengths.

Therefore, some unique opportunities exist to investigate the relationships between the compact structure of radio sources and their environments, thereby ob-

1

taining a view of the processes taking place in radio loud active galactic nuclei
(AGN) over many orders of magnitude in spatial scale.

1.2   Source selection

The nearby, bright, and compact radio sources can be put into the context of the
radio source population by considering the following.

The sample of 1 Jy extragalactic radio sources [Stickel, Meisenheimer, & Kühr
1994] contains 527 sources with 5 GHz flux densities greater than 1 Jy and $|b| > 10°$.
Of these sources 71/527 lie at red shifts less than z=0.06. At z=0.06, 1 mas is
approximately equivalent to 1 pc at the source, assuming a Hubble constant of 75
km/s/Mpc. Thus, VLBI observations of sources below this red shift allow sub-pc-
scale spatial resolution radio imaging

17/71 of these nearby sources are listed by Stickel, Meisenheimer, & Kühr [1994]
as having flat radio spectra; they are good candidates for being sources with flux
densities in excess of 1 Jy at VLBI resolution ($S_{VLBI} > 1$ Jy) since flat-spectrum
sources are likely to be core dominated.

On the other hand, 54/71 of the nearby sources are listed as having steep radio
spectra. These sources are not good candidates for $S_{VLBI} > 1$ Jy since they are
likely to be lobe dominated radio galaxies. To select $S_{VLBI} > 1$ Jy sources from
these 54 objects, core dominance parameters of $R < 0.33$ (ratio of core to extended
flux density) were adopted. Thus, steep-spectrum radio sources with a total flux
density > 4 Jy became candidates for $S_{VLBI} > 1$ Jy. For example, $R = 0.33$ and
$S_{TOTAL} = 4$ Jy corresponds to $S_{VLBI} = 1$ Jy; lower values of R are possible for
higher values of S_{TOTAL}, but it is unlikely that higher values of R (i.e. lower values
of S_{TOTAL}) are appropriate for lobe dominated sources. 12/54 of the nearby steep-
spectrum sources listed by Stickel, Meisenheimer, & Kühr [1994] have $S_{TOTAL} > 4$
Jy.

Thus, 29 of the 527 sources in the 1 Jy sample are candidates for $S_{VLBI} > 1$ Jy
and z < 0.06. A search of the literature was performed for these 29 sources and it
was found that 12/29 could unambiguously be shown to have $S_{VLBI} > 1$ Jy. These
12 sources consisted of 8/17 of the flat-spectrum sources and 4/12 of the steep-
spectrum sources, making up a "Whole-Sky" sample. In support of the selection
criteria for the steep-spectrum sources given above, the 4/12 steep-spectrum sources
found to have $S_{VLBI} > 1$ Jy have S_{TOTAL} of 681 Jy, 120 Jy, 15 Jy, and 12 Jy, all
well above the lower limit of 4 Jy.

Six of the 12 "Whole-Sky" sources were selected for study, those sources south
of $\delta = 0°$, over a period of three years with multi epoch and multi frequency VLBI
observations. Those six sources are listed in Table 1.1.

Additional sources have been studied during the course of this thesis, namely
sources used in the comparison between the VLBI properties of EGRET-identified
radio sources and the VLBI properties of similar sources which have not been
identified by EGRET. The sources included in the thesis for this purpose are listed
in Table 1.2 and their selection is discussed in chapter 4.

Finally, one more source was (unexpectedly, but happily) added to the scope of
this thesis. The radio source associated with the Galactic X-ray nova GRO J1655-
40 was discovered in 1994 August and subsequently investigated over a period of

four days with the SHEVE array. These observations provided the unique opportunity for a very high spatial resolution view of a rapidly evolving, relativistic Galactic jet.

Parkes Name	Alternate Name	z	$S(4.8)_{TOTAL}$	$S(4.8)_{VLBI}$	pc/mas
0518−458	Pictor A	0.035	15.45	1.1	0.7
0521−365	2EG J0524−3630	0.055	9.29	1.2	1.1
1322−427	Centaurus A	3.5 Mpc	681	5.5	0.02
	NGC 5128				
1514−241	AP Libræ	0.049	2.0	1.5	1.0
1718−649	NGC 6328	0.014	3.81	3.8	0.3
2152−699		0.028	12.28	1.2	0.6

Table 1.1: Six low red shift radio sources

Parkes Name	Alternate Name	z	$S(4.8)_{TOTAL}$	$S(4.8)_{VLBI}$	Gamma-ray Loud?
0208−512	2EG J0210−5051	1.003	3.31	2.5	√
0438−436		2.852	6.94	6.2	×
0537−441	2EG J0536−4348	0.894	4.00	3.3	√
0637−752		0.656	5.85	4.5	×
1921−293	OV−236	0.352	10.0	8.5	×

Table 1.2: Gamma-ray loud and quiet radio sources

1.3 Outline of thesis

In chapter 2, a brief theoretical introduction to the fundamentals of aperture synthesis is given, followed by a discussion of the SHEVE operation and the reduction path that SHEVE data takes.

In chapters 3 to 8, the observations of the radio sources are described in order of their right ascension. In chapter 3, the first multi epoch and multi frequency VLBI imaging observations of the low red shift FR II type radio galaxy PKS 0518−458 (Pictor A) are described and related to sub-arcsecond optical imaging observations from the Hubble Space Telescope (HST).

In chapter 4, multi epoch and multi frequency SHEVE observations of the radio galaxy PKS 0521−365 are described. Prompted by the identification of PKS 0521−365 by EGRET, an extensive comparison of the VLBI properties of EGRET-identified sources with the VLBI properties of similar radio sources not identified by EGRET has been made. Observations of PKS 1514−241, another of the low red shift sources, has been used in this study. Results from the comparison are also given in chapter 4.

In chapter 5, the most extensive VLBI observations of the closest active radio galaxy, PKS 1322−427 (Centaurus A, NGC 5128), are described. Multi frequency and multi epoch observations are described, as well as VLBI observations which utilised the SHEVE array in conjunction with the VLBA.

In chapter 6, SHEVE observations of the Galactic X-ray and radio source GRO J1655−40 are presented.

In chapter 7, the first VLBI imaging observations of the unusual low red shift radio galaxy PKS 1718−649 (NGC 6328) are discussed. A consideration of multi frequency data from optical to radio wavelengths, from the sub-pc-scale to the kpc-scale, show that this source is probably the lowest red shift example of a GHz Peaked-Spectrum radio source.

In chapter 8, the first VLBI imaging observations of the low red shift radio galaxy PKS 2152−699 are discussed. The relationships between the pc-scale radio source and the kpc-scale radio and optical structure of the galaxy are discussed and a model to explain the relationships is developed and presented.

Finally, in chapter 9, a summary of the properties of the Southern Hemisphere component of the "Whole-Sky" sample is given as well as a brief literature review of the properties of the Northern Hemisphere sources in the sample. Thus, for the first time, a "Whole-Sky" sample of nearby, bright, and compact radio sources is assembled and its VLBI properties described.

Chapter 2

Southern Hemisphere VLBI

2.1 Fundamentals of aperture synthesis

The technique of VLBI can be described by the fundamental equations of aperture synthesis as given by Clark [1995] and briefly outlined below.

If the electric field produced at a distant (celestial) source of radio emission is $\mathbf{E}(\mathbf{R}, t)$ then the frequency components of the time varying field can be designated $\mathbf{E}_\nu(\mathbf{R})$ and are complex quantities. $\mathbf{E}_\nu(\mathbf{R})$ are known as the *quasi-monochromatic components* of the electric field.

Radio source

$E_\nu(R)$

R

r

Earth
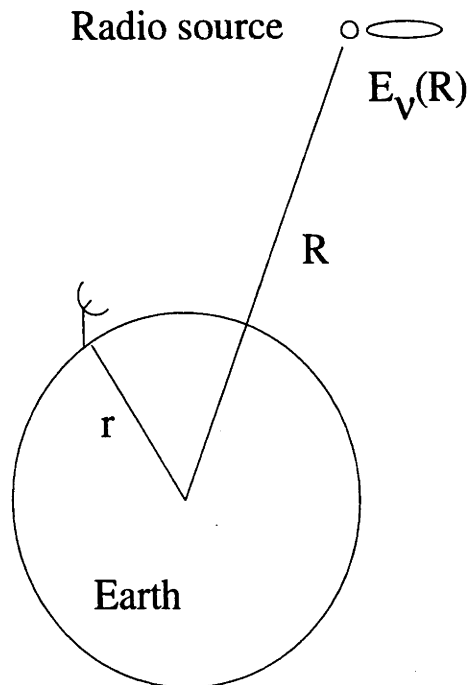
Figure 2.1: Radio source - antenna geometry

The linearity of Maxwell's equations allow each of the quasi-monochromatic components of the field from the source to be superposed at the observer. This superposition can be written as

$$\mathbf{E}_\nu(\mathbf{r}) = \int P_\nu(\mathbf{R}, \mathbf{r})\mathbf{E}_\nu(\mathbf{R})dS$$

(refer to Figure 2.1, adopted from Clark 1995). $P_\nu(\mathbf{R}, \mathbf{r})$ is the *propagator* which describes how the electric field at $\mathbf{R}$ influences the electric field at $\mathbf{r}$. P_ν is assumed to be an ordinary scalar function and through empty space P_ν takes a simple form, so that

$$\mathbf{E}_\nu(\mathbf{r}) = \int \frac{\mathbf{E}(\mathbf{R})e^{2\pi i\nu|\mathbf{R}-\mathbf{r}|/c}}{|\mathbf{R} - \mathbf{r}|}dS \ \ .$$

This is the quantity which is observable at a radio telescope. Among the properties of $\mathbf{E}_\nu(\mathbf{r})$ is the correlation of the field at two different locations in space,

$$\mathbf{V}_\nu(\mathbf{r}_1\mathbf{r}_2) = \langle \mathbf{E}_\nu(\mathbf{r}_1)\mathbf{E}_\nu^*(\mathbf{r}_2)\rangle \ \ .$$

Upon substitution of the expression for $\mathbf{E}_\nu(\mathbf{r})$ into the above equation and using the simplifying assumptions that the astrophysical radiation is not spatially coherent and that $|\mathbf{r}|/|\mathbf{R}| << 1$, the expression for the correlation of the electric field at two locations is

$$V_\nu(\mathbf{r}_1, \mathbf{r}_2) = \int I_\nu(\mathbf{s})e^{-2\pi i\nu\mathbf{s}(\mathbf{r}_1-\mathbf{r}_2)/c}d\Omega \ \ ,$$

where $\mathbf{s}$ is the vector from the point of observation to a point in the source and $I_\nu(\mathbf{s})$ is the surface brightness distribution of the radio source. $V_\nu(\mathbf{r}_1, \mathbf{r}_2)$ is known as the *spatial coherence function* of the field and is the quantity measured by radio interferometers. The above expression can, within well defined limits, be Fourier inverted so that the measurement of V_ν allows an estimate of I_ν. This is the fundamental premise of aperture synthesis.

One further simplifying assumption can be made so that the expression for the spatial coherence function can be cast in a more convenient form for Fourier inversion. This assumption is that the radio source is of small angular size and that the vector $\mathbf{s}$ can be expanded as $\mathbf{s} = \mathbf{s}_0 + \sigma$, where $\mathbf{s}_0$ is a fixed unit vector in the direction of the source, and σ is a perpendicular vector in the plane of sky which describes each point in the radio source.

A suitable coordinate system can be chosen for the interferometer baselines connecting the pairs of locations at which V_ν is measured, (u, v), as well as a suitable coordinate system for the plane of the sky, (x, y) [Clark 1995]. The interferometer baselines do not necessarily lie within the $u - v$ plane. It is the projection of the physical baseline into the $u - v$ plane which is important and defines the baseline which measures the spatial coherence function of the electric field. For an array of radio telescopes spanning the Earth, $V_\nu(u, v)$ can be measured for many points in the $u - v$ plane by observing over a period of time. As the Earth rotates, the baselines of a given array, as projected into the $u-v$ plane, change their orientation and length, sampling different points of the $u - v$ plane. $u, v, x,$ and y are related in the new, simplified expression for V_ν,

$$V_\nu(u, v) = \int\int I_\nu(x, y)e^{-2\pi i(ux+vy)}dxdy \ \ .$$

When inverted, the above expression for $V_\nu(u,v)$ becomes:

$$I_\nu(x,y) = \int\int V_\nu(u,v)e^{2\pi i(ux+vy)}dudv \quad .$$

However, since an array of radio telescopes forming a set of interferometers does not measure V_ν at all points in the $u-v$ plane, but only discretely, a sampling function, $S(u,v)$, must be introduced,

$$I_\nu^D(x,y) = \int\int S(u,v)V_\nu(u,v)e^{2\pi i(ux+vy)}dudv \quad .$$

I_ν^D is referred to as the *dirty image*. It is related to the true brightness distribution of the radio source as follows:

$$I_\nu^D = I_\nu * B \quad ,$$

where B is known as the *dirty beam*, the Fourier transform of the sampling function,

$$B(x,y) = \int\int S(u,v)e^{2\pi i(ux+vy)}dudv \quad .$$

The true brightness distribution, I_ν, can then be obtained from I_ν^D and B by deconvolution.

2.2 Observing with SHEVE

The SHEVE array is an *ad hoc* array of radio telescopes in the Southern Hemisphere. The facilities which make up and support the array are owned and operated by several independent institutions. Thus, operation of the SHEVE array is based heavily on collaboration and cooperation between these institutions. The first SHEVE observations were made in 1982 [Preston *et al.* 1989; Meier *et al.* 1989; Tzioumis *et al.* 1989; Jauncey *et al.* 1989]. In Tables 2.1, 2.2, and 2.3, a brief summary of the array is given, including the telescopes which regularly participate and their characteristics (further information is available on the World Wide Web, http://wwwatnf.atnf.csiro.au).

An open proposal system is in place for obtaining observing time with the SHEVE array, administered by the Australia Telescope National Facility (ATNF). SHEVE observations are generally made three or four times per year, each session typically of one to two weeks in duration. Due to the collaborative nature of the SHEVE operation each investigator is required to participate in the observations, as well as be responsible for processing the results of the observations they propose.

Up until 1994 all SHEVE observations were made using either the narrow bandwidth Mark II VLBI recording system [Clark 1973] or the wide bandwidth Mark III VLBI recording system [Rogers *et al.* 1983]. Imaging observations utilised the Mark II setup since all telescopes were equipped for Mark II. Mark III VLBI observations are generally only utilised for astrometric or geodetic observations (e.g. Reynolds *et al.* 1994) since only a subset of the SHEVE telescopes are equipped with Mark III recorders. Seven of the SHEVE telescopes are equipped with Hydrogen masers as the frequency standard for VLBI observations. The remaining telescopes are equipped with Rubidium clocks, as indicated in Table 2.3.

Location	Longitude East (°)	Latitude geodetic (°)	Elevation (m)
Narrabri	149.57	-30.31	217
Mopra	149.07	-31.30	1164
Parkes	148.26	-33.00	392
Tidbinbilla (DS 43, 70 m)	148.98	-35.40	670
Hobart	147.44	-42.80	100
Perth (ESA 15 m)	115.89	-31.80	55
Hartebeesthoek	27.67	-25.89	1391

Table 2.1: SHEVE antenna locations

	Narrabri	Mopra	Parkes	Tid.	Hobart	Perth	Hart.
Narrabri	...	119	322	567	1396	3173	9847
Mopra	119	...	203	455	1283	3108	9781
Parkes	322	203	...	275	1089	3009	9665
Tid.	567	455	275	...	832	3053	9588
Hobart	1396	1283	1089	832	...	3001	9168
Perth	3173	3108	3009	3053	3001	...	7797
Hart.	9847	9781	9665	9588	9168	7797	...

Table 2.2: SHEVE baseline lengths in km

Telescope (Institute)	Diameter (m)	Mount	Elev. Limit°	T_{sys} (Jy) at ν (GHz) 2.3	4.8	8.4	Frequency Standard
Narrabri (ATNF)	22	AZEL	12	400	45	400	Rb
Mopra (ATNF)	22	AZEL	12	350	45	400	Maser
Parkes (ATNF)	64	AZEL	30	90	80	90	Maser
Tid. (DSN)	70	AZEL	6	15	-	20	Maser
Tid. (DSN)	34	AZEL	8	165	-	130	Maser
Tid. (DSN)	34	HADEC	10	100	-	130	Maser
Hobart (U. Tas.)	26	XYEW	16	650	1200	750	Maser
Perth (ESA)	15	AZEL	10	3300	-	4000	Rb
Perth (Telstra)	27	AZEL		-	1400	-	Rb
Hart. (HRAO)	26	HADEC	10	45	56	60	Maser

Table 2.3: SHEVE antenna characteristics

All of the Mark II data obtained for the work included in this thesis were recorded with a single sideband and a single circular polarisation, according to IEEE convention. The standard observing frequencies were used: 2.290, 4.851, and 8.418 GHz, with RCP, LCP, and RCP respectively.

The SHEVE array recording system has recently been upgraded to the S2 system [Wietfeldt *et al.* 1991] which uses a low-cost recording medium and hardware similar to the Mark II system but has a much larger recorded bandwidth. Most future SHEVE observations will be made with the S2 system.

2.2.1 Observations of the sample

In each of chapters 3 to 8 the dates and details of the SHEVE observations made for this thesis are given.

2.2.2 Correlation

For VLBI observations the individual elements of an array are not connected in real time; $V_\nu(u,v)$ cannot be measured as the observations are taking place. It is the task of the *correlator* to recreate the conditions of an observation after the event, so as to allow the data recorded at each array element to be combined, thus forming $V_\nu(u,v)$ (e.g. Romney 1995). The Mark II data recorded on VHS video tapes at each of the SHEVE antennae were correlated at the Caltech/JPL Block II VLBI processor at Caltech, in Pasadena, California.

The Block II processor is a lag correlator. The digital data streams recorded on tape are aligned by the correlator using recorded time signals. The correlator calculates the geometric and tropospheric delay and the phase rotation as a function of time, according to a correlator model which incorporates accurate source positions, antennae positions, observing frequencies, observation epochs, and sidebands in a correlator control file. The correlator applies the appropriate delay and phase rotation to the data streams and forms the correlation of pairs of data streams for a number of values of delay. A 4 MHz sampling rate is used to fulfill the Nyquist theorem for the 2 MHz recorded bandwidth of the Mark II system. Each increment in delay, or lag, at the Block II processor is therefore $1/4$ μs.

To correlate the SHEVE observations the correlator was used in two modes. First, to find the interferometer fringes on each baseline, the correlation was examined over a wide range in delay (64 μs = 256 delay lags) on one baseline at a time. The fringes were found at different times during an experiment, allowing drifts in the fringe delay due to changes in the time standards at each of the antennae to be followed. This pass through the data at the correlator is known as "determining the clocks". During this step rough residual fringe rates were also determined. Once the clocks were determined that information was added to the correlator model, in the correlator control file.

"Determining the clocks" is a very important step in the SHEVE data reduction process since Rubidium clocks are used as frequency standards at some of the SHEVE stations. Rubidium clocks are not as stable as Hydrogen masers and can undergo fast drifts. Also, significant jumps are not uncommon. Therefore, for each SHEVE experiment, fringes were found at two or three points per 24 hour period

for the purpose of "determining the clocks". If clock jumps existed, the precise points in time that the jumps took place were determined.

The second correlator mode was then used to correlate the data streams from all antenna pairs, N(N-1)/2 baselines, simultaneously (with some redundancy). Because the clocks had been determined it was only necessary to form the correlations over a small range in delay (2 μs = 8 delay lags), enough to contain the fringes at all times during the correlation. The correlator integrated the correlated signal and output to a file data for each of the eight values of delay every two seconds.

2.2.3   Fringe-fitting

The output from the correlator was converted into the Flexible Image Transport System (FITS) format, using the B2FITS task of the Caltech VLBI package [Pearson 1991] and then taken into the National Radio Astronomy Observatory (NRAO) Astronomical Image Processing Software (AIPS) reduction package for further processing. The first processing task was to accurately determine the amplitude and phase of the fringes at each of the 2 second correlator periods. This process is known as fringe-fitting. Fringe-fitting algorithms search for and remove any residual fringe rate from the data so that the fringes can be integrated in time, allowing an accurate amplitude and delay to be obtained. The delay on the $i - j$ baseline, τ_{ij}, is directly related to the baseline phase, ϕ_{ij},

$$\phi_{ij} = 2\pi\nu\tau_{ij} .$$

The amplitudes and phases determined by fringe-fitting are the (somewhat corrupted) real and complex components of the visibility function, V, in § 2.1.

The fringe-fitting task FRING in the AIPS package has been used to fringe-fit all of the SHEVE observations correlated at the Block II processor. During fringe-fitting, any information on the absolute phases of the visibility function was sacrificed in favour of increasing the sensitivity to weak fringes on some baselines. The powerful technique of global fringe-fitting was implemented to achieve this [Schwab & Cotton 1983]. In global fringe-fitting the residual phase rates are separated into antenna based components which satisfy closure relations around sets of three or more antennae. A rudimentary model for the source structure is therefore required for this method to proceed, a single point source being sufficiently accurate for most applications. Thus, from the detection of fringes on sensitive baselines the fringe rate can be predicted for the less sensitive baselines, giving a better chance for the detection of weak fringes on those baselines.

Any information on the absolute phase of the visibility function is lost since, with this method, the phase on a designated reference antenna is set to zero during each period that the fringe rate is evaluated. All baseline phases are determined relative to the reference antenna.

After fringe-fitting, the fringe amplitude and fringe phase relative to the reference antenna exist at each 2 second correlator output interval. For a 12 hour observation with 5 or 6 antennae this usually produced a file of the order of several megabytes in size. This FITS format file was then converted into the MERGE format, standard for the Caltech VLBI package tasks. To reduce the size of the dataset and to improve signal to noise, the data were integrated coherently over a

30 second period, well within the coherence time typical for SHEVE observations [King 1994]. This was achieved with the Caltech package task AVERAGE, using a coherent average and with errors derived from the scatter in the amplitudes and phases.

At this point the data were edited of bad visibilities. Editing was achieved within DIFMAP [Shepherd, Pearson & Taylor 1994] or with the Caltech task IED. Occasionally the task of editing on some baselines was a substantial one since the Rubidium frequency standards are not as robust at the higher frequency of 8.4 GHz as at 2.3 or 4.8 GHz.

2.2.4   External calibration

Following the completion of each SHEVE experiment, a file containing the logged system temperatures, T_{Si}, from each antenna was produced in the format required by the Caltech calibration task CAL. The file also contained nominal values for the antenna gains, g_i, and the correlator dependent constant, b. This *a priori* calibration information was then applied to the averaged and edited amplitudes output from the correlator for calibrator sources. The relationship between the correlated flux density, S_{Cij}, on the i - j baseline, and the correlated amplitude, ρ_{ij}, is [Cohen *et al.* 1975]

$$S_{Cij} = b\rho_{ij}\sqrt{\frac{T_{Si}}{g_i}\frac{T_{Sj}}{g_j}} \quad .$$

The SHEVE calibrator sources are known to be unresolved on most of the Australian SHEVE baselines, with little extended structure on arcsecond scales.

The total flux densities of the calibrators were measured during the course of each SHEVE experiment and compared to the calibrated VLBI flux densities. For most experiments the *a priori* calibration put the VLBI flux density of the calibrator within 10% of its total flux density. For some experiments larger deviations were present on some baselines, usually due to departures from the nominal system characteristics. When this was the case, antenna based corrections were derived from the calibrator observations using amplitude closure relations and added to the calibration file as an improvement on the *a priori* calibration. The refined calibration file was then applied to the raw correlated amplitudes of the target sources to produce calibrated amplitudes. The overall flux density accuracy of the data presented in this thesis is approximately 10%.

2.2.5   Imaging and internal calibration

Once the data had been averaged and edited of bad points and the visibility amplitudes calibrated it was used to produce an estimate of the surface brightness distributions of the radio sources, partly via the equations listed in § 2.1.

A major obstacle in applying the equations of aperture synthesis to VLBI data is that while the visibility amplitudes can usually be calibrated with an accuracy of better than 10%, it is not possible to calibrate the visibility phases in an absolute sense. The external methods of calibrating phase with a connected element interferometer do not apply to VLBI observations, as each antenna possesses a completely independent frequency standard.

Thus, the phases from the fringe-fitting process are not absolute phases and appear quasi-random in time. The only well behaved properties of the phases are their closure relations [Jennison 1958; Rogers 1974]. The relation between the measured baseline phase and the true baseline phase is [Pearson & Readhead 1984]

$$\phi_{mn} = \psi_{mn} + \theta_m - \theta_n + \epsilon_{mn} \quad ,$$

where ϕ_{mn} is the observed phase, ψ_{mn} is the true phase, θ_m and θ_n are the antenna dependent phase errors, and ϵ_{mn} is the noise in the measurement on the $m - n$ baseline. If the closure phase,

$$\Psi_{lmn} = \phi_{lm} + \phi_{mn} + \phi_{nl} \quad ,$$

is formed then it can be seen that

$$\Psi_{lmn} = \psi_{lm} + \psi_{mn} + \psi_{nl} + \epsilon_{lm} + \epsilon_{mn} + \epsilon_{nl}$$

depends upon the true phases, degraded only by noise. A somewhat similar closure relation also exists for visibility amplitudes [Pearson & Readhead 1984].

A method for the internal calibration of the visibility phases is generally utilised so that the visibility function can be reconstructed and used to produce images of the source structure. This internal calibration method relies heavily on the visibility closure phases and is known as self-calibration [Pearson & Readhead 1984]. The method proceeds as follows: an approximate model for the source structure is guessed, usually from an inspection of the visibility amplitudes. The closure phase information from the data, augmented by phases predicted from the approximate model are used to form a complete set of visibility phases which, along with the measured visibility amplitudes, can be inverted to produce a dirty image of the source. A deconvolution algorithm is then used to subtract copies of the dirty beam from the dirty image, producing a set of point sources which is a better representation of the source structure. This new representation of the source structure can then be used to generate a new set of visibility phases which, in turn, can be used to produce a new dirty image, a new source model, new visibility phases, etc. Thus, imaging using self-calibration is an iterative procedure, eventually converging to the point where new inversions of the data do not improve the quality of the image. Details of self-calibration imaging, the various deconvolution techniques and image restoration techniques can be found in the review by Pearson and Readhead [1984].

For the SHEVE data presented in this thesis, self-calibration techniques, as implemented in the DIFMAP imaging software [Shepherd, Pearson & Taylor 1994] have been used to produce the VLBI images. DIFMAP uses a difference mapping algorithm which de-convolves regions of the dirty image specified by the user and accumulates a list of point sources which represents the source. As the dirty image is de-convolved the list of point sources grows and the user is left with a residual dirty image, the difference between the original dirty image and the accumulated point sources. DIFMAP allows the dirty image to be de-convolved and self-calibrated in a piecewise manner, in a way which is easy to visualise and which allows the outcomes of different choices of imaging procedure to be explored efficiently.

This last point is very important for the imaging analysis of SHEVE data. The SHEVE array generally operates with between 4 and 7 antennae. The inner $u - v$

coverage of the array is generally concentrated in a north-south direction, due to the geographic locations of the antennae within Australia, and large gaps can exist within the outer $u - v$ coverage if Hartebeesthoek data is retained. This can make imaging difficult. To ensure that the images in this thesis are good representations of the source structures, careful analyses were made of all of the data sets, according to a basic imaging philosophy; the images should be as simple as possible and still model the data very well, and each dataset should be imaged on its merits, with any *a priori* knowledge of the source structure not influencing the choices made during imaging. The imaging choices made in producing each image in this thesis were, therefore, as follows:

- A uniform weighting scheme was employed for data in the $u - v$ plane.

- Pixel sizes between 0.1 and 2 mas and map sizes between 512 and 1024 pixels were used throughout. The particular combination of pixel and map size depended on the extent of the $u - v$ coverage for the observation.

- Initially the visibility phases were self-calibrated with a 1 Jy point source.

- The dirty image and consequently the residual dirty images were de-convolved using iterations of 100 cleans with a loop gain of 0.1. Windows were initially set tightly around the brightest region of emission.

- Phase self-calibration and cleaning proceeded. Gradually the number of clean windows was increased to incorporate more of the source emission, until the total flux density in the source model was comparable to the visibility amplitudes.

- An amplitude self-calibration was performed, generating a single amplitude correction for each antenna and applying it to the data. Generally the amplitude self-calibration significantly reduced noise in the residual image due to errors in the *a priori* flux density calibration, allowing more emission to be cleaned from the clean windows and further phase self-calibration to be performed.

- Eventually, more amplitude self-calibration was performed over shorter time-scales, so as to remove short time-scale variations in the amplitude gains. These further amplitude self-calibrations were always accompanied by one or more iterations of phase-only self-calibration. The last amplitude self-calibration was performed on the data at each $u - v$ point.

Many trial maps of each dataset were produced, exploring slightly different sequences of phase and amplitude self-calibration, and windowing. In all cases it was found that the results of imaging were repeatable, and not sensitive to small changes.

Having obtained the final images for each of the sources, specific analyses of the images could be made. The analyses particular to a given source are discussed in the relevant chapter.

Chapter 3

Pictor A, a powerful, low red shift radio galaxy

3.1 Introduction

PKS 0518−458 (Pictor A) is the nearest Fanaroff-Riley [1974] type II radio galaxy with a broad-line optical spectrum (d∼140 Mpc, $1''$∼700 pc, 1 mas∼0.7 pc since z=0.035 and adopting H_o=75 km/s/Mpc). The large-scale radio source has the classic characteristics of FR II type radio galaxies, with two edge-brightened lobes of radio emission, separated by approximately 290 kpc, straddling the radio core which is coincident with the optical galaxy [Thompson, Crane, & MacKay 1995]. The lobe hot spots are connected along a position angle of approximately 102°. Simkin, Sadler, and Sault [1994] have reported the detection of a kpc-scale jet connecting the core to the western hot spot.

The western hot spot itself contains a compact radio source and has been detected at optical wavelengths. The radio and optical morphology is complex and the optical emission is highly polarised [Thompson, Crane, & MacKay 1995].

The optical galaxy has been extensively studied and is notable for its strong, low ionisation, broad emission line spectrum which is variable. Sulentic *et al.* [1995] report dramatic variations in the strength and appearance of the Balmer lines.

The core of the radio source has been little studied, in comparison to the large-scale radio structure. Jones, McAdam, and Reynolds [1994] found Pictor A to have the second highest core flux density in their sample of radio galaxies, the source with the brightest core being Centaurus A. Jones, McAdam, and Reynolds [1994] found the Pictor A core to be unresolved on the Parkes to Tidbinbilla baseline of 275 km with a flux density of approximately 1.1 Jy at 8.4 GHz and a spectral index between 2.3 and 8.4 GHz of $\alpha = -0.06$ ($S_\nu \propto \nu^\alpha$).

This chapter contains a description of the first VLBI imaging investigation of the radio core of this powerful, low red shift radio galaxy.

3.2 Observations and data reductions

The SHEVE observations of Pictor A were obtained and processed as described in chapter 2. Table 3.1 contains a summary of the observations.

Figure 3.1 shows the image of Pictor A obtained from the data of 1991 March

Epoch	frequency (GHz)	Participating Telescopes
1991 March 12	2.3	Ds43,Pk,Hb,Na
1993 Feb. 18	8.4	Ds43,Pk,Hb,Na,Mr,Ht
1993 July 3	8.4	Ds43,Pk,Hb,Na,Mr,Pr15,Ht

Table 3.1: Observation log for PKS 0518−458.
Ds43 = Tidbinbilla (70 m), Pk = Parkes, Hb = Hobart, Na = Narrabri,
Mr = Mopra, Pr15 = Perth (15 m), Ht = Hartebeesthoek

12, at 2.3 GHz. The source consists of a component which is extended toward the west at a position angle of approximately −77°. Figure 3.2 is an image resulting from observations on 1993 February 18 with a similar array of telescopes but with a higher resolution due to the higher observing frequency of 8.4 GHz. The bright component apparent at the eastern end of the source, when Figures 3.1 and 3.2 are compared, can be identified as the flat-spectrum core. In addition a jet-like structure extends to the west at a position angle of −79°.

Figure 3.3 is an image produced from the data of 1993 July 3, at 8.4 GHz, but with resolution higher than Figure 3.2 due to the longer baselines to Perth available in the array for this observation. The core is again the brightest feature in the image and the jet is well resolved, revealing an extension from the core at a position angle of approximately −74°, with an angular length of approximately 7 mas, and a discrete component approximately 11 mas from the core, along the same position angle.

That the features in Figure 3.3 are real is supported by the fact that if the clean component model of Figure 3.3 is convolved with the restoring beam of Figure 3.2 then the reconvolved image and Figure 3.2 are identical.

The mismatch in frequency and resolution between the 2.3 GHz observations of 1991 March 12 and the 8.4 GHz observations in 1993 do not allow any meaningful investigation of evolution in the pc-scale radio source over this period. The comparison of 8.4 GHz data between the 4.5 months 1993 Feb 18 to 1993 Jul 3 indicates that no significant structural change could be detected on that time-scale.

The data on baselines to Hartebeesthoek at 1993 February 18 and 1993 July 3 were sparse and not used during the imaging process. However, a significant detection of the source was made on both occasions. Approximately 0.2 Jy were detected on the Tidbinbilla to Hartebeesthoek baseline on 1993 July 3, corresponding to an angular resolution of approximately 0.4 mas. Thus, a rough estimate of the radio core brightness temperature is 2×10^{10} K at 8.4 GHz.

One additional analysis of the data was made for the 2.3 GHz observations of 1991 March 12. During the correlation of the data, an attempt was made to correlate at the position of the radio hot spot in the western lobe since the hotspot was known to be compact at radio wavelengths, as seen in recent VLA images [Thompson, Crane, & MacKay 1995]. Fringes were detected at the position of the hot spot but it could not be ruled out that these fringes were simply side lobes in the delay beam as a result of the narrow bandwidth of the Mark II VLBI system.

0518−458 observed at 2.291 GHz, 1991 Mar 12
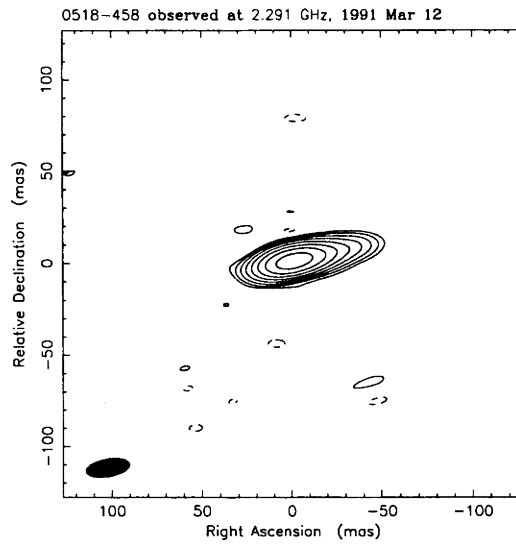
Figure 3.1: Map peak, 1.0 Jy/beam. Contours, -0.5, 0.5, 1, 2, 4, 8, 16, 32, and 64% of peak. Beam FWHM, 24.5×9.7 mas @ -80°.

0518−458 observed at 8.421 GHz, 1993 Feb 18
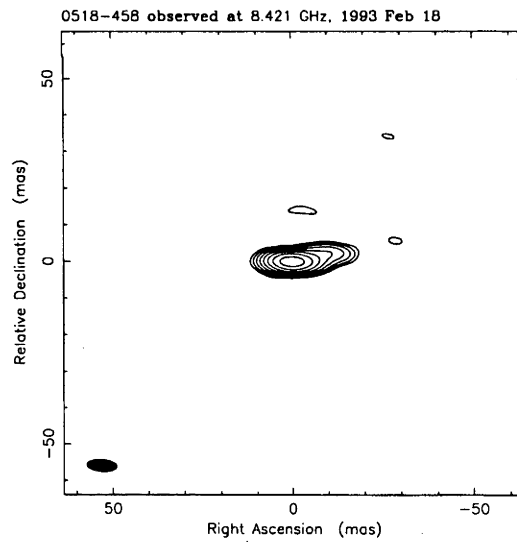
Figure 3.2: Map peak, 0.8 Jy/beam. Contours, 0.5, 1, 2, 4, 8, 16, 32, and 64% of peak. Beam FWHM, 8.2×3.3 mas @ 86°.
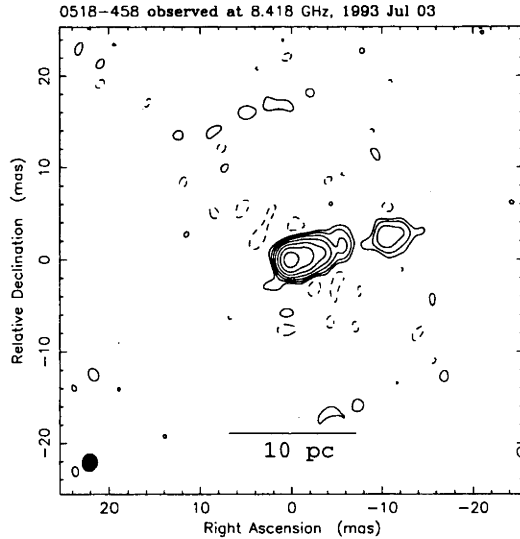
Figure 3.3: Map peak, 0.3 Jy/beam. Contours, -1, 1, 2, 4, 8, 16, 32, and 64% of peak. Beam FWHM, 1.9×1.6 mas @ -8.6°.

3.3   Discussion

The SHEVE observations have shown that the compact source at the nucleus of Pictor A has a core-jet structure approximately 10 pc in extent. A flat-spectrum core lies at the eastern end of the structure and a steep-spectrum jet extends toward the west, highly aligned with the kpc-scale jet and the western radio hotspot. In the highest resolution image the jet is resolved into an inner continuous jet and a detached component. Future VLBI observations of comparable quality and resolution will make an investigation of evolution in the pc-scale source possible.

Regardless, the pc-scale radio structure of Pictor A can be compared with existing high resolution optical observations.

The pc-scale core-jet radio structure aligns with a sub-arcsecond optical jet reported by Simkin, Robinson, and Sadler [1992] from narrow band HST imaging. They found that [OIII] emission from the narrow line region of the Pictor A host galaxy is distributed in a roughly symmetrical fashion around the nucleus, while the line-free continuum takes the form of an elongated, jet-like structure aligned with the western radio lobe. They measure the optical jet to have dimensions of 50×220 mas.

On one hand, the coincidence of the optical jet with the pc-scale radio jet supports the suggestion of Simkin, Robinson, and Sadler [1992] that the optical jet is due to synchrotron emission.

However, the optical jet appears to be much more extended than the pc-scale radio jet seen with VLBI. Figure 3.1 shows that the radio jet extends only approximately 50 mas whereas the quoted length of the optical jet is in excess of 200 mas. Given that the electrons responsible for optical synchrotron emission are much shorter lived than those responsible for radio synchrotron emission it is not clear that the optical jet can be more extended than the radio jet. In fact a very

good correspondence between radio and optical jets has been established, at least on kpc-scales. HST and radio imaging of the radio/optical jets in Virgo A and PKS 0521−365 [Sparks, Biretta, & Macchetto 1994; Macchetto *et al.* 1991] show a strong coincidence between the jet structure at radio and optical wavelengths.

To show that the VLBI observations were not biased towards measuring a jet shorter than in reality, Figure 3.4 shows an image produced from simulated data. The data were simulated from the Caltech VLBI task FAKE using a source model which consisted of a 5 mas full width at half maximum (FWHM) circular Gaussian core component of 0.4 Jy and a 200 mas long and 50 mas wide constant surface brightness elliptical component of 0.7 Jy, orientated at a position angle of −77°. The source was given the RA and DEC of the Pictor A nucleus and "observed" at 2.290 GHz with the array of telescopes used on 1991 March 12. Realistic values for system temperatures, antenna diameters and antenna pointing were used to generate noise in the data. In Figure 3.4, the jet component can be easily detected to its full 200 mas extent, showing that the observations of 1991 March 12 would have been sensitive to a jet with the extent of the optical jet reported by Simkin, Robinson, and Sadler [1992].
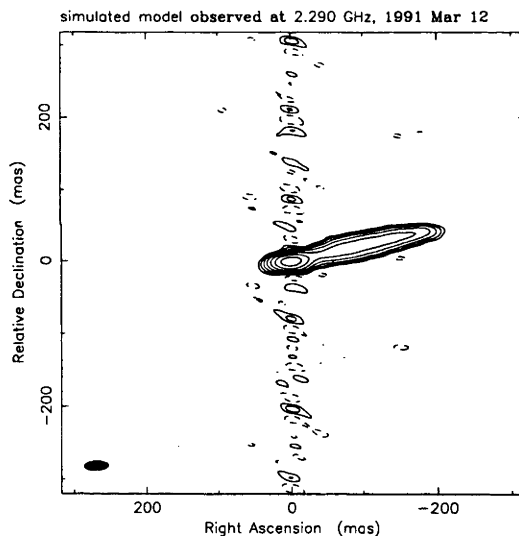
Figure 3.4: Map peak, 0.4 Jy/beam. Contours, -1, 1, 2, 4, 8, 16, 32, and 64% of peak. Beam FWHM, 32.5×13.3 mas @ -87.1°.

Thus, based on a simple synchrotron interpretation, the relationship between the VLBI observations and the HST observations is difficult to understand. A second epoch observation, with the post COSTAR HST, of the optical jet will be required before a detailed comparison between the optical and VLBI observations can be made.

The HST has also been used to observe the western hotspot, the site of inter-action between jet and inter galactic medium (IGM), at optical wavelengths. Even though the results of the attempt to detect the hotspot of Pictor A with VLBI, described in § 3.2, were ambiguous, Pictor A remains one of the best candidates for such a detection. Thompson, Crane, & MacKay [1995] present a VLA image of the western hotspot in Pictor A which reveals radio emission unresolved with a

0.″8×0.″2 beam. This emission should be detectable and imagable with 2.3 GHz VLBI observations utilising an array similar to that used for Figure 3.1. With the higher bandwidth of the S2 VLBI system a better sensitivity to the hotspot emission will be possible. The resulting images would give a view of the interaction between the jet and IGM at a resolution comparable to the HST observations. These observations have been proposed as future SHEVE experiments.

As one of the closest powerful radio galaxies, Pictor A will be an important target for future investigations with VLBI and at other wavelengths. Observations of the compact radio core of Pictor A with the VLBI Space Observatory Programme (VSOP) space VLBI mission may be feasible. As an FR II radio galaxy with a bright core it offers one of the best prospects for the investigation of a misaligned and non beamed radio jet with the long baselines provided by the upcoming space VLBI missions.

Chapter 4

Compact radio sources and γ-ray emission

4.1   Introduction

The first two dedicated gamma-ray astronomical satellites, *SAS 2* and *COS B*, yielded between them one identified extragalactic source of greater than 100 MeV gamma-rays, the radio source 3C273 [Bignami & Hermsen 1983]. The *Compton Gamma-Ray Observatory* (*CGRO*) was launched in 1991 April. Of the four detectors on board the Observatory, the Energetic Gamma-Ray Experiment Telescope (EGRET) is sensitive to the highest energy gamma-rays, those in the 20 MeV to 30 GeV range. To date, *CGRO* has discovered over 120 discrete sources of greater than 100 MeV gamma-ray emission.

Of these discrete sources the second EGRET Source Catalog, compiled from observations during phases I and II of the *CGRO* mission (from 1991 April to 1993 July), lists 40 high confidence identifications of strong, flat-spectrum extragalactic radio sources, and a further 11 marginal identifications [Thompson *et al.* 1995]. Identifications were classified as marginal if the candidate radio counterpart lies close to but outside the 95% uncertainty contour for the gamma-ray source position. Previously, the high confidence and marginal classifications were based solely on photon statistics [von Montigny *et al.* 1995a]. To avoid confusion, the following terminology will be used here: strong and weak describe the statistical significance of detection, and high-confidence and marginal describe the identifications. The rapid optical variability and large optical polarisation of many of the optical counterparts to the radio sources have resulted in their being classified as 'blazars'.

The absolute gamma-ray luminosities for some EGRET sources are exceedingly high ($\sim 10^{48}$ ergs s^{-1}, approximately the Eddington limit for a $10^{10} M_\odot$ black hole)

if isotropic emission is assumed. However, there are reasons for concluding that the emission is not isotropic. A number of the radio counterparts have already been observed with VLBI. These sources have generally exhibited apparent superluminal motions, suggesting beamed emission from relativistic matter travelling close to our line of sight. If the gamma-ray flux is also beamed along our line of sight then the luminosities derived by assuming isotropic emission will be overestimates.

The short time-scale variability of the gamma-ray emission from some of the stronger sources implies that the spatial extent of the gamma-ray emission region is on the order of 10 light days or less [von Montigny et al. 1995a].

From consideration of these two points it is generally postulated that the gamma-ray emission region lies within the base of the relativistic jet (c.f. references in von Montigny et al. 1995a).

The fact that many flat-spectrum radio sources have not been identified by EGRET and the assumption that the gamma-ray emission is beamed has been used to infer that the width of the gamma-ray beam is smaller than that of the radio beam, under a "unified scheme" where all bright, flat-spectrum radio sources are gamma-ray sources. Adopting a beam size for the radio emission of $\sim 14°$ [Padovani & Urry 1992], Salamon & Stecker [1994] derive a beam size for the gamma ray emission of $\sim 4°$. However, Dondi & Ghisellini [1995] argue that the radio and gamma-ray beams may be collimated to the same extent and suggest that the EGRET sources have been detected because they are currently in a high state of gamma-ray emission, thus leaving undetected those sources currently in a low state of gamma-ray emission.

von Montigny et al. [1995b] have offered another alternative, which also relies on relativistic beaming, to explain why some radio sources have been detected in gamma-rays but others have not. von Montigny et al. [1995b] suggest that gamma-ray sources may have jets which remain straight from the scale of the gamma-ray emission region all the way to the kpc-scale and that we lie within the gamma-ray beaming cone as well as the radio beaming cone. On the other hand, jets which bend allow for the possibility that the gamma-ray emission is beamed away from our line of sight but that we still lie within the beaming cone of the radio emission. The implication of this suggestion is that the majority of gamma-ray loud sources have closely aligned small and large-scale jets whereas the majority of gamma-ray quiet sources have misaligned small and large-scale jets.

Indicators of relativistic beaming are therefore very relevant for models of the gamma-ray emission. For example, the models proposed by Salamon & Stecker [1994] and Dondi & Ghisellini [1995] make quite different predictions about the distribution of line of sight angles of the relativistic jet in EGRET sources. Salamon & Stecker predict that all gamma-ray sources have their jets aligned within 4° to the line of sight whereas Dondi & Ghisellini imply a broader distribution of angles to the line of sight.

Such predictions may be tested by comparing the beaming characteristics of radio sources, such as superluminal motions and radio core brightness temperatures, over the full range of gamma-ray activity i.e. nondetections, weak detections, and strong detections, and examining any similarities or differences between these populations.

Thus, the three aims of the work described in this chapter are:

1] To increase the numbers of EGRET-identified radio sources well studied with VLBI by targeting those in the Southern Hemisphere.

2] To begin to build a sample of strong, flat-spectrum radio sources which have not been identified by EGRET but are otherwise similar to the EGRET-identified sources, as a comparison sample.

3] To compare the relativistic beaming indicators derived for the sources presented here from 1] and 2], and also for observations from the literature.

To meet these aims, this chapter describes the first VLBI observations of three EGRET-identified radio sources, PKS 0208−512, 0521−365 and 0537−441, all high-confidence identifications in the second EGRET catalog. Also described are the first high-resolution VLBI observations of four radio sources which have not been identified by EGRET, but show evidence for blazar activity, PKS 0438−438, PKS 0637−752, PKS 1514−241, and PKS 1921−293. In § 4.2, a brief discussion of the beaming indicators which can be estimated from VLBI observations is given. In § 4.3, the data reduction and analysis methods specific to this work are outlined. The results for each individual source are presented in § 4.4, where estimates of the radio core brightness temperatures and pc-scale to kpc-scale misalignment angles are made. A discussion and comparison of the VLBI properties of the sources considered in § 4.4, as well as other radio sources from the literature, is given in § 4.5.

4.2   Indicators of relativistic beaming

Relativistic beaming can be measured in terms of the Doppler factor, δ, which relates the intensity in the observer's frame to the intensity in the rest frame, of radiation originating from material travelling at a significant fraction of the speed of light.

$$\frac{S_{obs}}{S_{rest}} = \delta^{3-\alpha} = \frac{1}{\gamma^{3-\alpha}(1-\beta cos\theta)^{3-\alpha}} = \frac{(1-\beta^2)^{\frac{3-\alpha}{2}}}{(1-\beta cos\theta)^{3-\alpha}} \ ,$$

for a spherical component, where γ and β have their usual definitions in relativity and refer to the motion of the radiating material (e.g. Blandford and Konigl 1979). θ is the angle the material motion makes to the line of sight and α ($S \propto \nu^\alpha$) is the spectral index of the emission.

Another relativistic effect, apparent superluminal motion, can be observed when a source of radiation is moving at a substantial fraction of the speed of light and in a direction close to the observer's line of sight,

$$\beta_{app} = \frac{\beta sin\theta}{1-\beta cos\theta} \ ,$$

where β_{app} is the apparent speed relative to the speed of light. Usually from the observation of the apparent speeds of components in VLBI jets some limits on

the intrinsic speed and angle to the line of sight can be derived. For instance the minimum intrinsic speed of a component with β_{app} can be found by differentiating the above equation and is $\beta_{min} = \sqrt{\frac{\beta_{app}^2}{1+\beta_{app}^2}}$. The maximum angle to the line of sight that the motion of the component can make is found by assuming that $\beta = 1$, the maximum possible, and is $\theta_{max} = cos^{-1}\left(\frac{\beta_{app}^2-1}{\beta_{app}^2+1}\right)$. These limits on β and θ can be used to loosely constrain the Doppler factor.

However, the measurement of radio core brightness temperatures with VLBI observations can provide a direct estimate of the Doppler factor. The observed radio core brightness temperature can be written as [Murphy 1993]

$$T_{12} = \frac{1.22S_{obs}}{ab\nu_{obs}^2} \quad ,$$

where S_{obs} is the observed flux density (in Jy) from a radio core at the frequency ν_{obs} (in GHz) and a and b are the semi-major and semi-minor axes of the core component (in mas). T_{12} is the brightness temperature in the observer's frame, in units of 10^{12} K. If the radio core appears bright due to beamed emission then $S_{obs} = \delta^{3-\alpha}S_{int}$, as above, and $\nu_{obs} = \delta\nu_{int}$. A factor of $(1 + z)$ also needs to be included to account for the effects of cosmological red shift [Lang 1986], thus

$$T_{12} = \frac{1.22S_{int}}{(1+z)ab\nu_{int}^2}\delta^{1-\alpha} \quad .$$

Since the rest frame brightness temperature is limited to the nominal value of 10^{12} K [Kellermann & Pauliny-Toth 1969] it follows that if $T_{12}(1 + z) > 1$ then $T_{12}(1 + z) = \delta^{1-\alpha}$. The Doppler factor can be directly estimated from the three observables T, z, and α.

4.3   Observations and data reductions

VLBI observations, summarised in Table 4.1, were made using the SHEVE (plus Shanghai) array of telescopes. All data were obtained and processed as described in chapter 2.

Brightness temperatures in the observer's frame were estimated from the images, for radio core components de-convolved from the synthesised beam using the JMFIT task in AIPS. JMFIT fits elliptical Gaussians to components and returns only an upper limit on the Gaussian FWHM of unresolved components but returns an estimated FWHM, with upper and lower limits, for components which are resolved. JMFIT also returns the integrated flux density of the component. In the case of unresolved core components, lower limits to the observed brightness temperature were derived using the flux density and the upper limit to the FWHM. For the cores which were resolved, an estimate of the observed brightness temperature could be derived from the estimated FWHM and the flux density. Using the source red shifts, brightness temperatures were then derived in the source frame.

For PKS 0521−365 high-resolution multi epoch and multi frequency data are available, and so, in addition to the above procedures, the following analyses were performed. Limits on the jet to counterjet surface brightness ratios were made directly from the images. Spectral indices, using total flux densities measured from

Source	Epoch	Frequency (GHz)	Participating Telescopes
PKS 0208−512	1992 Nov. 28	4.8	Pk,Hb,Na,Mr,Pr27,Ht
PKS 0438−436	1992 Nov. 26	4.8	Pk,Hb,Na,Mr,Pr27
PKS 0521−365	1992 Nov. 23	4.8	Pk,Hb,Na,Mr,Pr27,Ht,Sh
	1993 Feb. 15	4.8	Pk,Hb,Na,Mr,Pr27
	1993 May 14	4.8	Pk,Hb,Mr,Pr27
	1993 Oct. 21	8.4	Pk,Hb,Na,Mr,Pr15
PKS 0537−441	1992 Nov. 24	4.8	Pk,Hb,Na,Mr,Pr27,Ht,Sh
	1994 Feb. 25	8.4	Ds45,Pk,Hb,Na,Mr
PKS 0637−752	1993 May 15	4.8	Pk,Hb,Na,Mr,Pr27,Ht
PKS 1514−241	1994 Feb. 25	8.4	Ds45,Pk,Hb,Na,Mr
PKS 1921−293	1993 Feb. 15	4.8	Pk,Hb,Na,Mr,Pr27,Ht

Table 4.1: Observation log for EGRET and non-EGRET sources
Ds45 = Tidbinbilla (34 m), Pk = Parkes, Hb = Hobart,
Na = Narrabri, Mr = Mopra, Pr15 = Perth (15 m), Pr27 = Perth (27m),
Ht = Hartebeesthoek, Sh = Shanghai

the images, were estimated. The multi epoch data were used to estimate the apparent speed in the jet of PKS 0521−365. To this end the Caltech task MODELFIT was used to fit simple Gaussian components to the visibility amplitudes and closure phases, either two or three components at each epoch, keeping the core component as the arbitrary phase centre.

4.4   The individual sources

4.4.1   PKS 0208−512

PKS 0208−512 was detected with a strong statistical significance ($> 5\sigma$) by EGRET [von Montigny et al. 1995a]. The high-confidence identification is with a highly polarised quasar at a red shift of 1.003 [Savage 1976; Peterson et al. 1976; Impey & Tapia 1988]. PKS 0208−512 has had the hardest gamma-ray spectrum of all EGRET sources, with a differential spectral index of −1.69±0.05 between 40 MeV and 30 GeV [Bertsch et al. 1993]. The five observations in the first EGRET source catalog show clear evidence of variability in the greater than 100 MeV gamma-ray flux by at least a factor of three on time-scales of tens of days [Bertsch et al. 1993]. Similar variability behaviour was also seen in phase II observations [von Montigny et al. 1995a], and in phase III, when it was the brightest gamma-ray blazar observed by almost a factor of two (R. Hartman et al. 1995, private communication). Recently PKS 0208−512 underwent a major outburst in gamma-rays above the 100 MeV level, further confirming its variable behaviour [Vestrand et al. 1996].

The compact nature of PKS 0208−512 was revealed in the 1982 SHEVE observations at 2.3 GHz, as it was unresolved on the inner Australian baselines [Preston et al. 1989]. The new VLBI observations at 4.8 GHz (Figure 4.1) show that the radio source consists of a bright, unresolved core and a jet-like extension

0208−512 observed at 4.851 GHz, 1992 Nov 28
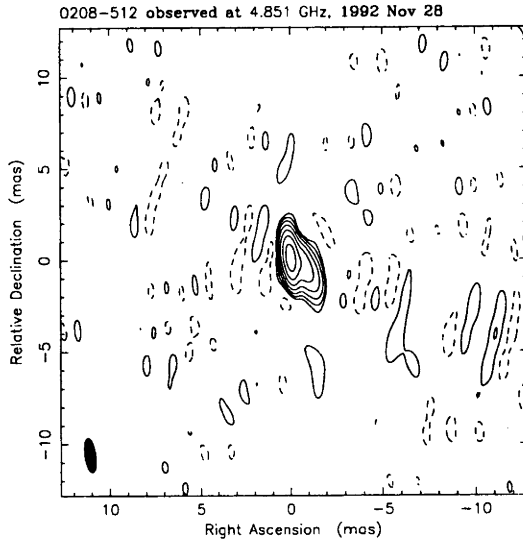
Figure 4.1: Low contour, ±1%. Peak, 2.1 Jy/beam. Beam, 1.9×0.6 mas @ 8.0°. N.B. For each image in this chapter the displayed contours range from the lowest contour indicated in the Figure captions to the highest contour, which is 64% of the peak flux density in the image, each contour increasing by a factor of two. Also, the beam dimensions are of the beam FWHM.

at a position angle of approximately 233°. It is estimated, from these data, that the compact radio core has an observed brightness temperature of $> 1.2 \times 10^{12}$ K, with a de-convolved FWHM of $<0.5 \times < 0.2$ mas and flux density of 2.4 Jy at 4.8 GHz. This corresponds to a source frame brightness temperature of $> 2.4 \times 10^{12}$ K, at or above the inverse Compton limit for synchrotron radiation. The position angle of the jet-like feature in Figure 4.1 aligns closely with a 5″ extension at a position angle of 219° seen with the Australia Telescope Compact Array (ATCA) at 4.8 GHz [Lovell, McCulloch, & Jauncey 1995]. The misalignment between the mas-scale and arcsecond-scale structures is 14°.

Since only one epoch of high resolution VLBI data is available, any motion of the jet-like feature relative to the core cannot be estimated. The 1982 data of Preston et al. [1989] could be modelled by a single Gaussian component. However, the resolution of those observations is well below those reported here.

4.4.2   PKS 0438−436

PKS 0438−436 is one of the bright, flat-spectrum radio sources considered by von Montigny et al. [1995b] to be of interest as a blazar not identified by EGRET. von Montigny et al. [1995b] place an upper limit of 3.4×10^{-7} cm^{-2}s^{-1} for greater than 100 MeV emission from PKS 0438−436. PKS 0438−436 is one of the highest red shift, and consequently highest luminosity, radio loud quasars at z=2.852. It exhibits the typical blazar characteristic of high and variable optical polarisation [Impey & Tapia 1988].

The 1982 VLBI observations at 2.3 GHz of Preston et al. [1989] with the SHEVE array, were the first of PKS 0438−436 and were used to produce both a

0438−436 observed at 4.851 GHz, 1992 Nov 28
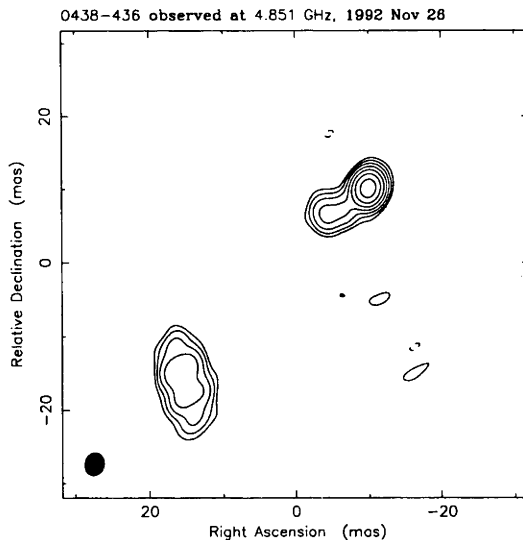
Figure 4.2: Low contour, ±1%. Peak, 1.6 Jy/beam. Beam, 3.2×2.6 mas @ -13.8°

model and an image. It was found that the compact source consisted of two 1.9 Jy components separated by 35 mas at a position angle of -43°, with the south-east component slightly more extended than the north-west component. They also found a large position angle difference between the VLBI structure and a 2″ extension at a position angle of approximately 10° observed with the VLA [Perley 1985]. The angular length and position angle of this arcsecond extension has been confirmed with two-frequency observations at the ATCA [Lovell, McCulloch, & Jauncey 1995].

Images obtained, at a frequency of 2.3 GHz, in 1989 showed no significant change in the structure of the radio source, although both components remained essentially unresolved at this resolution [Murphy et al. 1993].

The new VLBI data, at the higher frequency of 4.8 GHz (Figure 4.2) show the two components seen at lower frequency. The south-east component is less compact than the flat-spectrum north-west component, which is the core of the radio source. The two components are both elongated, but not along the same position angle. The north-west component has a position angle of approximately 124° whereas the south-east component has a position angle of approximately 35°. The position angle connecting the centroids of the two components is approximately 136°, in good agreement with the results of Preston et al. [1989] and Murphy et al. [1993]. The distance between the centroids of the two components is 36.2 mas, only 1.2 mas greater than in 1982. The mismatch in frequency and resolution between the observations do not allow an accurate estimate of any apparent speed of separation between these components.

From Figure 4.2, the core FWHM and integrated flux density have been estimated to be 0.6 × 0.2 mas and 1.6 Jy respectively. The observed radio core brightness temperature is therefore approximately 6.0 × 10^{11} K at 4.8 GHz, corresponding to approximately 2.3 × 10^{12} K in the source frame, at or above the inverse Compton limit for synchrotron radiation.

The misalignment between the VLBI and VLA radio structures noted by Pre-

ston *et al.* [1989] is continued on the mas-scale between the two compact components. The misalignment between the mas-scale and arcsecond-scale structures is approximately 126°. The misalignment on the mas-scale, between the two components, is approximately 89°.

4.4.3   PKS 0521-365

PKS 0521−365 was initially listed as a statistically weak $(4 < \sigma < 5)$ EGRET detection [Fichtel *et al.* 1994; von Montigny *et al.* 1995a; Lin *et al.* 1995]. However, the positional coincidence of the gamma-ray and radio sources resulted in its being classified as a high-confidence identification in the second EGRET catalog [Thompson *et al.* 1995]. PKS 0521−365 is one of the brightest radio sources in the sky at 2.3 GHz [Wall 1994].

The radio source was identified optically as an N galaxy by Bolton, Clarke, & Ekers [1965]. Danziger *et al.* [1979] measured its red shift to be z=0.0554, making it the second lowest red shift AGN in the EGRET list after Mrk 421. PKS 0521−365 has not yet been detected at TeV energies, unlike Mrk 421. The CANGAROO team [Kifune *et al.* 1996] find a 3σ upper limit of 3×10^{-12}cm^{-2}s^{-1} between 1994 December and 1995 January from PKS 0521−365 at energies above 1 TeV. This limit corresponds to approximately 1/5 of the flux at 1 TeV expected from an extrapolation of the EGRET flux at 200 GeV [Bowden *et al.* 1993]. For comparison, the flux of Mrk 421 above 500 GeV is 1.5×10^{-11}cm^{-2}s^{-1} [Punch *et al.* 1992].

Danziger *et al.* [1979] discovered an optical jet and followed up with VLA observations which revealed an asymmetric radio structure with an unresolved component centred on the optical galaxy. More detailed observations of the jets [Keel 1986; Macchetto *et al.* 1991; Falomo 1994] showed a strong correspondence between the features seen at optical and radio wavelengths.

VLBI observations of the unresolved component in the VLA images were first made by Broderick *et al.* [1972] who found a compact component of 0.9 Jy at 2.3 GHz with a 25 million wavelength baseline. Preston *et al.* [1989] modelled their sparse 2.3 GHz data with a 1.2 Jy circular Gaussian component of 1.4 mas FWHM. The new VLBI images (Figures 4.3 - 4.7) show that the compact radio source is dominated by a slightly resolved component, together with a jet-like component which extends towards the north-west at a position angle of 310°. The core is the flat-spectrum component in the south-east. The position angle of the arcsecond-scale optical and radio jets is 312°. The mas-scale and arcsecond-scale structures are aligned to better than 2°.

Figures 4.3, 4.4, and 4.5 show the images resulting from data obtained at 4.8 GHz between 1992 November 23 and 1993 May 14. Figure 4.6 shows an image of slightly higher resolution at 8.4 GHz, from data obtained in 1993 October 21. Finally, Figure 4.7 is another image made from the data at 4.8 GHz from 1992 November 23, after data on baselines to Shanghai and Hartebeesthoek were added to the Australian array data. The resulting high-resolution image resolves out the jet-like feature seen in Figure 4.3 but reveals the structure of the radio source within 5 mas of the core.

0521−365 observed at 4.851 GHz, 1992 Nov 23

Figure 4.3: Low contour, ±1%. Peak, 1.3 Jy/beam. Beam, 4.7×2.3 mas @ 1.5°.

0521−365 observed at 4.851 GHz, 1993 Feb 15

10 pc
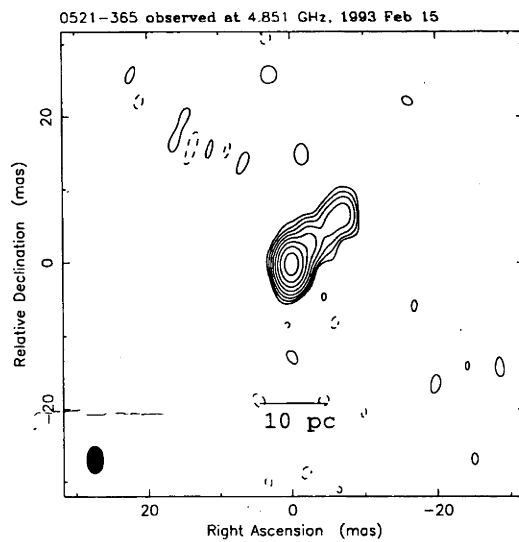
Figure 4.4: Low contour, ±0.5%. Peak, 1.8 Jy/beam. Beam, 3.7×2.3 mas @ 0.6°.
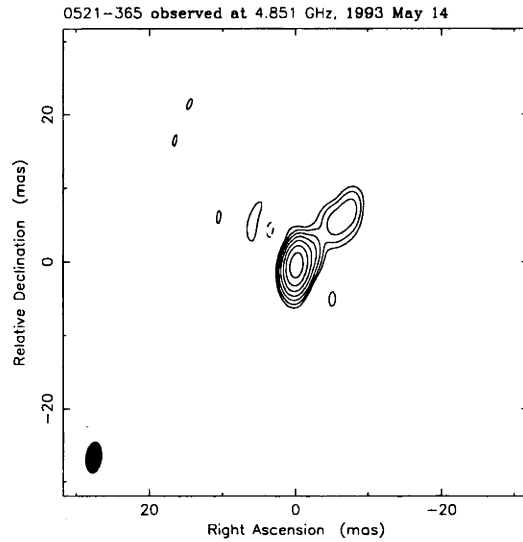
Figure 4.5: Low contour, $\pm 1\%$. Peak, 2.0 Jy/beam. Beam, 4.3×2.1 mas @ -6.3°.
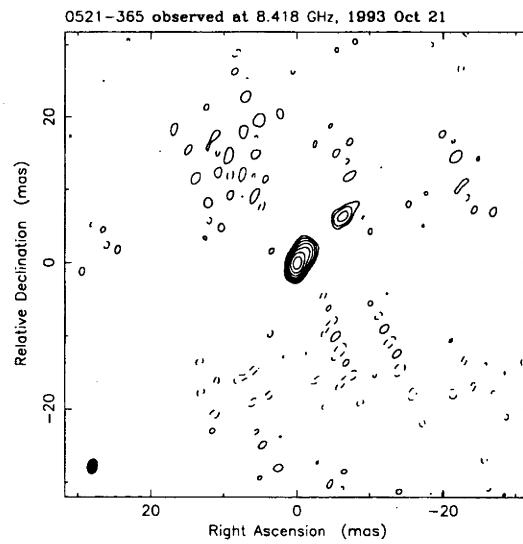
Figure 4.6: Low contour, $\pm 1\%$. Peak, 1.6 Jy/beam. Beam 2.0×1.3 mas @ -10.1°.
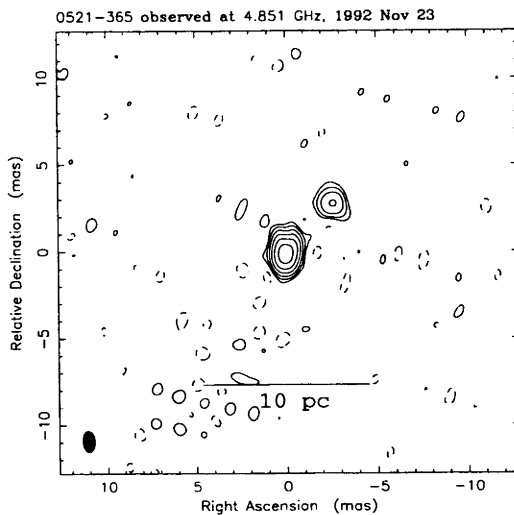
Figure 4.7: Low contour, ±2%. Peak, 0.7 Jy/beam. Beam, 1.2×0.7 mas @ 3.7°.

Epoch	Freq (GHz)	R	d (mas)
1992 Nov. 23	4.8	>9.3	$7.8\pm^{1.4}_{1.6}$
1993 Feb. 15	4.8	>8.6	$8.6\pm^{1.4}_{1.6}$
1993 May 14	4.8	>5.0	$9.4\pm^{1.4}_{2.0}$
1993 Oct. 21	8.4	>2.9	$10.3\pm^{1.2}_{1.8}$

Table 4.2: Limits on jet to counterjet surface brightness ratio (R) and core-jet separation (d) for each of the PKS 0521−365 epochs.

The observed (and source frame) brightness temperature of the core, from Figure 4.7, is 1.0×10^{11} K; de-convolved component FWHM of 0.8×0.6 mas and total flux density of 1.2 Jy at 4.8 GHz.

Limits on the jet to counterjet surface brightness ratio (R) and core-jet separations (d) are given at each epoch in Table 4.2. Given the error-bars on the core-jet separations and the lower limits on R, these results are consistent with the idea of mild relativistic speeds and moderate beaming proposed by Falomo *et al.* [1995] for PKS 0521−365, but also with a model which has a highly relativistic flow closely aligned to our line of sight. However, the brightness temperature is well below the nominal inverse Compton limit of 10^{12} K and therefore does not favour PKS 0521−365 as a highly beamed radio source. Observations at later epochs will allow further constraints on any apparent motion in the jet of PKS 0521−365, giving a more complete indication of the importance of relativistic beaming.

4.4.4   PKS 0537−441

The blazar PKS 0537−441 (z=0.894) was detected with a strong statistical significance by EGRET [von Montigny *et al.* 1995a] and subsequently became a high-confidence identification. Its optical polarisation of 10% [Impey & Tapia 1990] and

optical variability with a total range of more than 4 mag. (see references in Tanzi *et al.* 1986) is reminiscent of BL Lac objects, but its broad optical emission lines are features of quasars. It is sometimes classified as a highly polarised quasar [Treves *et al.* 1993; Sambruna *et al.* 1994].
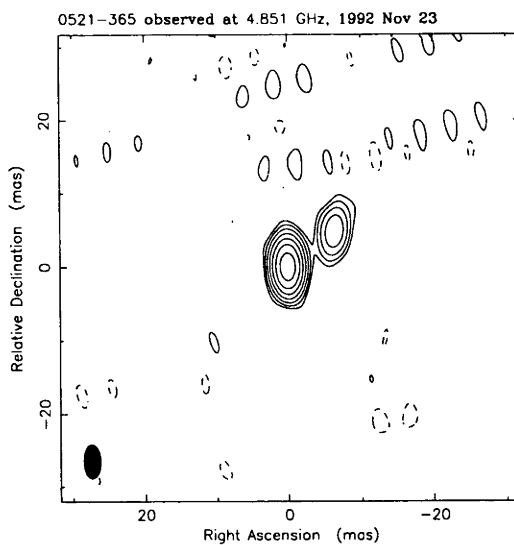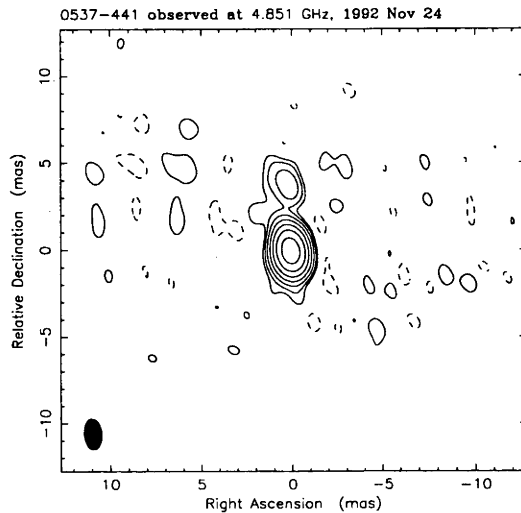

Figure 4.8: Low contour, $\pm 1\%$. Peak, 3.0 Jy/beam. Beam, 1.8×0.9 mas @ $4.5°$.
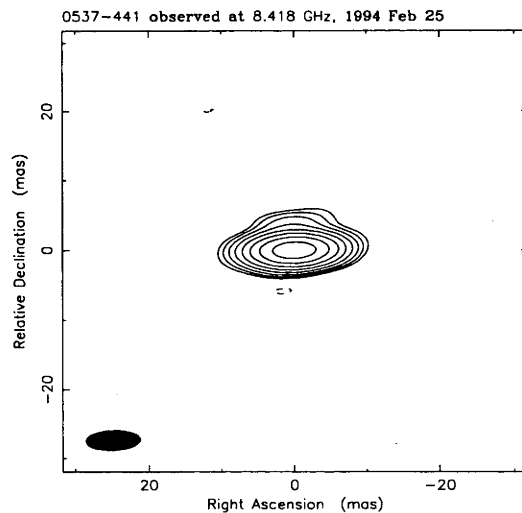
Figure 4.9: Low contour, $\pm 0.5\%$. Peak, 6.2 Jy/beam. Beam, 7.4×2.9 mas @ $-87.8°$.

The compact nature of PKS 0537−441 was clear from the 1982 SHEVE observations at 2.3 GHz in which the object was unresolved on all Australian baselines [Preston *et al.* 1989]. Using a 4 hr scan on the intercontinental baseline from Australia to South Africa, along with the shorter internal Australian baselines, [Preston *et al.* 1989] modelled the source as a circular Gaussian component of 1.1

mas FWHM and total flux 4.2 Jy with no evidence of a jet. The new VLBI images at 4.8 and 8.4 GHz (Figures 4.8 and 4.9) show that the source is dominated by a slightly resolved component which can be identified as the core, together with a jet-like component extending towards the north at a position angle of 3°. The jet-like component may have appeared during the 10 years between epochs, but it is just as likely that the lack of $u - v$ constraints in 1982 allowed the available data to be modelled with a single component.

Perley [1982] found a 7.″2 extension to the compact radio core at a position angle of 305° with the VLA. Thus, the misalignment between the mas-scale and arcsecond-scale structures is approximately 58°.

From Figure 4.8, the FWHM of the slightly resolved core component is estimated to be, de-convolved from the beam, 0.9 × 0.3 mas with a flux density of 4.0 Jy, from which an observed brightness temperature is approximately 7.0×10^{11} K at 4.8 GHz can be inferred. The source frame brightness temperature is therefore approximately 1.3×10^{12} K, near the inverse Compton limit for synchrotron radiation.

4.4.5   PKS 0637−752

PKS 0637−752 (z=0.656) is another of the strong, flat-spectrum radio sources considered by von Montigny *et al.* [1995b] in their investigation of radio sources not identified by EGRET. von Montigny *et al.* [1995b] place an upper limit of 1.5 × 10^{-7} cm^{-2}s^{-1} in greater than 100 MeV gamma-rays from the direction of this AGN.
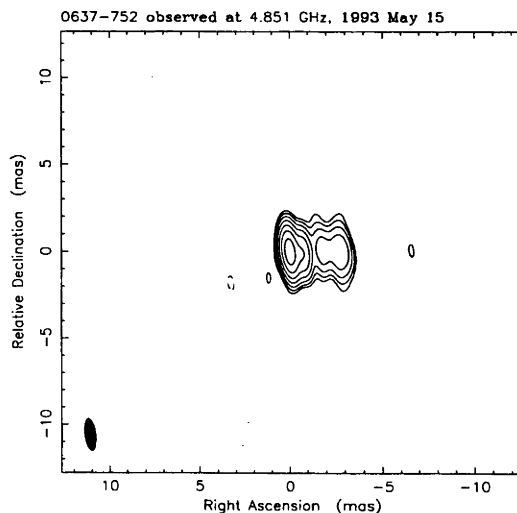
Figure 4.10: Low contour, ±1%. Peak, 3.6 Jy/beam. Beam, 1.9×0.6 mas @ 7.3°.

The compact structure of the radio source was first revealed by Preston *et al.* [1989] with 2.3 GHz VLBI observations utilising the SHEVE array. They reported an essentially unresolved component with a 2.6 Jy core and a halo of emission greater than 20 mas in extent with a flux density of 1.5 Jy. The latest VLBI observations (Figure 4.10) at the higher frequency of 4.8 GHz show that the

compact radio structure is dominated by a bright core and a jet lying at a position angle of approximately $-90°$. Two-frequency imaging of the kpc-scale radio structure with the ATCA [Lovell, McCulloch, & Jauncey 1995] shows a strongly one-sided jet which lies at a position angle of approximately $-86°$. The mas-scale and arcsecond-scale radio structures are very well aligned, the difference in position angle being approximately $4°$.

From Figure 4.10, the core FWHM and total flux density, de-convolved from the restoring beam, have been estimated at 0.4×0.4 mas and 4.3 Jy respectively, leading to a value for the observed radio core brightness temperature of approximately 1.5×10^{12} K at the frequency of 4.8 GHz. The source frame brightness temperature is therefore approximately 2.6×10^{12} K, again at or in excess of the inverse Compton limit for synchrotron radiation.

Again the mismatch in resolution and data quality between this image and the model of Preston *et al.* [1989] do not allow a useful estimate of apparent motion to be made for this source.

4.4.6   PKS 1514−241

PKS 1514−241 (AP Libræ) is a low red shift (z=0.049) BL Lac type object with a compact, flat-spectrum radio core and is a well studied blazar. It has not been identified by EGRET and is therefore of interest in a comparison between gamma-ray loud and gamma-ray quiet AGN; EGRET detected not only the powerful AGN at large red shifts, but also AGN which are considerably less luminous at low red shifts (e.g. PKS 0521−365 and Mrk 421). Fitchel *et al.* [1994] placed an upper limit to greater than 100 MeV photons of 0.7×10^{-7} cm^{-2} s^{-1} for PKS 1514−241. The typical blazar characteristics of high optical polarisation and variability have been well demonstrated for this source. The optical polarisation measured by Kinman [1976] varied over the range 2 - 6% and rapid variability has been observed at optical wavelengths [Webb *et al.* 1988].
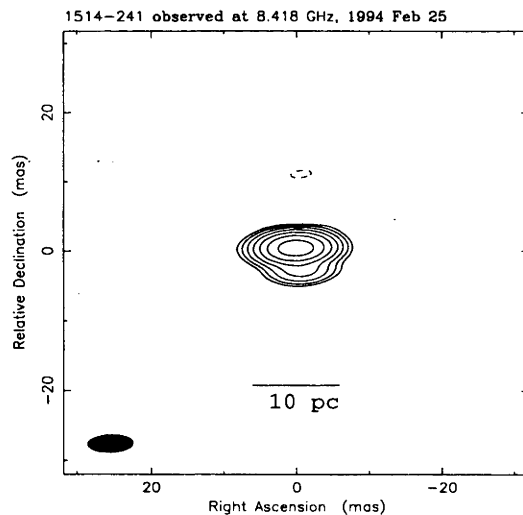
Figure 4.11: Low contour ±1%. Peak 1.9 Jy/beam. Beam, 6.1×2.5 mas @ -87.9°

PKS 1514−241 has previously only been observed with single baseline VLBI [Preston *et al.* 1985; Mollenbrock *et al.* 1996] and shows compact structure on intercontinental baselines. The observations described here were made at a frequency of 8.4 GHz and are the first VLBI imaging observations. The image (Figure 4.11) shows a strong core component of 1.9 Jy and a short jet-like extension at a position angle of approximately 195°.

Several investigators have published images of the extended radio emission of PKS 1514−241. Stannard and McIlwrath [1982] present a MERLIN image at 0.4 GHz with 2.″5 resolution which shows a 5″ extension at a position angle of approximately 125°. However, Antonucci and Ulvestad [1985] present a 20 cm VLA A configuration image of PKS 1514−241 with a resolution of 1.″2 arcseconds which shows a 23″ extension from the core at a position angle of approximately 100°. Likewise, Morganti *et al.* [1993] present a C+B$_N$ configuration VLA image at a frequency of 4.885 GHz of PKS 1514−241. The image has a resolution of 4.″4 × 4.″8 and shows a 21″ extension at a position angle of approximately 90°. The higher quality and more recent observations from the VLA are consistent between Antonucci and Ulvestad [1985] and Morganti *et al.* [1993]. The mas-scale and arcsecond-scale structures are therefore misaligned by approximately 100°.

From the VLBI image the de-convolved core dimensions of 1.3 × 0.9 mas and the total core flux density of 2.2 Jy give an observed radio core brightness temperature of 3.0 × 10^{10} K at 8.4 GHz. This value is very low and is due to the fact that only short baselines (< 1000 km) were obtained with these observations. This value for the brightness temperature will not be useful for comparison with the data for the other six sources since those data were obtained at 4.8 GHz, with baselines exceeding 3000 km. Mollenbrock *et al.* [1996] observed PKS 1514-241 as part of the VSOP pre-launch survey on an intercontinental baseline at 22 GHz and found an observed brightness temperature at that frequency of > 1.46±0.21 × 10^{11} K.

4.4.7   PKS 1921−293

PKS 1921−293 is one of the strongest (up to ∼20 Jy), flat-spectrum radio sources in the sky, but was not identified by EGRET in greater than 100 MeV gamma-rays. It is a highly polarised and optically violently variable quasar (OV-236) at a red shift of z=0.352 [Pica *et al.* 1988]. Fichtel *et al.* [1994] place an upper limit to greater than 100 MeV emission from PKS 1921−293 of 0.6 × 10^{-7} cm^{-2}s^{-1}. It was not considered by von Montigny *et al.* [1995b] in their investigation of radio sources not identified by EGRET whereas they did consider the similar sources PKS 0438−436 and 0637−752. As one of the most extreme blazars, and one of the brightest core dominated radio sources PKS 1921−293 clearly should be considered in any comparison between gamma-ray loud and quiet AGN.

PKS 1921−293 was observed by Preston *et al.* [1989] with the first multi-baseline VLBI observations at a frequency of 2.3 GHz. They found the radio source to consist of a 5 mas elongated component at a position angle of approximately 25° and with a flux density of 6.6 Jy. The new VLBI observations at 4.8 GHz are represented by the image in Figure 4.12. The image shows that the compact radio source is dominated by an unresolved core component and a jet-like structure at a position angle of approximately 25°, in agreement with the results of Preston *et al.* [1989]. PKS 1921−293 was completely unresolved at the VLA at 1.4 and 5 GHz

as observed by de Pater, Schloerb and Johnston [1985] and Perley [1982]. Thus, no comparison between the mas-scale and arcsecond-scale structure position angles can be made.
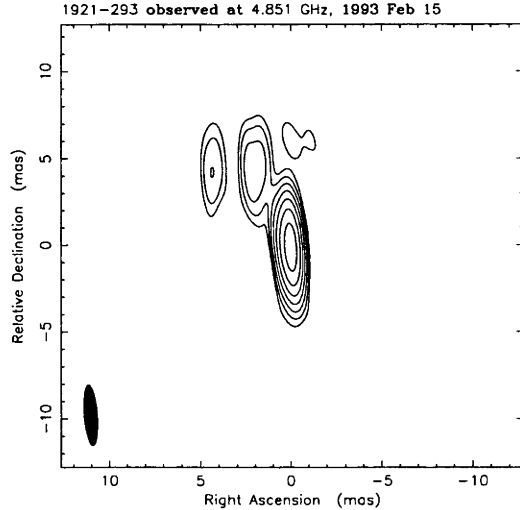
Figure 4.12: Low contour, 1%. Peak, 7.9 Jy/beam. Beam, 3.5×0.7 mas @ 4.2°.

From Figure 4.12, the core dimensions and flux density, de-convolved from the restoring beam, are < 0.5 × <0.5 mas and 9.4 Jy. These values give an observed radio core brightness temperature of > 2.1×10^{12} K at the frequency of 4.8 GHz, corresponding to a source frame brightness temperature of > 2.8×10^{12} K. Thus PKS 1921−293 possibly has the highest brightness temperature of the seven radio sources considered here, in excess of the inverse Compton limit for synchrotron radiation. This result is consistent with the findings of Mollenbrock et al. [1996] who measured 140 extragalactic radio sources with trans-continental baselines at a frequency of 22 GHz. They found that PKS 1921−293 had the highest correlated flux density and observed brightness temperature in their sample, 12.6±1.6 Jy and >$7{\pm}^{4}_{2} \times 10^{12}$ K respectively.

The high brightness temperature inferred from ground-based VLBI observations [this work; Mollenbrock et al., 1996] is confirmed from VLBI observations with greater than Earth diameter baselines. From the Tracking and Data Relay Satellite System (TDRSS) space VLBI experiments Linfield et al. [1989] found that PKS 1921−293 had a source frame brightness temperature of approximately 3.8×10^{12} K at a frequency of 2.3 GHz.

4.5   Discussion

The images presented in the last section show that these seven compact radio sources are dominated by > 1 Jy cores and resolved into core-jet morphologies. In the cases of PKS 0208−512, 0521−365, and 0637−752, the position angle of the mas-scale structure seen with VLBI aligns with the position angle of the arcsecond-scale radio structure, with agreement better than 15°. In the cases

of PKS 0438−436, 0537−441, and 1514−241, the mas-scale and arcsecond-scale position angles are significantly misaligned, with agreement worse than 55°. For PKS 1921−293, no arcsecond-scale radio emission has been detected, so no comparison between the mas-scale and arcsecond-scale position angles is possible.

The misalignment angles do not correlate with the statistical significance of EGRET detectability. PKS 0208−512 and 0537−441 are strong statistical EGRET detections ($> 5\sigma$ significance), PKS 0521−365 is a weak statistical EGRET detection ($4 < \sigma < 5$ significance) and PKS 0438−436, 0637−752, 1514−241, and 1921−293 are EGRET non-detections (Table 4.3). It is important to repeat that the significance of the EGRET detection, based on the photon statistics, is being considered here, given that the identifications of the gamma-ray sources with the radio sources can be made, as Thompson *et al.* [1995] assert, with high confidence.

The estimates of radio core brightness temperatures for the seven sources suggest that PKS 0208−512, 0438−438, 0637−752, and 1921−293 are more highly beamed than PKS 0521−365, and 0537−441, probably requiring Doppler factors of ~ 2 to explain the $> 10^{12}$ K source frame brightness temperatures. For PKS 1514−241, a good estimate of the radio core brightness temperature is not available. However, as for the misalignment angles, the brightness temperatures for the six sources do not correlate with EGRET detectability (Table 4.3).

source	z	EGRET	$T_{12,obs}$	$T_{12,s.f.}$	$\theta^\circ_{|mas-as|}$
PKS 0208−512	1.003	strong detection	>1.2	>2.4	14
PKS 0438−436	2.852	no detection	0.6	2.3	126
PKS 0521−365	0.055	weak detection	0.1	0.1	2
PKS 0537−441	0.894	strong detection	0.7	1.3	58
PKS 0637−752	0.656	no detection	1.5	2.6	4
PKS 1514−241	0.049	no detection	N/A	N/A	100
PKS 1921−293	0.352	no detection	>2.1	>2.8	N/A

Table 4.3: VLBI and EGRET properties of the 7 sources

On the basis of the brightness temperatures and misalignment angles for these seven sources, no strong statement concerning the importance of relativistic beaming for identification by EGRET can be made. Is it possible, however, to increase the number of objects under consideration by examining existing VLBI data in the literature and find trends which could link the gamma-ray and VLBI characteristics of the EGRET-identified sources, or differentiate the EGRET-identified radio sources from radio sources which have not been identified by EGRET?

In investigating these questions the VLBI properties under consideration will be:

1] The apparent speed of components in mas-scale jets.

2] The misalignment of mas-scale and arcsecond-scale jets.

3] Radio core brightness temperatures.

4.5.1   Apparent speeds

First, 9 of the 11 EGRET-identified sources listed by Thompson *et al.* [1995], which have been well studied with VLBI, are known or possible superluminal radio sources [Vermeulen & Cohen 1994; Barthel *et al.* 1995; this work]. The mean apparent speed in the VLBI jets of these 11 EGRET-identified sources is $5.6h^{-1}c$ with a standard deviation of $7.3h^{-1}c$.[1] While there is substantial evidence that some EGRET-identified sources are highly beamed, some others do not appear to be. Some of the strong EGRET sources, for example 1226+023 (e.g. Unwin *et al.* 1985) are clearly highly superluminal whereas others such as 1222+216 [Hooimeyer *et al.* 1992] are perhaps consistent with subluminal speeds.

Second, there are some highly superluminal radio sources that have not been identified by EGRET, such as 1641+399 [Biretta, Moore & Cohen 1986]. The mean apparent speed for the core selected quasars and BL Lac objects which are listed by Vermeulen and Cohen [1994] and have not been identified by EGRET is $3.9h^{-1}c$, with a standard deviation of $3.0h^{-1}c$ (based on 24 objects and using the same method as for the EGRET-identified sources).

These data do not allow a firm conclusion to be made regarding possible differences or similarities in beaming characteristics between the radio sources EGRET has identified and those not identified. The mean values for the apparent VLBI speeds are easily consistent at the 1σ level, but the standard deviations on the distributions are large.

For the sake of completeness, an apparent speed of $\beta_{app} = 5.6$ (for the EGRET-identified sources) corresponds to a minimum intrinsic speed of $\beta_{min} = 0.984$ for the radiating material and a maximum angle to the line of sight of $\theta_{max} = 14°$ for the motion. Likewise for the sources not identified by EGRET $\beta_{app} = 3.9$ gives $\beta_{min} = 0.969$ and $\theta_{max} = 28°$. Using these limits in the equation for the Doppler factor gives rough values of δ for the EGRET-identified sources of 4.0, and 1.7 for the radio sources not identified by EGRET.

4.5.2   Misalignment angles

In order to investigate the suggestion of von Montigny *et al.* [1995b] that the jets in EGRET-identified radio sources may be preferentially straight, information on the mas-scale and arcsecond-scale radio emission from EGRET-identified sources has been compiled from the literature. 18 of the 40 high-confidence EGRET identifications listed by Thompson *et al.* [1995] were found to have the relevant information of sufficient quality to find the difference between the mas-scale and arcsecond-scale radio structure position angles. For the remaining 22 sources either no information was found, or else the information was not of a sufficient quality to allow the determination of the position angle difference. The data compiled for the 18 sources are plotted as a histogram in Figure 4.13. From the histogram it can be seen that a strong peak in the distribution of position angle differences occurs near 0°, or no misalignment.

---

[1]This estimate includes the highest reliability VLBI observations listed by Vermeulen & Cohen [1994] for 9 sources, the observations of Barthel *et al.* [1995] for 1633+382 and the data for PKS 0521−365 appearing in Table 4.2. Where multiple observations of similar reliability were available for a single source from Vermeulen & Cohen [1994] they were used to form an average

MISALIGNMENT ANGLE (DEGREES)
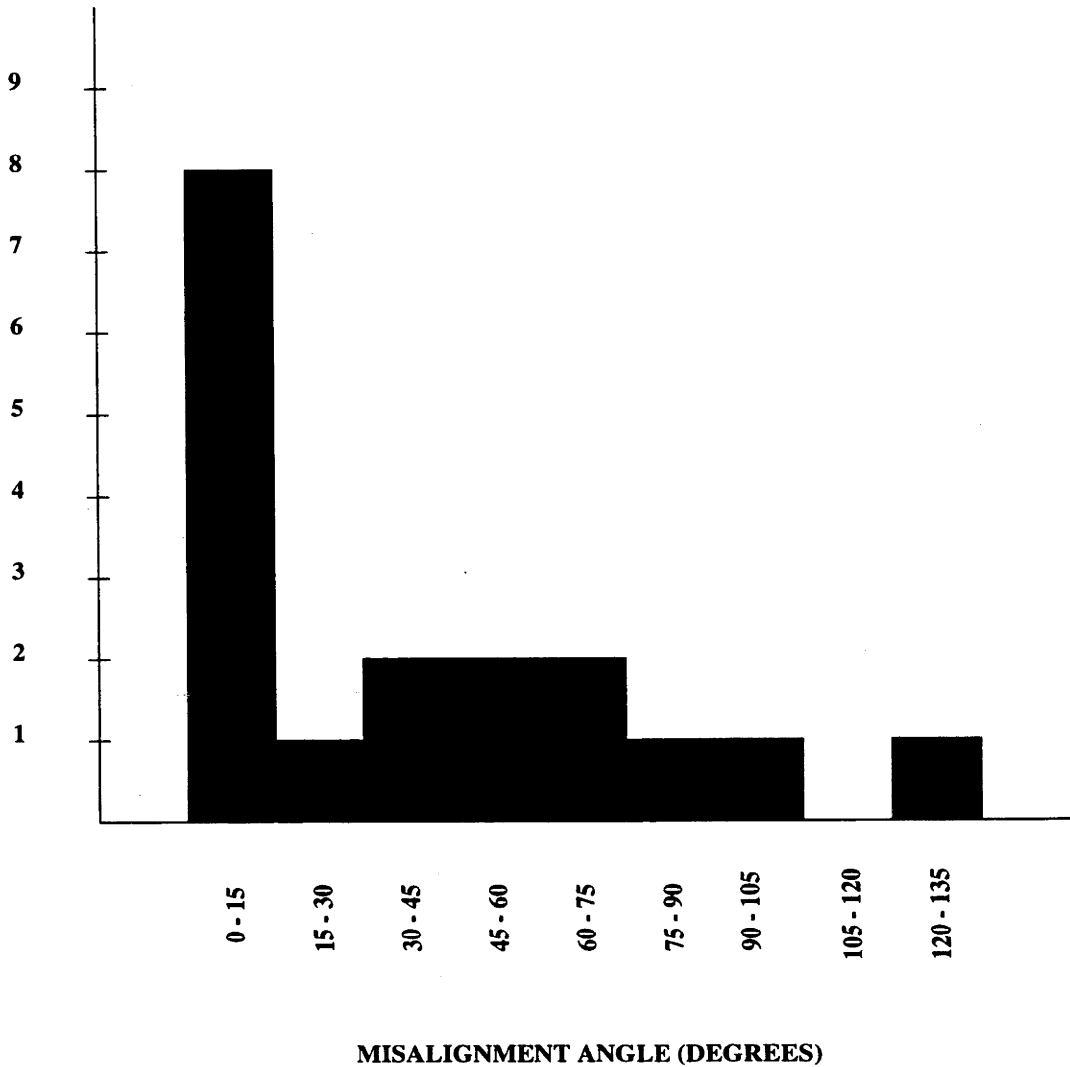
Figure 4.13: Misalignment angles for 18 EGRET-identified radio sources

To investigate the possibility that the core dominated radio sources not identified by EGRET preferentially have bent jets, information on the mas-scale and arcsecond-scale radio structure of 11 core dominated quasars and BL Lac objects from the list given by Vermeulen and Cohen [1994] and 4 core dominated quasars appearing in both Murphy, Browne, and Perley [1993] and Polatidis et al. [1995] was collected. In addition, 3 of the sources considered for the first time here, PKS 0438−438, 0637−752, and 1514−241 were utilised to complete a list of 18 objects. Figure 4.14 is the histogram of the position angle differences for these 18 sources.

A simple Kolmogorov-Smirnov two-sample test was used to determine if the differences between the distributions of position angle differences are significant. For 18 objects and a maximum difference of 4/18 in the cumulative distribution it is not possible to reject the null hypothesis that the two samples are drawn from the same parent distribution. On the basis of these 36 objects there is no reason to conclude that EGRET-identified radio sources have a greater preference for straight jets than radio sources not identified by EGRET.

---

value for the source.

MISALIGNMENT ANGLE (DEGREES)
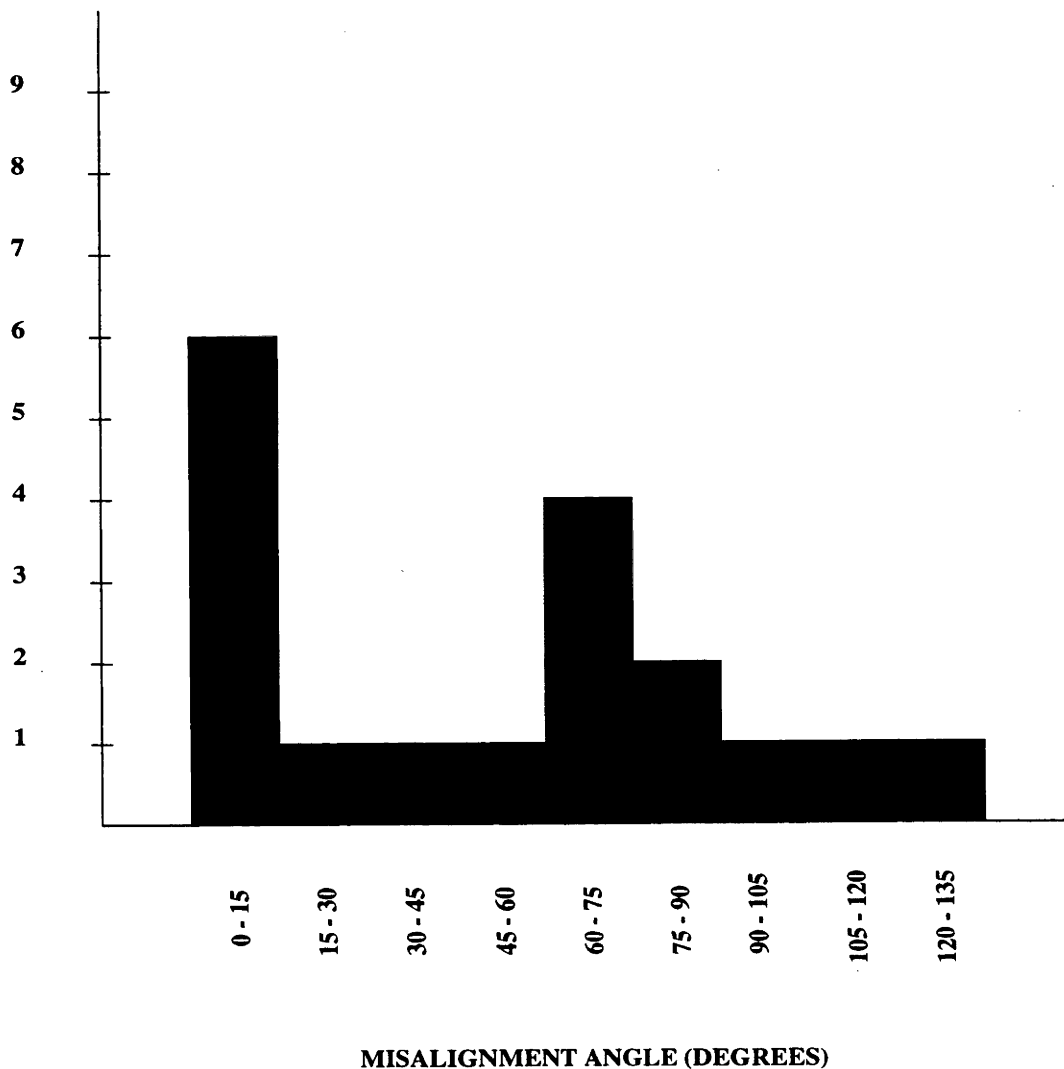
Figure 4.14: Misalignment angles for 18 radio sources not identified by EGRET

4.5.3   Brightness temperatures

Mollenbrock *et al.* [1996] list the observed brightness temperatures, or lower limits, for 140 compact radio sources derived from 22 GHz intercontinental VLBI obser- vations. They plot the brightness temperature distribution for their sample and highlight the EGRET-identified sources. It appears that these 21, 17 high confi- dence and 4 marginal, EGRET-identified radio sources prefer the high brightness temperature end of this distribution, although the brightest and highest brightness temperature source in their sample is PKS 1921−293.

Mollenbrock *et al.* [1996] evaluate the statistical significance of this result with a Kolmogorov-Smirnov test and find that the observed brightness temperature distribution of the EGRET-identified sources is different to that for the 119 sources in their sample not identified by EGRET at a confidence level better than 95%. This result will need to be confirmed since to measure high brightness temperatures accurately longer baselines must be used. If the cores in radio-loud AGN are, in reality, unresolved then the measured brightness temperature is independent of the frequency of observation and only sensitive to the length of the baseline. Thus, high frequency observations on Earth-based baselines are not effective for measuring high

brightness temperatures, hence the need arises for the Earth-space baselines which will be provided by the upcoming VSOP and RadioAstron space VLBI missions.

Space VLBI observations have previously been made with the TDRSS satellite in conjunction with ground-based telescopes [Levy *et al.* 1986]. Linfield *et al.* [1989; 1990] report on the measurement of source frame radio core brightness temperatures from these observations.

At 2.3 GHz, Linfield *et al.* [1989] detected 23 out of 24 sources observed and could derive Gaussian models and therefore brightness temperatures for 14. Two of these sources have been identified as gamma-ray sources and the remaining 12 have not. The brightness temperatures of the two gamma-ray sources, 0420−014 and 1253−055, are midrange in the sample, 3.14×10^{12} K and 1.59×10^{12} K respectively. The brightness temperatures for the remaining 12 sources ranged between 2.5×10^{11} K (0723−008) and 3.80×10^{12} K (PKS 1921−293). 0420−014 and 1253−055 were the third and seventh highest brightness temperature objects respectively.

At 15 GHz, Linfield *et al.* [1990] were able to derive Gaussian models and brightness temperatures for 9 of the same 24 sources. Four of these are identified gamma-ray sources. Again, the brightness temperatures for these sources, 1223−023, 1253−055, 1510−089, and 1730−130 are midrange for the sample, 1.14×10^{12} K, 1.98×10^{12} K, 1.55×10^{12} K, and 8.7×10^{11} K respectively. The remaining 5 sources are gamma-ray quiet and have 15 GHz brightness temperatures ranging between 5.0×10^{11} K (0823+033) and 2.40×10^{12} K (3C 446). The ranking of the gamma-ray sources in brightness temperature was sixth, fourth, fifth, and seventh respectively.

The results of section 4.3, Mollenbrock *et al.* [1996] and Linfield *et al.* [1989; 1990] are in a sense consistent. All of these investigations have shown that the EGRET-identified radio sources can have core brightness temperatures in excess of 10^{12} K, the nominal inverse Compton limit for synchrotron radiation and therefore, Doppler factors greater than unity. However, the highest brightness temperature objects are not all EGRET-identified sources. In particular these studies have one object in common, PKS 1921−293, which is not an EGRET-identified source but consistently revealed to be the highest brightness temperature object.

Despite this level of consistency, the large-sample study of Mollenbrock *et al.* [1996] has shown evidence that the EGRET sources, in general, have significantly higher radio core brightness temperatures than those sources not identified by EGRET, at least as measured with ground-based VLBI observations.

4.6 Conclusions

It is clear that some EGRET-identified radio sources are highly superluminal and/or have high radio core brightness temperatures, in excess of the nominal inverse Compton limit for synchrotron radiation. This is evidence that relativistic beaming is an important effect to consider for at least some gamma-ray loud sources.

It is also clear that some strong, flat-spectrum radio sources which have not been identified by EGRET are also highly superluminal and/or have high radio core brightness temperatures. In particular, these characteristics can be displayed

at least as extremely as for the EGRET-identified radio sources.

A wide variety of behaviours can be noted when the two populations are examined. There exist examples of objects which have strongly beamed core radio emission, but have not been identified by EGRET *and* have highly linear projected jets at least from pc-scales to kpc-scales (e.g. PKS 0637−752; § 4.3.5). There also exist examples of radio sources which do not have highly beamed radio emission, but have been identified as gamma-ray sources *and* have linear jets (e.g. PKS 0521−365; § 4.3.3). Some EGRET-identified radio sources have bent jets, others have straight jets. Likewise for the radio sources not identified by EGRET.

It would follow that **a simple, one-to-one link between beamed radio emission and gamma-ray emission is not tenable**. Any plausible model for gamma-ray emission from AGN must somehow allow for a large variation in the radio to gamma-ray spectral index from object to object, or within a given object over time.

Salamon & Stecker [1994] need to appeal to an argument of this sort to explain the highly beamed but gamma-ray quiet radio sources. The existence of gamma-ray sources in jets which appear to point away from our line of sight (e.g. PKS 0521−365) is a larger problem for their proposed model since they predict that all gamma-ray sources should have their jets only a few degrees from our line of sight.

The suggestion of Dondi & Ghisellini [1995] that the radio and gamma-ray beaming cones may be collimated to the same extent is supported by the existence of objects like PKS 0521−365 and explains how gamma-rays can be observed from jets at moderate angles to the line of sight. In their model, Dondi & Ghisellini [1995] do appeal to variability in the radio to gamma-ray spectral index to explain the beamed radio sources which have not been identified as gamma-ray sources. This model may, therefore, be feasible.

The suggestion of von Montigny *et al.* [1995b] that jet bending may be a simple explanation for the difference between gamma-ray loud and quiet objects is not supported by the data presented here. However, this explanation cannot be ruled out for some sources such as PKS 0438−438 (§ 4.3.2) which appear to have extreme jet bending. We could quite easily miss the gamma-ray beaming cone in this object but easily pick up the radio beaming cone as the jet bends dramatically.

Thus, in answer to the questions posed above, it is not clear which, if any, VLBI characteristics distinguish the EGRET-identified radio sources from those not identified by EGRET. The conclusion of Mollenbrock *et al.* [1996] that EGRET sources have higher observed brightness temperatures than sources not identified by EGRET is the only substantial evidence in support of a difference in the beaming characteristics between these two populations, based on VLBI properties.

However, investigations of the relationships between the gamma-ray and VLBI properties of AGN are compromised by a number of limitations. One limitation is the sensitivity of the EGRET instrument. Even though the number of known extragalactic gamma-ray sources has increased dramatically by virtue of the EGRET observations, only the brightest gamma-ray sources are being identified. In addition, although 40 extragalactic sources have been positively identified a comparable number of discrete EGRET detections (39) which lie away from the Galactic plane have not yet been identified.

From the VLBI point of view, the data on the EGRET identified sources is rel-

atively scarce, apart for a few of the very well studied sources. In particular, many of the determinations of apparent speed carry large error bars as a consequence of the sparse data which are available. Many of the EGRET-identified radio sources only have rudimentary VLBI and VLA images available, which make the task of estimating misalignment angles difficult. In addition, an unavoidable difficulty with ground-based VLBI is that the technique is not suited to the accurate measurement of high brightness temperature objects, with the consequence that arguments based on identifying high brightness temperatures with relativistic beaming cannot be accurately quantified. Observations combining Earth-orbiting radio telescopes with ground arrays will alleviate this inaccuracy since with longer baselines space VLBI will be able to accurately measure high brightness temperatures [Hirosawa 1991]. The author is the principle investigator on a proposal which has been made part of the 'blazar' Key Science Program of the VSOP Space VLBI mission: a Space VLBI investigation of a sample of gamma-ray loud and quiet blazars. Included in this sample are PKS 0208−512, 0438−436, 0537−441, and 0638−752.

As our knowledge of the extragalactic gamma-ray population improves and the VLBI observations of the counterpart radio sources become more comprehensive and of better quality it may be that links between the gamma-ray and VLBI properties of AGN can be revealed. The possibility remains, however, that even though VLBI is the technique that allows the most direct indication of the importance of relativistic beaming, as close as is possible to the supposed gamma-ray emitting region, it is still probing a spatial region orders of magnitude larger than the suspected origin of the gamma-ray emission. Thus the properties of the jet on scales observable by VLBI may bear no relation to the properties of the jet in the gamma-ray emitting region.

Chapter 5

Sub-parsec-scale structure and evolution in Centaurus A

Discovery of a sub-parsec-scale counterjet in the nucleus of Centaurus A
Jones, D.L., Tingay, S.J., Murphy, D.W., Meier, D.L., Jauncey, D.L., Reynolds, J.E., Tzioumis, A.K., Preston, R.A., McCulloch, P.M., Costa, M.E., Kemball, A.J., Nicolson, G.D., King, E.A., Lovell, J.E.J., Clay, R.W., Ferris, R.H., Gough, R.G., Sinclair, M.W., Ellingsen, S.P., Edwards, P.G., & Jones, P.A.
Submitted to The Astrophysical Journal Letters (April 1996)

Sub-pc-scale Structure and Evolution of Centaurus A (NGC 5128)
Jauncey, D.L., Tingay, S.J., Preston, R.A., Reynolds, J.E., Lovell, J.E.J., McCulloch, P.M., Tzioumis, A.K., Costa, M.E., Murphy, D.W., Meier, D.L., Jones, D.L., Amy, S.W., Biggs, J.D., Blair, D.G., Clay, R.W., Edwards, P.G., Ellingsen, S.P., Ferris, R.H., Gough, R.G., Harbison, P., Jones, P.A., King, E.A., Kemball, A.J., Migenes, V., Nicolson, G.D., Sinclair, M.W., van Ommen, T., Wark, R.M., & White, G.L.
Proc.Nat.Acad.Sci.USA 92, 11368-11370 (1995 December).

Centaurus A, The Core of the Problem
Tingay, S.J., Jauncey, D.L., Preston, R.A., Reynolds, J.E., Meier, D.L., Tzioumis, A.K., Jones, D.L., King, E.A., Amy, S.W., Biggs, J.D., Blair, D.G., Campbell-Wilson, D., Clay, R.W., Costa, M.E., Edwards, P.G., Ferris, R.H., Gough, R.H., Harbison, P., Hoard, D.W., Jones, P.A., Lovell, J.E.J., Kemball, A.J., McAdam, W.B., MacCleod, G., McCulloch, P.M., Migenes, V., Murphy, D.W., Nicolson, G.D., Quick, J.F.H., Sinclair, M.W., Skjerve, L., St John, M.E., van Ommen, T., Wark, R.M., & White, G.L.
Australian Journal of Physics 47, 619-624 (1994).

5.1 Introduction

The radio source PKS 1322−427 (Centaurus A, NGC 5128) is associated with a peculiar elliptical galaxy and is the closest radio galaxy to us, at a distance of 3.5±0.2 Mpc [Hui *et al.* 1993]. Centaurus A was one of the first radio sources to be identified with an extragalactic object [Bolton, Stanley, & Slee 1949] and is

one of the brightest extragalactic radio sources in the sky with an integrated flux density of 681±34 Jy at a wavelength of 6 cm [Junkes et al. 1993]. As the closest radio galaxy, Centaurus A offers the best spatial resolution return for high angular resolution (1° ∼ 61 kpc, 1′ ∼ 1 kpc, 1″ ∼ 17 pc, and 1 mas ∼ 0.017 pc) and the most detailed view of an extragalactic radio jet on sub-pc-scales.

The entire radio source occupies approximately 3.5° × 8.5° on the sky, including the faint extended emission which is orientated along a position angle of approximately 0° [Junkes et al. 1993]. Straddling the optical galaxy along a position angle of approximately 50° and separated by approximately 15 kpc are two lobes of radio emission which have been imaged in detail with the VLA [Clarke, Burns, & Norman 1992]. An unresolved and inverted spectrum radio core which is coincident with the centre of the optical galaxy is connected to the north-east lobe by a radio jet [Burns, Feigelson, & Schreier 1983]. At the dynamic range of the existing VLA images, no jet has been found connecting the radio core to the south-west radio lobe.

VLBI observations of Centaurus A are aimed at imaging the inverted spectrum radio core. Wade et al. [1971] undertook the first high resolution radio observations of Centaurus A and reported a source less than 0.″5 in extent, although noting that the inverted spectrum of the core implied a much smaller extent. Preston et al. [1983], from 2.3 GHz VLBI observations, showed the compact core to consist of a component 50 mas in length at a position angle of 30°±20°, identifying the component as a jet which possibly aligned with the kpc-scale radio structure. Preston et al. [1983] detected no structure with spatial extent less than 0.02 pc whereas at higher frequencies a component of 0.01 pc size was known to exist. Preston et al. [1983] therefore proposed a model for the nuclear radio source in Centaurus A which consisted of two components, the 50 mas jet which is seen with low frequency observations and a more compact component likely to be the core, seen only at higher frequencies since it is severely self-absorbed at lower frequencies.

VLBI observations of Centaurus A were undertaken during the first SHEVE observing session in 1982. Meier et al. [1989] described the 2.3 and 8.4 GHz observations aimed at detecting both the compact self-absorbed core component and the 50 mas jet component. Meier et al. [1989] extended the suggested model of Preston et al. [1983] and constructed from their two-frequency observations a model for the source which consisted of a weak self-absorbed core and an extended jet component some 100 mas away which can be seen at both frequencies. The core-jet position angle was estimated to be 51°±3°, in good agreement with the jet position angle from VLA images of the kpc-scale radio structure.

In 1991, VLBI imaging observations of Centaurus A were successful for the first time at 8.4 GHz. Within only a few months significant changes were seen in the sub-pc-scale structure of Centaurus A [Meier et al. 1993; Tingay et al. 1994], in stark contrast to the results at 2.3 GHz. The observations presented in this chapter were motivated by the results of these early 8.4 GHz observations.

The contents of this chapter describe the results of the first concerted effort to monitor the radio core of Centaurus A at frequencies of 4.8 and 8.4 GHz with VLBI arrays which allow high quality images to be formed. This program of observations had two primary aims:

1] To determine the detailed sub-pc-scale structure of the nuclear radio source, especially its frequency dependent structure.

2] To follow evolution in the nuclear source on the sub-pc-scale over an extended period of time.

In § 5.2, near simultaneous observations at 4.8 and 8.4 GHz which examine the sub-pc-scale structure are presented. In § 5.3, the results of approximately 4.3 years of monitoring observations at 8.4 GHz and an examination of the evolution in the sub-pc-scale structure are presented. In § 5.4, observations combining the VLBA and SHEVE arrays which yield the highest resolution images of Centaurus A yet and show evidence for a sub-pc-scale counterjet are presented. Finally, § 5.6 presents the conclusions.

5.2   Near-simultaneous 4.8 and 8.4 GHz SHEVE observations

On 1992 November 22, 8.4 GHz VLBI observations of Centaurus A were obtained and three days later on 1992 November 25, 4.8 GHz VLBI observations were obtained with the SHEVE array. Both observations utilised similar arrays of telescopes. For the 8.4 GHz observations the participating telescopes were: Tidbinbilla (70 m), Parkes, Hobart, Narrabri, Mopra, Perth (15 m), and Hartebeesthoek. For the 4.8 GHz observations the participating telescopes were: Parkes, Hobart, Narrabri, Mopra, Perth (27 m), and Hartebeesthoek. The data were obtained and processed as described in chapter 2.
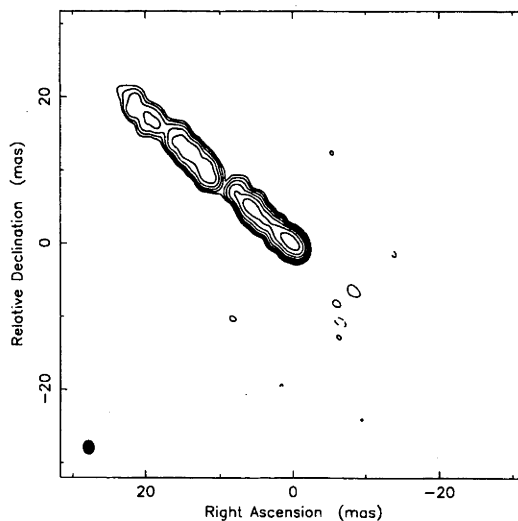
Figure 5.1: VLBI image of Centaurus A at 8.4 GHz from 1992 Nov. 22. Map peak, 1.5 Jy/beam. Contours, -1, 1, 2, 4, 8, 16, 32, 64% of peak. Beam FWHM, 1.9×1.5 mas @ 6.7°.
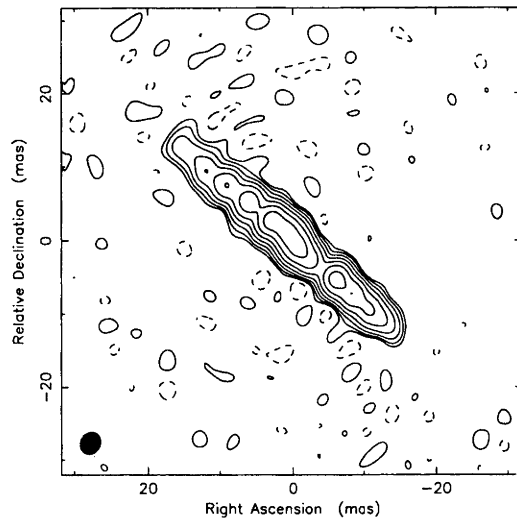
Figure 5.2: VLBI image of Centaurus A at 4.8 GHz from 1992 Nov. 25. Map peak, 0.7 Jy/beam. Contours, -1, 1, 2, 4, 8, 16, 32, 64% of peak. Beam FWHM, 3.1×2.6 mas @ -24.4°.

Several trial images were made of each data set, for instance including or excluding the data on baselines to Hartebeesthoek. Eventually the best images (Figures 5.1 and 5.2) were produced without the sparse Hartebeesthoek data.

The image at 8.4 GHz (Figure 5.1) is dominated by a bright component at the south-west end of the source, with components extending to the north-east. The structure is aligned along a position angle of 51° and has an angular length of approximately 35 mas. The bright south-west component is also the most compact, no more than 0.8 mas in extent.

The image at 4.8 GHz (Figure 5.2) is of a lower resolution than the 8.4 GHz image. The brightest component now lies midway along the source, with a further discrete component to the south-west and extensions toward both the north-east and the south-west.

The registration adopted for the images at 4.8 and 8.4 GHz is shown in Figure 5.3. The two images have been plotted on the same flux density scale after being convolved with a circular Gaussian beam of 3 mas FWHM (corresponding to the major axis length of the formal restoring beam from the 4.8 GHz image), rotated by 39° and aligned horizontally. The registration is based on two considerations. First, the relative positions and the morphologies of the components C1 and C2 are the same at 4.8 and 8.4 GHz. In particular, the component C1 is elongated and noticeably curved in both images and C1 is separated from C2 by a sharp pinching in both images. Second, the overall extent of the source at 4.8 and 8.4 GHz is the same. The bright and compact south-west component in the 8.4 GHz image is therefore aligned with the extension at the south-west end of the source in the 4.8 GHz image.

The registration adopted is consistent with the previously suggested model for the sub-pc-scale structure of Centaurus A. Meier *et al* [1989] concluded that a self-absorbed core component was seen at 8.4 GHz but missed at 2.3 GHz at the south-west end of the source, and that a strong jet component was seen at both

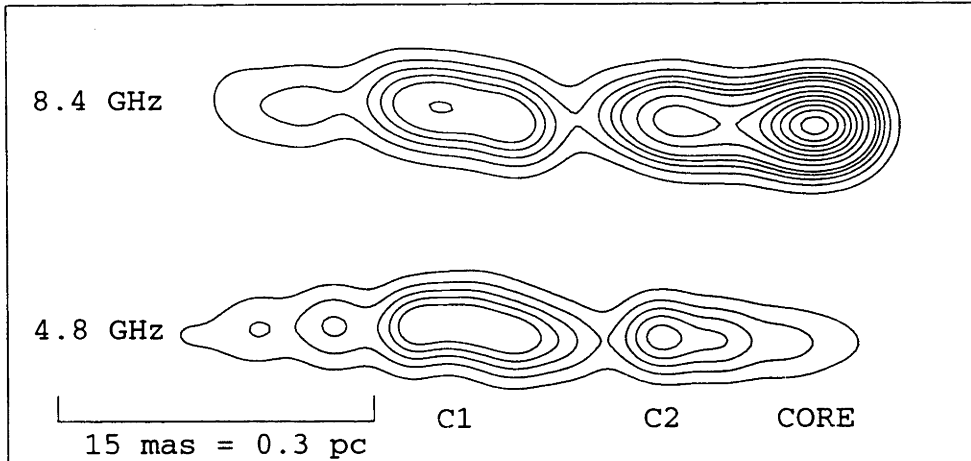
Figure 5.3: Montage peak, 2.7 Jy/beam. Contours, 5, 10, 15, 20, 25, 35, 45, 55, 65, 75, 85, 95% of peak. Beam FWHM, 3.0 mas.

frequencies. The registration for the current data shows a component with a highly inverted spectrum at the south-west end of the VLBI source, with the north-east components possessing flat to steep spectra. The inverted spectrum component is taken to be the core of the radio source which is absent from images at 2.3 GHz, but can be seen weakly at 4.8 GHz and is the brightest feature at 8.4 GHz. The remaining components comprise the sub-pc-scale jet which originates at the core and is aligned at the same position angle as the inner part of the kpc-scale jet.

From Figure 5.3, the spectral index of the core component is $\alpha = 4.1 \pm 0.4$ ($S_\nu \propto \nu^\alpha$) between 4.8 and 8.4 GHz, allowing for the 10% error in the flux density scales (see chapter 2). Jones *et al.* [1996], from simultaneous VLBA observations, also find that the core has a highly inverted spectrum between 2.3 and 8.4 GHz, $\alpha \sim 4$. The spectral index of the component C2 is $\alpha = 0.9 \pm 0.4$ and the spectral index for C1 is $\alpha = 0.3 \pm 0.4$. Here the surface brightnesses of the images have been used to estimate spectral indices since the core does not appear as a distinct component at 4.8 GHz and therefore cannot be easily de-convolved from the restoring beam.

The spectral index of the core component is too highly inverted to be explained simply by synchrotron self-absorption, which can achieve a limiting spectral index of $\alpha = 2.5$ [Rybicki & Lightman 1979]. It is possible that an additional source of absorption is causing the $\alpha > 2.5$ spectral index, namely thermal bremsstrahlung (free-free) absorption. If we assume that the intrinsic spectrum of the core component is $\alpha = 2.5$, at the limit for synchrotron radiation, then it can be argued that the additional steepening of the spectrum may be caused by a free-free absorbing structure which lies between us and the radio source. The expression for free-free absorption (e.g. Rybicki & Lightman 1979) can be used to estimate the amount of absorption, given assumptions about the electron density in the structure, its temperature, chemical composition, and the path length through the structure. Following Rybicki & Lightman [1979],

$$\alpha^\nu_{ff} = 0.018 T^{-3/2} Z^2 n_e n_i \nu^{-2} g^\nu_{ff} \ ,$$

where

$$S_{obs}^{\nu} = S_{int}^{\nu} e^{-l_{ff} \alpha_{ff}^{\nu}} \quad .$$

With an $l_{ff} = 1$ pc path length through ionised but overall electrically neutral Hydrogen (Z=1) of electron density $n_e = 10^4 = n_i$ and temperature $T = 10^4$ K, the observed spectral index between 4.8 and 8.4 GHz of $\alpha_{obs} = 4.1$ corresponds to an intrinsic spectral index, before free-free absorption, of $\alpha_{int} \sim 2.5$ (using the appropriate Gaunt factors; Karzas & Latter 1961).

There is no need to assume that C1 and C2 are free-free absorbed since their spectral indices are each less than 2.5. However, if the free-free absorption region extends beyond the core component to obscure components C1 and C2 with the same optical depth of material as is obscuring the core, unreasonably steep (in the sense of decreasing flux density with increasing frequency) intrinsic spectra are found. If assumptions are made for the intrinsic spectra of components C1 and C2, some information can be derived concerning the form of the free-free absorbing structure. An assumption which can be made is that the emission from C1 and C2 is optically thin synchrotron radiation, $\alpha_{int} = -0.6$, which suffers from no self-absorption, but only extrinsic free-free absorption.

Using this assumption and retaining the temperature, density and composition of the free-free absorbing structure constant, only a reduction in the path length (l_{ff}) need occur so that the observed spectra for these two components correspond to the assumed intrinsic spectral index of $\alpha_{int} = -0.6$. The path length required for component C2 is approximately 0.9 pc and for component C1 is approximately 0.5 pc. The path length through the free-free absorbing structure drops by a factor of two within approximately 0.4 pc of the core.

Under these assumptions the free-free absorbing structure could take the form of a torus of circular (diameter ~ 1 pc) cross section which lies perpendicular to the jet direction. To make the intrinsic spectral index of the core significantly less than the limiting value for synchrotron self-absorption ($\alpha = 2.5$) the path length through the torus, in the direction of the core, would have to be increased. In this case the torus would assume a form more resembling a thick disk. A similar situation has been noted in 3C 84 [Vermeulen, Readhead, & Backer 1994] for which a pc-scale free-free absorbing disk or torus with $l_{ff} = 3$ pc, $T \sim 10^4$ K, and $n_e \sim 1.5 \times 10^4$ may be plausible. Also, from HI observations of Cygnus A, some evidence has been found supporting the existence of a free-free absorbing torus on the scale of approximately 15 pc [Conway & Blanco 1995].

In any case, a significantly inverted intrinsic radio spectrum for the Centaurus A core appears likely. Botti & Abraham [1993] have shown that the spectrum of the nuclear radio source in Centaurus A remains inverted between 22 and 43 GHz and is variable on time-scales of a few months, evidence that flux outbursts brighten first at higher frequencies. This may partly explain the extreme spectral index of the core, as observed with VLBI.

The form and extent of the possible free-free absorbing structure in Centaurus A is uncertain since, as calculated above, it relies heavily on fairly arbitrary assumptions about the intrinsic spectra of the components in the sub-pc-scale jet and the core. However, the effect of free-free absorption at some level is almost unavoidable due to the extreme spectral index observed for the core in both the

near simultaneous imaging presented here and the simultaneous images of Jones *et al.* [1996]. This calculation is therefore a reasonable one to consider.

5.3   SHEVE 8.4 GHz monitoring observations

Between early 1991 and mid 1995, a series of nine VLBI observations were carried out with the SHEVE array (at eight epochs) and with the VLBA (at four epochs, three of which overlapped with SHEVE observations) at a frequency of 8.4 GHz. Table 5.1 summarises the series of observations and lists the telescopes participating at each epoch.

Epoch	Participating Telescopes
1991 March 6	**Ds45,Pk,Hb,Na**
1991 Nov. 24	**Ds43,Pk,Hb,Na,Mr**
1992 March 26	**Ds43,Ds45,Pk,Hb,Na,Mr,Ht**
1992 Nov. 22	**Ds43,Pk,Hb,Na,Mr,Pr15,Ht,St,Fd,Ov,Pt,Kp,La,Mk,Sc**
1993 July 3	**Ds43,Pk,Hb,Na,Mr,Pr15,Ht,Fd,Ov,Pt,Kp,La,Sc**
1993 Oct. 20	**Ds45,Pk,Hb,Na,Mr,Pr15,Ht,Fd,Ov,Pt,Kp,La,Mk,Sc**
1994 Feb. 27	**Ds43,Ds45,Pk,Hb,Na,Mr**
1994 June 20	**Ds45,Pk,Hb,Na,Mr**
1995 July 3	**Fd,Ov,Pt,Kp,La,**Nl,Mk,Sc

Table 5.1: Observation log for Centaurus A 8.4 GHz observations
Ds43 = Tidbinbilla (70 m), Ds45 = Tidbinbilla (34 m), Pk = Parkes, Hb = Hobart, Na = Narrabri, Mr = Mopra, Pr15 = Perth, Ht = Hartebeesthoek, St = Santiago, Fd = Fort Davis, Ov = Owens Valley, Pt = Pie Town, Kp = Kitt Peak, La = Los Alamos, Mk = Mauna Kea, Nl = North Liberty, Sc = Saint Croix

The high resolution SHEVE+VLBA data from 1992 November 22, 1993 July 3, and 1993 October 20 will be discussed in § 5.4. The discussion here will focus on a comparison of the lower resolution data from the nine epochs, those data obtained with the telescopes highlighted in Table 5.1.

The data from the SHEVE array were obtained and processed as described in chapter 2 to produce the images appearing in Figures 5.4 to 5.11. The image in Figure 5.12 is from VLBA data alone. The VLBA observations of 1995 July 3 were made in VLBA mode using a 32 MHz bandwidth, with single bit sampling. The data were correlated at the VLBA correlator in Soccoro then fringe-fitted with FRING in AIPS before being calibrated from system temperatures and gain-elevation curves in the Caltech VLBI package. Imaging proceeded as described in chapter 2.

Each image is dominated by the bright core component at the south-west end of the source and shows a strong jet along a position angle of 51°. The typical dynamic range achieved in imaging these data was 100:1. From a cursory inspection of the images it is clear that the source is structurally complex and changes in the source are apparent between epochs, and over the full 4.3 years of the observations. To quantify these changes a model-fitting analysis of the data was made at each epoch. The models were then compared to obtain some understanding of the structure and evolution in Centaurus A on the sub-pc-scale during this period and in an attempt

to quantify the effects of the (sometimes significant) differences in the $u - v$ coverage between the epochs.

5.3.1   Model-fitting technique

To model-fit each of the 8.4 GHz datasets the Caltech VLBI task MODELFIT was utilised. MODELFIT uses a non-linear least-squares algorithm to fit the parameters of a set of simple components in the image plane (a model) to the visibility amplitudes and closure phases of the VLBI data and reports a measure of the goodness-of-fit (defined as the square root of the reduced chi-square value for the fit of the model to the data). MODELFIT can undertake a gradient search for the best match of model to data by finding the gradient of the goodness-of-fit function and adjusting the parameters of the model so that the gradient is followed towards the local minimum. A brute force method is also available which finds the best match of model to data by adjusting each of the model parameters individually and in turn, to minimise the goodness-of-fit.

The models initially chosen to represent the source were a minimum representation of the main features which could be seen in the images; the core and components C1 and C2, with flux densities, separations, position angles, and component extents estimated from the images.[1] These starting models, along with the corresponding self-calibrated data from the imaging process, formed the input to the MODELFIT program. Initially the gradient search mode was used, allowing only one parameter to vary, the core flux density, and then one by one the flux densities of the remaining components. Then the other parameters of the model components were allowed to vary, one by one, during individual runs of MODELFIT. Once this process was complete all of the model parameters were allowed to vary together with full freedom in the gradient search mode, and then finally, using the brute force method to ensure convergence.

In all cases, the resulting model did not fit the data well and the inclusion of further model components was required at each epoch. Guided once more by the images, single components were added to the starting models and the model-fitting process initiated once more from first principles. Again when the model-fitting was completed, the data at some epochs was still not well fit by the models. Again another component was added to the starting models at these epochs and model-fitting initiated a third time.

In this way, good fits to the visibility amplitudes and closure phases of the data at all nine epochs were finally obtained. At four epochs, models with 4 components were required, and at five epochs, models with 5 components were required. Thus the data could consistently be quantified with a reasonably small number of parameters, considering the degree of complexity of the source. Accompanying each of the images in Figures 5.4 to 5.12 are the best fit models for the structure of the source. Each model consists of a number of components which are identified in the right hand column of each table. Each component has 7 parameters associated with it:

---

[1]The core component was always held at the origin of the image plane during model-fitting since the absolute position of the source is lost during the fringe-fitting and self-calibration processes. As a result, MODELFIT returns the relative positions of the components in the source.

S (Jy)   -   The integrated flux density of the model component in Jy.

d (mas)   -   The distance of the model component centroid from the designated phase centre in milliarcseconds.

$\theta°$ -   The position angle of the model component centroid from the designated phase centre in degrees east from north.

A (mas)   -   The major axis extent of the model component in milliarcseconds.

B/A   -   The ratio of model component minor axis extent to major axis extent.

$\phi°$ -   The position angle of the model component major axis in degrees east from north.

Type   -   The type of model component. Type 1 components are elliptical Gaussians, in which case component extents are the FWHM of the Gaussian. Type 2 components are elliptical disks of uniform surface brightness, in which case component extent is the full extent. This is a non-variable parameter in MODELFIT.
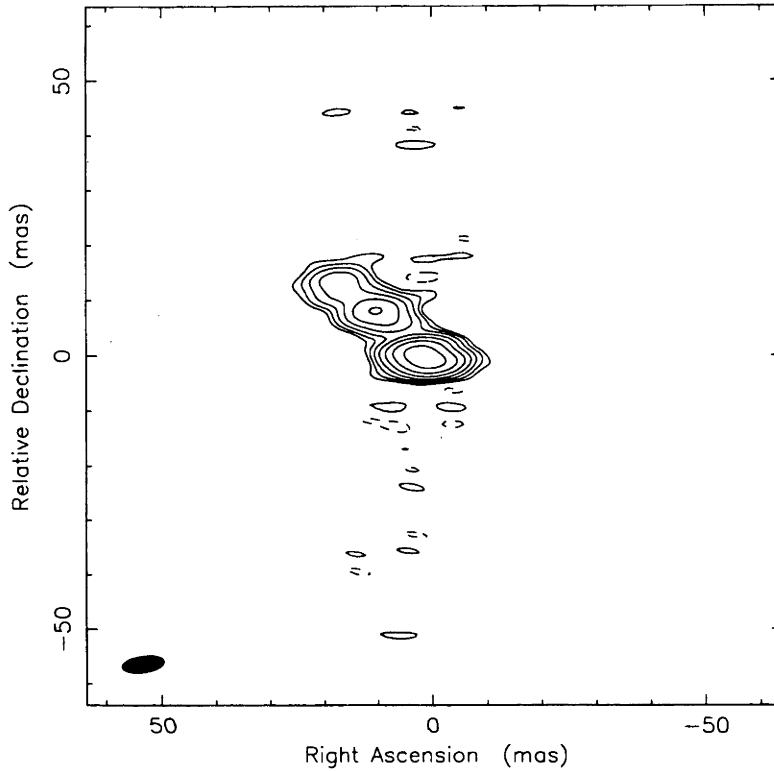
Figure 5.4: VLBI image of Centaurus A at 8.4 GHz from 1991 March 6. Map peak, 3.0 Jy/beam. Contours, -1, 1, 2, 4, 8, 16, 32, 64% of peak. Beam FWHM, 7.6×3.0 mas @ -81.7°.

S (Jy)	d (mas)	$\theta°$	A (mas)	B/A	$\phi°$	Type	I.D.
2.34	0.00	0.0	2.94	0.00	73.6	1	Core
2.93	3.47	53.1	2.62	0.27	66.9	1	C2
1.65	14.39	49.5	4.08	0.68	52.4	1	C1
0.73	22.97	51.3	3.94	0.15	21.8	1	C1/Jet

Table 5.2: Best fit model for Centaurus A data from 1991 March 6

Figure 5.5: VLBI image of Centaurus A at 8.4 GHz from 1991 Nov. 24. Map peak, 2.7 Jy/beam. Contours, -1, 1, 2, 4, 8, 16, 32, 64% of peak. Beam FWHM, 7.2×3.0 mas @ -89.3°.

S (Jy)	d (mas)	$\theta°$	A (mas)	B/A	$\phi°$	Type	I.D.
2.18	0.00	0.0	2.74	0.11	37.6	1	Core
2.75	4.35	51.2	2.84	0.53	42.6	1	C2
1.22	12.79	52.2	4.59	0.32	41.5	1	C1/Jet
1.47	20.46	49.1	12.58	0.00	47.1	1	C1/Jet
0.60	32.54	49.5	35.02	0.00	46.5	2	Jet

Table 5.3: Best fit model for Centaurus A data from 1991 Nov. 24

Figure 5.6: VLBI image of Centaurus A at 8.4 GHz from 1992 March 26. Map peak 2.5 Jy/beam. Contours, -0.5, 0.5, 1, 2, 4, 8, 16, 32, 64%. Beam FWHM, 8.7×3.0 mas @ 82.6°.

S (Jy)	d (mas)	$\theta°$	A (mas)	B/A	$\phi°$	Type	I.D.
2.40	0.00	0.0	2.04	0.00	62.1	1	Core
1.83	4.75	51.7	2.30	0.00	65.7	1	C2
3.02	15.92	49.5	9.86	0.17	47.8	1	C1
1.02	28.15	51.5	32.90	0.00	45.1	2	Jet

Table 5.4: Best fit model for Centaurus A data from 1992 March 26
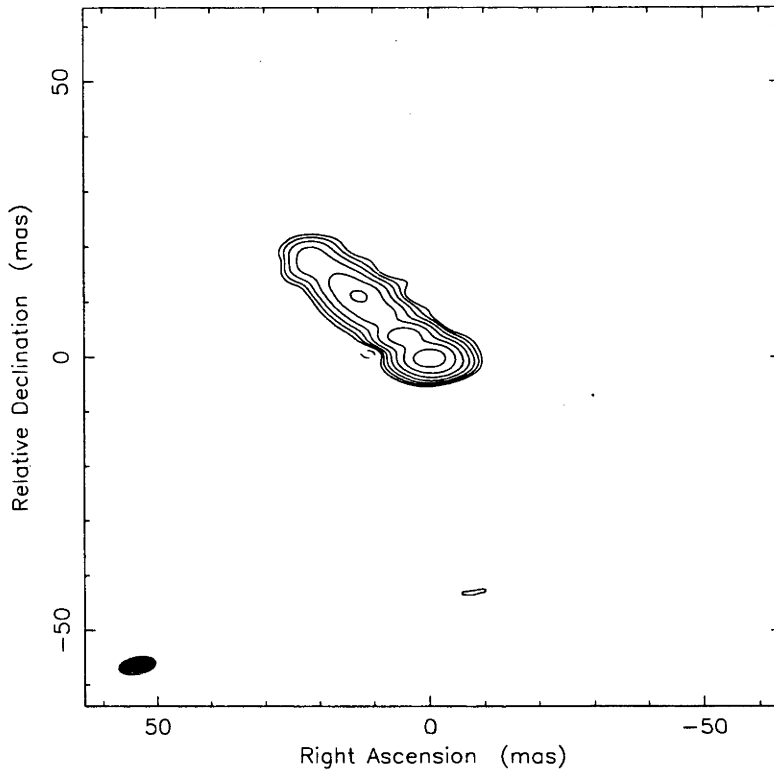
Figure 5.7: VLBI image of Centaurus A at 8.4 GHz from 1992 Nov. 22. Map peak, 3.1 Jy/beam. Contours, -1, 1, 2, 4, 8, 16, 32, 64%. Beam FWHM, 6.9×3.1 mas @ -79.6°.

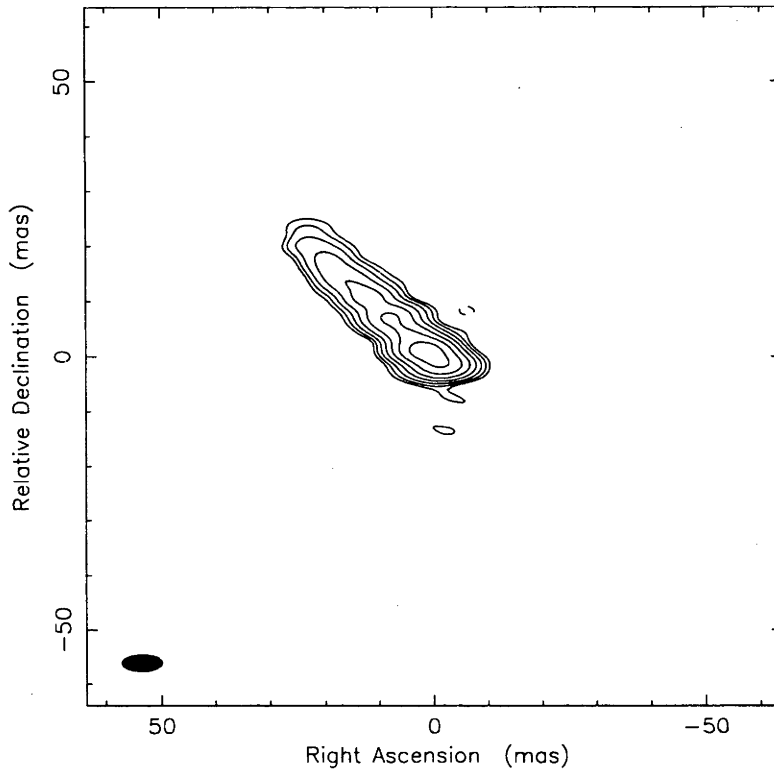| S (Jy)	d (mas)	$\theta°$	A (mas)	B/A	$\phi°$	Type	I.D.
3.31	0.00	0.0	2.90	0.18	50.8	1	Core
1.17	6.35	50.5	3.17	0.00	56.4	1	C2
1.05	16.96	47.9	5.42	0.00	32.8	1	C1
4.53	14.4	50.4	37.4	0.00	48.7	2	Jet

Table 5.5: Best fit model for Centaurus A data from 1992 Nov. 22
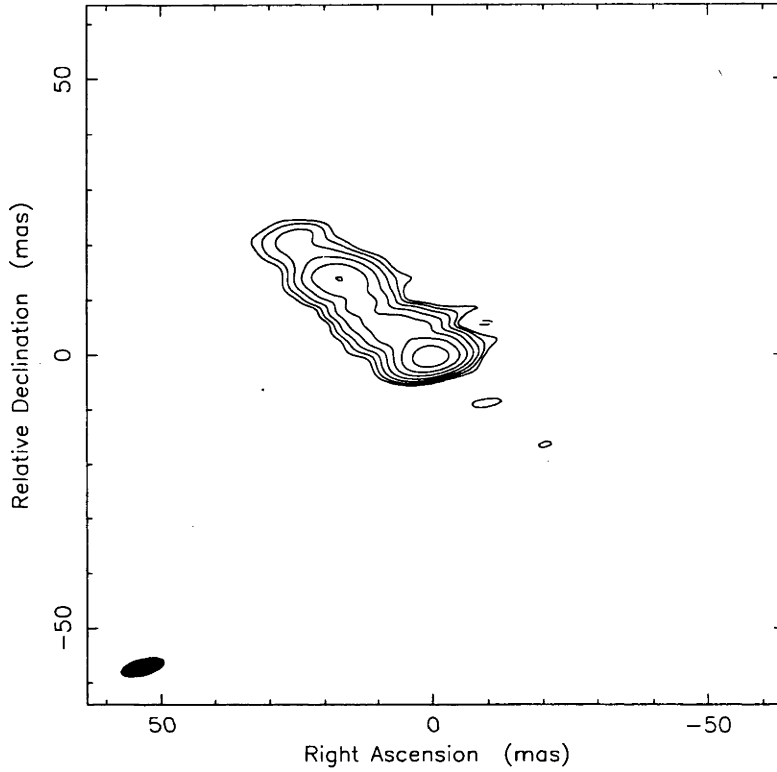
Figure 5.8: VLBI image of Centaurus A at 8.4 GHz from 1993 July 3. Map peak, 1.7 Jy/beam. Contours, -1, 1, 2, 4, 8, 16, 32, 64%. Beam FWHM, 8.0×3.0 mas @ -74.6°.

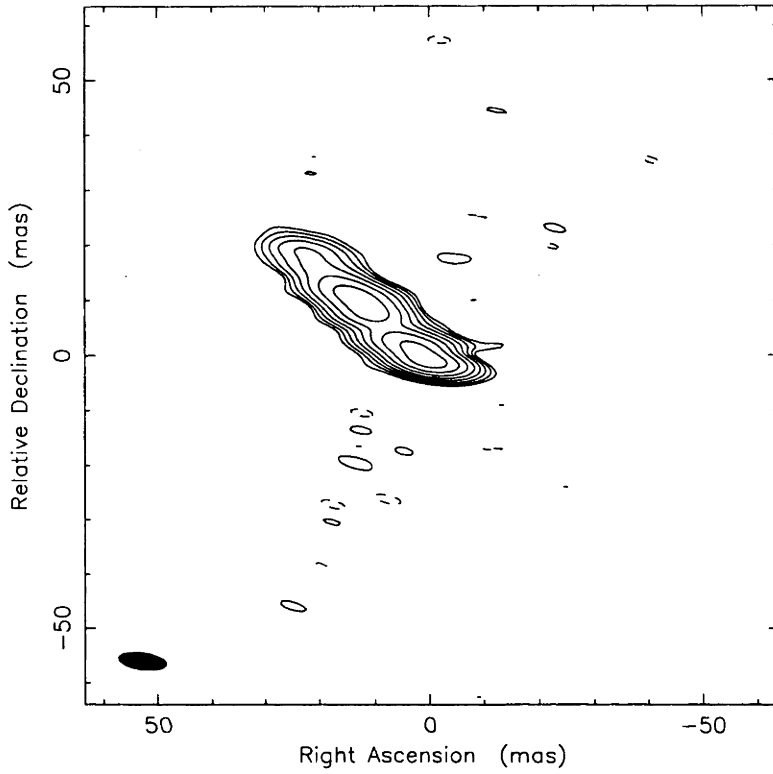| S (Jy)	d (mas)	$\theta°$	A (mas)	B/A	$\phi°$	Type	I.D.
2.30	0.00	0.0	3.65	0.00	49.6	1	Core
0.69	6.34	46.3	7.76	0.31	69.7	1	C2
1.93	15.00	50.2	25.96	0.14	49.9	1	Jet
0.26	16.46	56.6	6.45	0.00	0.11	1	C1/Jet
0.52	22.53	49.9	3.77	0.00	55.2	1	C1/Jet

Table 5.6: Best fit model for Centaurus A data from 1993 July 3
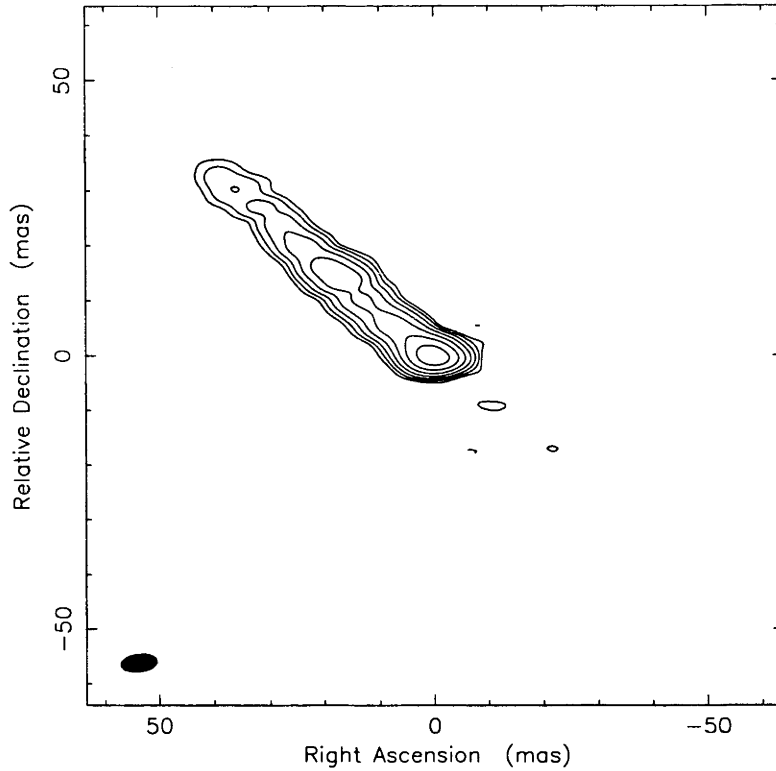
Figure 5.9: VLBI image of Centaurus A at 8.4 GHz from 1993 Oct. 20. Map peak, 2.4 Jy/beam. Contours, -1, 1, 2, 4, 8, 16, 32, 64%. Beam FWHM, 6.8×3.2 mas @ -83.1°.

S (Jy)	d (mas)	$\theta°$	A (mas)	B/A	$\phi°$	Type	ID
2.35	0.00	0.0	1.86	0.00	56.5	1	Core
1.05	3.16	49.1	0.00	0.37	40.0	1	C3
1.20	8.36	52.4	6.91	0.00	54.1	1	C2
2.39	22.69	50.3	13.7	0.00	45.4	1	C1
0.71	42.54	50.4	19.37	0.12	45.2	1	Jet

Table 5.7: Best fit model for Centaurus A data from 1993 Oct. 20
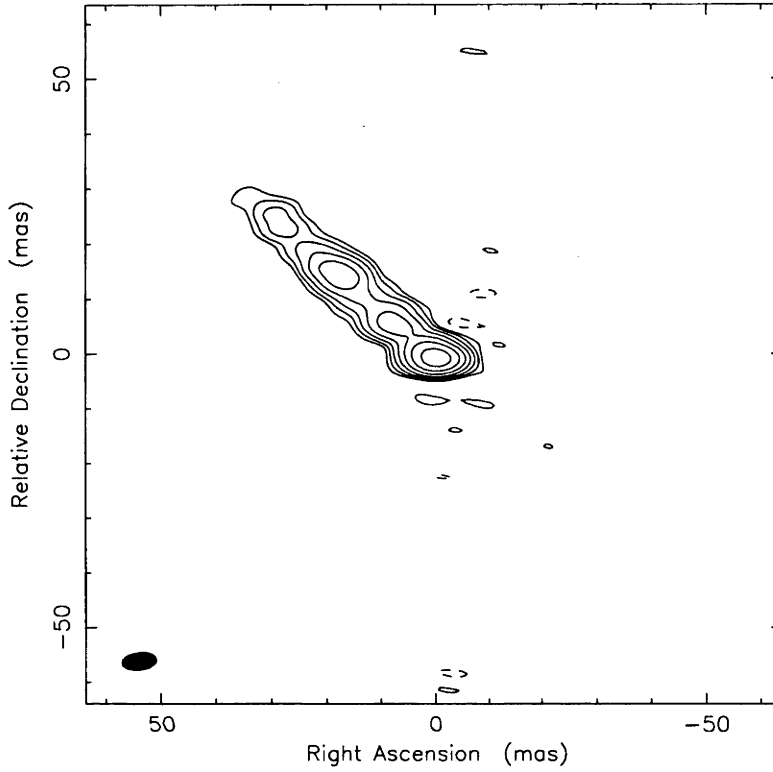
Figure 5.10: VLBI image of Centaurus A at 8.4 GHz from 1994 Feb. 27. Map peak, 2.6 Jy/beam. Contours, -1, 1, 2, 4, 8, 16, 32, 64%. Beam FWHM, 6.3×3.2 mas @ -83.3°.

S (Jy)	d (mas)	$\theta°$	A (mas)	B/A	$\phi°$	Type	I.D.
3.26	0.00	0.0	3.20	0.00	60.1	1	Core
0.36	3.60	40.8	0.00	0.00	59.7	1	C3
1.21	10.27	52.3	6.00	0.00	43.6	1	C2
1.39	22.82	49.3	6.83	0.17	45.8	1	C1
0.73	35.00	50.6	20.1	0.11	46.5	1	Jet

Table 5.8: Best fit model for Centaurus A data from 1994 Feb. 27
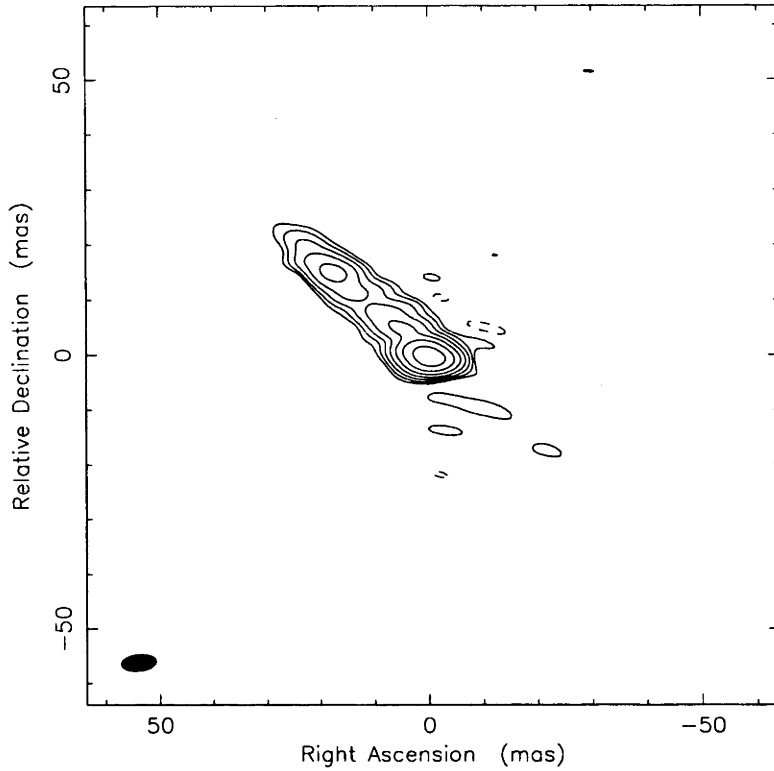
Figure 5.11: VLBI image of Centaurus A at 8.4 GHz from 1994 June 20. Map peak, 2.1 Jy/beam. Contours, -1, 1, 2, 4, 8, 16, 32, 64%. Beam FWHM, 6.4×3.0 mas @ -84.2°.

S (Jy)	d (mas)	$\theta°$	A (mas)	B/A	$\phi°$	Type	I.D.
1.97	0.00	0.0	2.04	0.00	45.8	1	Core
1.05	2.91	50.6	1.58	0.68	31.5	1	C3
0.81	9.44	47.3	9.09	0.00	48.1	1	C2
0.78	16.31	53.5	38.22	0.00	47.7	1	Jet
0.87	24.20	49.0	9.38	0.19	57.3	1	C1

Table 5.9: Best fit model for Centaurus A data from 1994 June 20
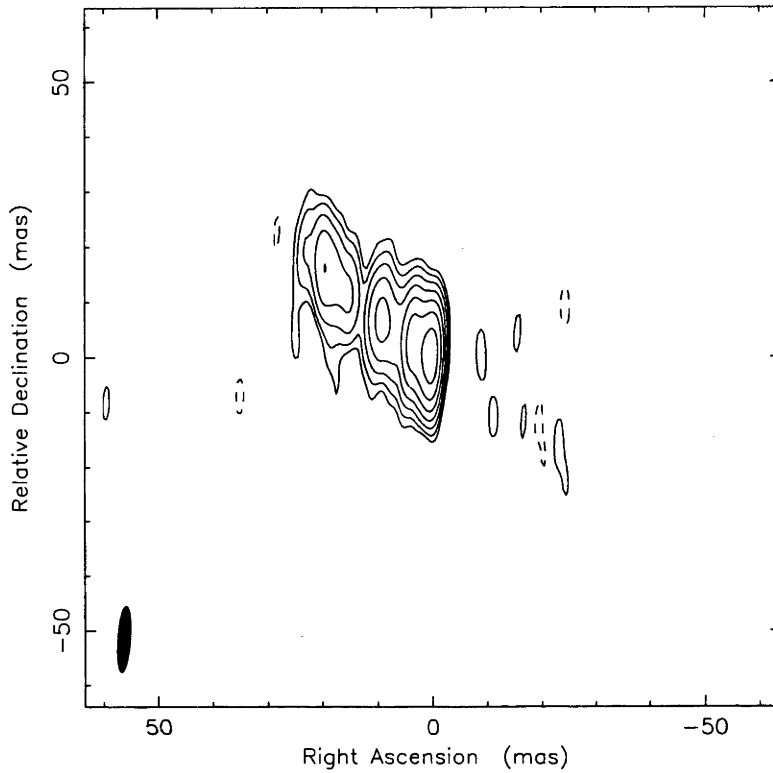
Figure 5.12: VLBI image of Centaurus A at 8.4 GHz from 1995 July 3. Map peak, 4.1 Jy/beam. Contours, -1, 1, 2, 4, 8, 16, 32, 64%. Beam FWHM, 12.2×2.3 mas @ -4.2°.

S (Jy)	d (mas)	$\theta°$	A (mas)	B/A	$\phi°$	Type	I.D.
5.66	0.00	0.0	2.62	0.70	35.9	1	Core
2.72	4.51	44.7	3.15	0.77	148.4	1	C3
1.82	11.04	52.5	4.80	0.49	52.8	1	C2
2.04	23.36	50.88	11.00	0.11	34.2	1	C1

Table 5.10: Best fit model for Centaurus A data from 1995 July 3

5.3.2   Structure and evolution from model-fitting

The core component appears strongly in each of the models. The component C2 can also be identified at each epoch. The component C1 can be identified at seven of the nine epochs. At two epochs, 1991 November 24 and 1993 October 20, it is not clear which, if any, of the model components corresponds to C1. In the last four epochs, an additional component can be identified between the core and C2, and is designated C3. Lastly, at eight of the nine epochs one or more of the components in the models have been identified as possible or definite jet-like components. These components are often required by the model to take an extended (elongated along the jet) and diffuse appearance, in contrast to the discrete components. Such a component was first noted by Meier *et al.* [1989] in their modelling of the first 8.4 GHz VLBI observations of Centaurus A. This component probably represents the underlying, smooth emission from the jet.

The main aim of the model-fitting analysis was to quantify the evolution of the components in the source. To achieve this aim further analyses of the models were undertaken to estimate the errors on the best-fit parameters at each epoch. The model-fitting errors are required so as to determine whether or not the differences between the different models are significant.

To estimate errors, the best-fit model at a given epoch and its corresponding dataset were taken back into the MODELFIT program. The best-fit value for a single parameter of a given component in the model was then altered by a certain amount and fixed at the new value. MODELFIT was then allowed to re-converge the model with all parameters varying, except for the parameter which had been fixed and the position of the core. First the gradient search method was employed and then the brute force method immediately afterwards. When the model had re-converged to its new goodness-of-fit (worse than for the best fit model), its fit to the visibility amplitudes and closure phases was compared to the fit of the best-fit model. The Caltech VLBI task VPLOT was used to plot the data against the model predictions and a visual comparison of the two fits was made. If no significant difference could be found between the fit of the two models then the process was repeated, after the parameter in question had been fixed again at a new, larger displacement from its best-fit value.

When a displacement was reached at which the fit of the re-converged model to the data was significantly worse than for the best-fit model, the displacement defined the error bar in one direction. Displacements in the opposite sense were used to define the error bar in the opposite direction.

The comparison of model fits was necessarily a subjective one. However, several ground rules were established for the purposes of deciding whether a difference between fits was significant or not. First, none of the fits were perfect, there were differences between model and data on some baselines and closure triangles in every data set. The baselines and closure triangles which were very well fit by the best-fit model were most closely monitored in the error determination process. The fit was deemed to be significantly worse than the best-fit if the model prediction was outside the scatter in the visibilities for periods longer than 2 hours on 2 or more baselines and/or closure triangles which were well fit by the best-fit model, and if further steps away from the best-fit solution caused even greater divergence from the data. Otherwise any differences in the fits were deemed not significant.

This method can be applied to any of the parameters in the models. However, the analysis was successful only in its application to the core-component separations for the discrete components in the source, namely C1, C2, and C3. For example, from an analysis of the errors on the flux densities of individual components it became clear that the various components in a given model were easily able to "trade" flux density in a way which satisfied the MODELFIT program over a large range in displacement from best-fit values, giving no useful estimate of the errors. The core-component separations for the discrete components were the best constrained parameters, probably because the closure phase information maintained a strong influence.

Even for the core-component separations it would appear that this method is near the limit of its usefulness for this source. It was noted that the core-component separation could be systematically compensated by the core-component position angle to retain a good fit to the data over a (sometimes) wide range in displacement.

Figure 5.13 presents the results of the model-fitting error analysis for the core-component separations of C1, C2, and C3 and shows that components C1 and C2 have significantly changed their positions relative to the core over the 4.3 years of the monitoring. A least-squares fit to the series of core-C2 separations gives an angular motion for C2 relative to the core of 1.9 ± 0.4 mas/yr corresponding to an apparent speed of $\beta_{app}=v_{app}/c=0.12 \pm 0.03$, with small residuals at most epochs. Extrapolating the motion back in time gives a core-C2 zero separation time of approximately 1989.5.

A least squares fit to the core-C1 separations gives an angular motion for C1 relative to the core of 2.6 mas/yr, corresponding to $\beta_{app}=v_{app}/c=0.16$. However, the residuals on this fit are large at most epochs and it appears that a single, constant expansion speed may not be the best description for the evolution of this component. From the visibility data, the images, and the models, it is apparent that C1 undergoes strong internal evolution.

Over the period of the first three epochs (1991 March 6 to 1992 March 26) C1 changed its structure appreciably, from being a discrete component at 1991 March 6 (see images and model) to being possibly absent from the source model at 1991 November 24, and returning as a bright and discrete component some time during the following 4 months to 1992 March 26 [Meier *et al.* 1993; Tingay *et al.* 1994]. The evolution between 1991 November 24 and 1992 March 26 could be characterised by the appearance of a component within C1 approximately 0.3 ly (4.5 mas) in projected extent (from a comparison of the models) over the 0.34 year period (Figure 5.14). Also between the epochs of 1992 November 22 and 1993 October 20, C1 altered its appearance considerably. C1 appears to have increased its separation from the core by approximately 0.4 ly (6 mas) over the 0.9 year period, remaining close to that separation until the end of the series of observations. This change in position is significant, as can be seen in Figure 5.13.

From the two episodes of evolution in C1, and assuming that the changes seen are the result of component motions, lower limits on the speed of 0.85c and 0.45c can be inferred respectively. These speeds are much greater than inferred from the long term monitoring. The behaviour of C1 appears to be accounted for by a slow, linear motion combined with internal changes on much shorter time-scales, < 4 months.
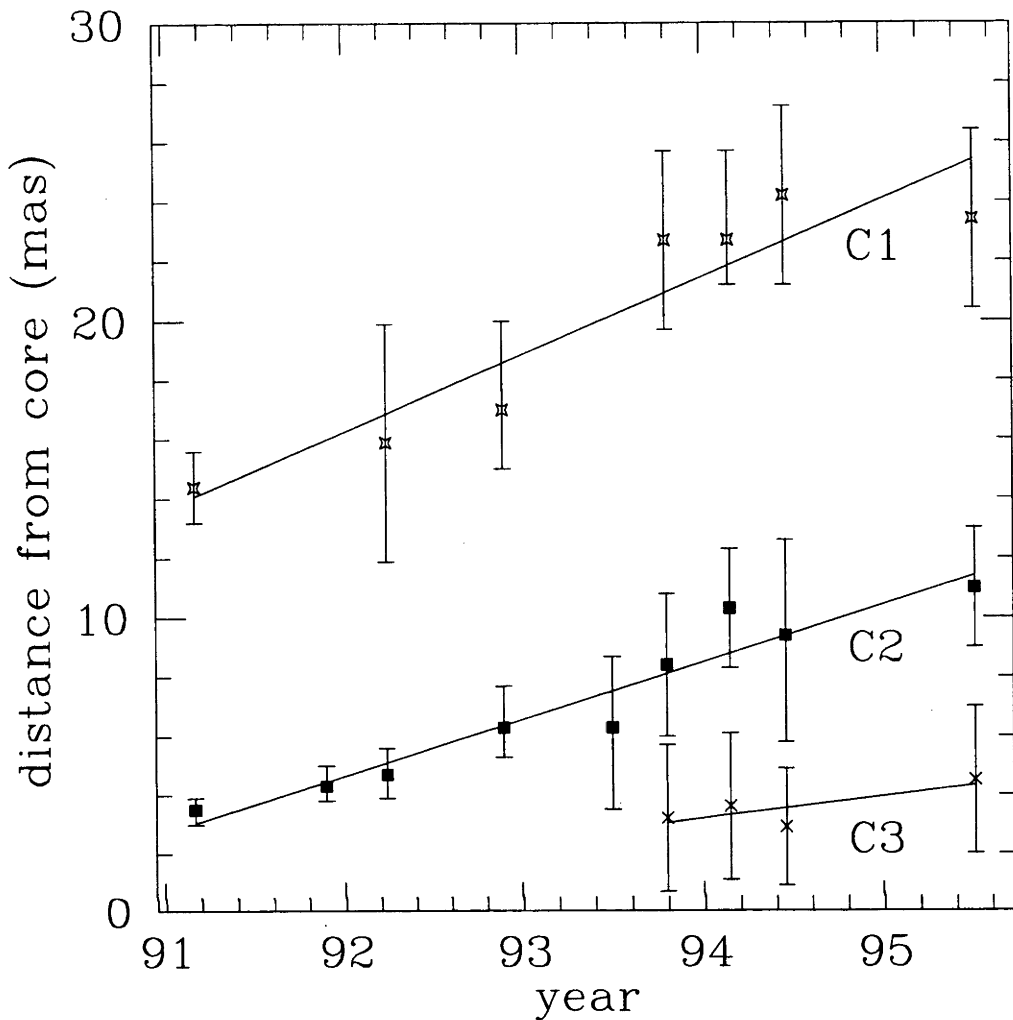
Figure 5.13: Evolution of major model components

The component C3 was only detected in the last four epochs of observation and the error bars do not indicate any significant motion, but it might be expected that with further observations C3 will be shown to have a motion with respect to the core similar to C2.

5.3.3 Effects of $u - v$ coverage variation

The model-fitting analyses have shown that the prominent, discrete components in the source can consistently be identified despite changes in the details of the VLBI array used and variations in the resulting $u - v$ coverage. The model-fitting has also shown that the component of the source which is most sensitive to variations in the array and its $u - v$ coverage is the component used to represent the smooth, diffuse and extended jet emission underlying the discrete components C1, C2, and C3.

For example, on 1991 March 6 when four telescopes were available, only one baseline was observing in the range of hour angles when the source position angle was aligned with the primary interferometer fringe, allowing the full flux density of

Figure 5.14: Comparison of 1991 Nov. 24 and 1992 March 26 models

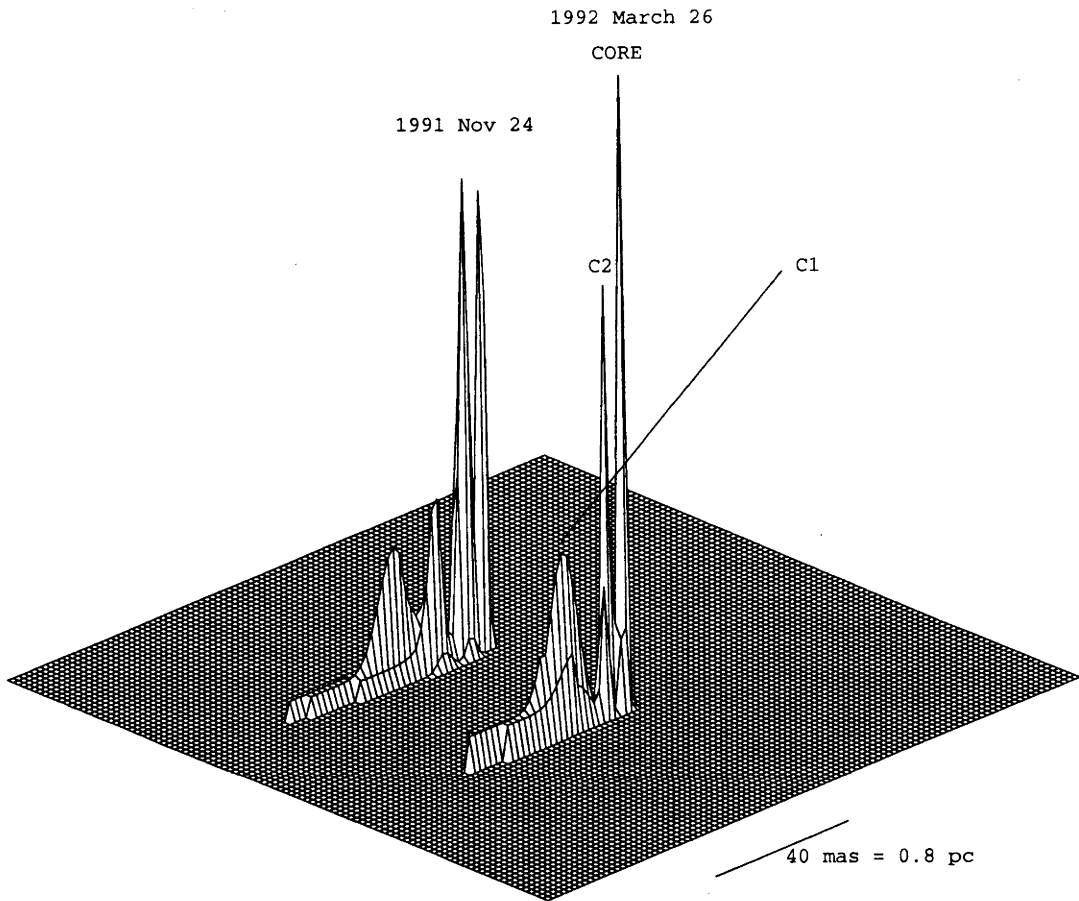the source to be measured. This lack of constraint on the underlying jet emission caused it to be essentially absent from the image and the model (Figure 5.4, Table 5.2). The discrete components in the source produced structure in the visibilities at other hour angles and were, therefore, well constrained in the image and model.

Conversely, at 1992 November 22 and 1993 October 20, when five telescopes were available and almost all baselines observed the source to cross the primary interferometer fringe, many constraints on the total flux density were obtained, allowing the underlying jet to be imaged and modelled (Figures 5.7 and 5.9, Tables 5.5 and 5.7). Thus the appearance and prominence of the jet-like component in both the images and the models is strongly related to details of the $u - v$ coverage.

To achieve a uniform comparison of the data at each epoch, Figure 5.15 shows the 8.4 GHz images, each rotated by 39°. The images have been aligned on the core component and the vertical space between each pair of images is proportional to the temporal difference between epochs. Each of the eight SHEVE images have been convolved with a beam (8.7 × 3.2 mas @ −83°) which is the average of the eight original beams, and plotted on a common flux density scale, with a peak flux density of 3.3 Jy/beam. The ninth epoch, with VLBA telescopes only, requires a

completely different beam (12.2 × 2.3 @ −4.2°). The peak flux density in this last image is 4.1 Jy/beam. The lowest contour in the montage was chosen to be 5% of the peak since most of the effects of differing $u - v$ coverage on the underlying jet appear below this level and the discrete components are prominent above this level. The contour levels are 5, 10, 15, 20, 25, 35, 45, 55, 65, 75, 85, and 95% of 3.3 Jy/beam for the first eight images and of 4.1 Jy/beam for the ninth image.

Marked on Figure 5.15 is the position of the core and the 0.12c motion of component C2. For comparison, a 0.12c motion is also shown for component C1. The internal evolution in C1 is visible from epoch to epoch. At the end of the series of images, the new component C3 can be clearly seen as an extension to the core in the VLBA image.
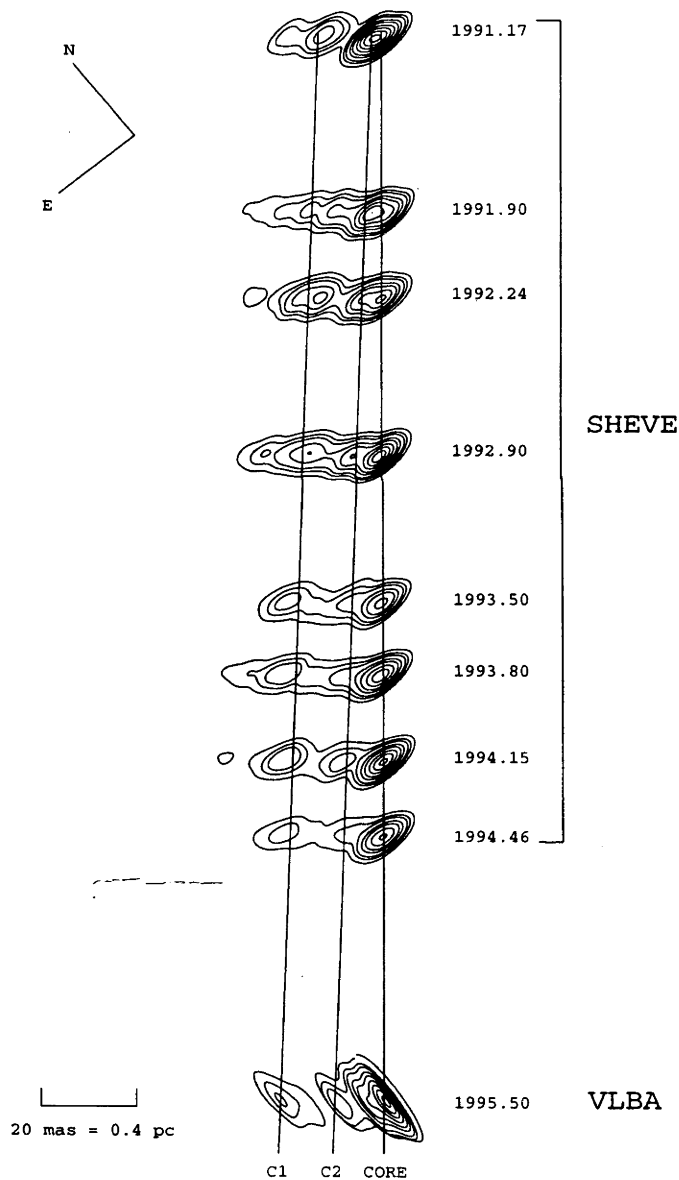

Figure 5.15: 4.3 year sequence of 8.4 GHz Centaurus A observations

5.4   Combined SHEVE+VLBA observations

As indicated in Table 5.1, at the epochs of 1992 November 22, 1993 July 3, and 1993 October 20, the SHEVE observations were made jointly with the VLBA. These simultaneous observations were designed to improve the $u - v$ plane coverage for Centaurus A. The SHEVE array coverage of Centaurus A is generally north-south, missing east-west coverage. On the other hand, the VLBA telescopes which can observe to the declination of Centaurus A produce an east-west coverage. Thus, treating the SHEVE array and the VLBA as two sub-arrays and combining the data in the $u - v$ plane, more detailed and reliable VLBI images can be obtained.

The VLBA data were obtained in Mark III mode and correlated at the VLBA correlator in Soccoro. The data obtained from 1993 July 3 are not yet available from the correlator. The VLBA and SHEVE data were fringe-fit and calibrated separately and merged together as two sub-arrays using the Caltech VLBI package task MERGE. The signal to noise match between the Mark II SHEVE data and the Mark III VLBA data was good since the SHEVE array was anchored by the 64 m antenna at Parkes and the 70 m antenna at Tidbinbilla. The visibility weights did not require adjustment.

5.4.1   The sub-pc-scale counterjet

The image resulting from the SHEVE+VLBA observations of 1992 November 22 can be seen in Figure 5.16. The structure can still be seen to consist of the familiar core component and components C1 and C2, with an underlying smoother jet. However, an additional component appears to the south-west of the core component which is not seen in the images from SHEVE data alone (Figures 5.1 and 5.7).
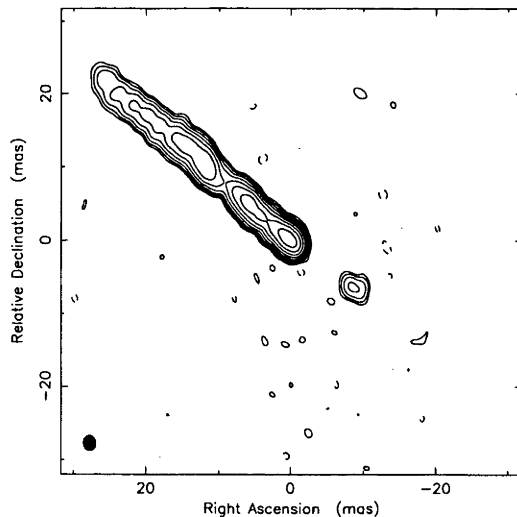

Figure 5.16: SHEVE+VLBA image of Centaurus A from 1992 Nov. 22. Map peak, 1.6 Jy/beam. Contours, -0.5, 0.5, 1, 2, 4, 8, 16, 32, 64% of peak. Beam FWHM, 2.2×1.7 mas @ 5.4°.
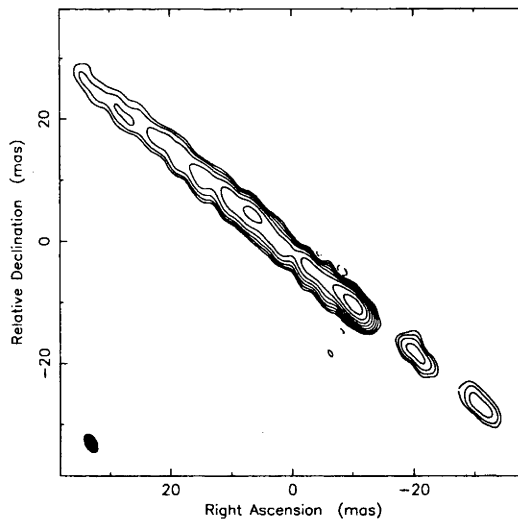
Figure 5.17: SHEVE+VLBA image of Centaurus A from 1993 Oct. 20. Map peak, 1.8 Jy/beam. Contours, -0.5, 0.5, 1, 2, 4, 8, 16, 32, 64% of peak. Beam FWHM, 3.3×1.9 mas @ 27.3°.

In the image resulting from the 1993 October 20 observations (Figure 5.17) even more structure can be seen to the south-west of the core component. In this image two components lie along the position angle of the jet.

The structure to the south-west of the core appears weaker than the main emission and this is essentially the reason why it was missed in imaging SHEVE-only datasets. The improvement in $u - v$ coverage gained by combining the SHEVE and VLBA data allowed the weak components to appear strongly during the imaging process, becoming the brightest features in the residual dirty images following each iteration of clean and self-calibration, after the bright emission had been cleaned. During the imaging of the SHEVE-only data, these weak residual features appear only marginally above the noise level and can easily be missed or ignored if the imager is conservative and the clean windows are restricted to the core and the components north-east of the core.

To test the reality, or otherwise, of the features south-west of the core, many trial images of these data were made in an attempt to produce a good image *without* the additional features, but all attempts were unsuccessful. The features remained the strongest after each iteration near the end of the imaging procedure and the inclusion of the features in the clean model always greatly improved the agreement between model and data.

Additional trials were conducted which involved the use of datasets produced with the Caltech VLBI task FAKE. Simulated data were produced using various combinations of SHEVE and VLBA telescopes and a variety of different source models. These trials were undertaken on a blind basis with one person producing the FAKE data and another producing the images with no knowledge of the source model used for the data. In each case, the trials showed that no spurious features were added and all real features were found.

A final trial was made, allowing three independent investigators to image the real datasets. All three agreed in the existence of the features.

The two images in Figures 5.16 and 5.17 nonetheless have a difference. At 1992 November 22, only one additional component was revealed, but at 1993 October 20, two additional components were revealed. This difference is primarily due to the difference in data quality between the two epochs, with the 1993 October 20 data being of a higher quality. Two telescopes also needed to be removed from the 1992 November 22 dataset due to equipment failures, leading to a difference in the $u-v$ coverage. However the second additional component, furtherest from the core toward the south-west at 1993 October 20 is weakly apparent in the 1992 November 22 image if its existence is assumed *a priori*. Consistent with the discussion of the imaging philosophy adopted here (see Chapter 2), that each data set be considered strictly upon its merits, the second component was not well enough constrained to appear in the 1992 November 22 image and was therefore excluded from the clean windows.

The additional features, seen best in Figure 5.17, can be interpreted as evidence for a sub-pc-scale counterjet emerging from the core toward the south-west. The counterjet appears much weaker than the main jet. This may be due to a combination of the effects of relativistic beaming and the effects of the possible free-free absorbing structure discussed earlier. Presumably the images show just the brightest portions of the counterjet emission (analagous to the bright components C1 and C2 in the main jet) and the smoother underlying jet emission may be too faint to be detected.

Using Figure 5.17 and correcting for the free-free absorbing structure discussed in § 5.2, an estimate of the intrinsic jet to counterjet surface brightness ratio (R) can be found. The jet to counterjet surface brightness ratio is defined here as the ratio of the brightest jet feature to the brightest counterjet feature. For Centaurus A on the sub-pc-scale, the intrinsic (corrected) ratio is $R \sim 3$.

The equation describing the jet to counterjet surface brightness ratio due to relativistic beaming is

$$R = \left(\frac{1 + \beta cos\theta}{1 - \beta cos\theta}\right)^{3-\alpha}$$

for a spherical component of emission. β is the speed of the radiating material, θ is the angle the motion of the material makes to our line of sight, and α is the spectral index ($S \propto \nu^\alpha$). Using the assumption of $\alpha = -0.6$ as in § 5.2 and the corrected jet to counterjet brightness ratio, R, then $\beta cos\theta = 0.15$. Now, with the various estimates for the speed of material in the jet from the model-fitting analysis in § 5.3.2, the jet angle to the line of sight can be estimated.

With the subluminal ($\beta_{app} = 0.12 \pm 0.03$) speed for component C2, a solution for $\beta cos\theta = 0.15$ can just be found, the minimum speed required for a solution being $\beta = 0.15$. However, the angle to the line of sight for the jet in this case is $0°$, not in good agreement with the large-scale structure of the radio source. For the faster speeds implied from the episodic rapid evolution, $\beta_{app} > 0.85$ and $\beta_{app} > 0.45$, solutions for θ of $> 80°$ and $> 70°$ respectively can be found, with an upper limit of $\theta = 81°$ (for $\beta = 1$). These large values for the angle to the line of sight are in agreement with the extended morphology of the kpc-scale radio source and the optical morphology of the host galaxy.

Therefore, it may be that the rapid evolution occasionally seen in Centaurus A is indicative of the motion of material in the jet, with the subluminal components

perhaps representing the motion of slower and longer lived patterns in the jet. It follows that the temporal frequency at which the sub-pc-scale structure of Centaurus A has been monitored is such that this rapid evolution may be under-sampled and that other episodes of rapid variability may have gone unobserved.

5.5 Conclusions

The frequency-dependent model for the structure of the Centaurus A VLBI source, first suggested by Preston *et al.* [1983] and extended by Meier *et al.* [1989], has been confirmed here with the first simultaneous VLBI observations at 4.8 and 8.4 GHz. These observations allow the unambiguous identification of the core of the radio galaxy, which has a highly inverted spectrum between 4.8 and 8.4 GHz. The remaining components in the sub-pc-scale jet have less inverted or flat spectra.

The first extensive monitoring of the sub-pc-scale structure of Centaurus A has been presented. The results of the monitoring show that the source consists of a number of discrete components in an underlying smooth jet. One of these components, C2, is moving with a subluminal apparent speed of approximately 0.12c, away from the core of the source along the position angle of the jet and appears to have been ejected from the core in mid 1989. Another component, C1, lies further from the core than C2 and may also be travelling with a similar subluminal speed, but episodes of strong internal evolution have been observed in C1 which complicate the interpretation in terms of a simple linear motion. It seems likely that the evolution of C1 is due to the combination of a slow linear motion and strong internal evolution on time-scales as short as a few months. The component C3 appears to have only been ejected from the core recently since it was first detected midway through the sequence of observations. The limited data collected thus far for this component shows that it may also have a subluminal speed.

High resolution and reliable images produced from a combination of data from the SHEVE array and the VLBA have resulted in one of the first detections of a sub-pc-scale counterjet. The jet to counterjet brightness ratio in conjunction with estimates of speed in the jet indicate that the jet is inclined at a large angle to our line of sight, perhaps 70° to 80°, consistent with the kpc-scale structure of the radio source. Notably, it is difficult to reconcile the subluminal motion of component C2 with the observed jet to counterjet brightness ratio. This indicates that the motion of component C2 probably does not reflect the bulk motion of material in the jet. The episodes of rapid evolution may better reflect the true speed of material in the jet.

The spectral indices of the components seen with VLBI can be plausibly explained by the existence of a free-free absorbing structure which surrounds the central radio source and obscures the VLBI jet. The free-free absorption is in addition to synchrotron self-absorption for the compact core component and contributes to the $\alpha > 2.5$ spectral index observed between 4.8 and 8.4 GHz. Some information on the form of the obscuring structure can be derived only if values for the intrinsic spectral indices of C1 and C2 are assumed. The structure could plausibly be described as a torus with a cross sectional diameter of approximately 1 pc, similar to the free-free absorbing structures suggested for 3C

84 [Vermeulen, Readhead, & Backer 1994] and Cygnus A [Conway & Blanco 1995]. However, this interpretation may be somewhat complicated by single dish observations of a variable spectral index core [Botti & Abraham 1994].

Both the multi frequency and multi epoch VLBI observations of Centaurus A have provided a better understanding of the structure and evolution of a radio jet on the sub-pc-scale. A concerted program of further observations is now required to allow a more detailed study.

A key program to undertake will be the short time-scale monitoring of the sub-pc-scale structure of Centaurus A. The value of the combined SHEVE+VLBA imaging observations is clear since the counterjet is detected only when the combined $u - v$ coverage is available. Such observations should be continued at a rate of 3 or 4 per year to follow the subluminal component motions, not only in the jet but also possibly in the counterjet. Monitoring observations should also be made with a much shorter period to monitor the short time-scale changes in the bright part of the jet, namely C1.

Another key program will be to push the angular resolution of VLBI imaging observations of Centaurus A higher. At 8.4 GHz with the SHEVE+VLBA array, the VLBI core component is still only marginally resolved with a measured size of approximately 20 light days. Since the core spectral index is highly inverted, observations at a higher frequency would be well suited for increasing the resolution of imaging observations. Such observations have recently been undertaken with the VLBA. However, the largest gain in angular resolution will come from observations with the VSOP space VLBI observatory [Hirosawa 1991] in conjunction with ground based arrays such as the SHEVE array and the VLBA. At 22 GHz, the VSOP+ground array resolution will be approximately 50 μas, corresponding to approximately one light day at Centaurus A. Extensive Space VLBI observations of Centaurus A have been accepted for phase I of the VSOP mission. Centaurus A will be a key source in one of the VSOP Key Science Programs.

Chapter 6

GRO J1655-40 - A superluminal radio source in our Galaxy

6.1 Introduction

On 1994 July 27, the Burst and Transient Source Experiment (BATSE), on board the *Compton Gamma-Ray Observatory* (*CGRO*), detected an outburst of high energy X-rays from a previously unknown source toward the constellation of Scorpius [Harmon *et al.* 1995]. The source was designated GRO J1655-40.

Approximately 12 days after the X-ray outburst, a strong outburst at radio wavelengths occured [Campbell-Wilson & Hunstead 1994]. Given that Mirabel and Rodriguez [1994] had observed apparent superluminal motions following a similar outburst in another Galactic X-ray source, GRS 1915+105, with VLA observations, the radio outburst from GRO J1655-40 prompted radio astronomers to begin monitoring the source structure with synthesis arrays at arcsecond and mas resolutions.

Following observations of GRO J1655−40 with the SHEVE array, the aims of this chapter are:

1] To describe the SHEVE observations of GRO J1655−40, paying particular attention to the rapid structural evolution of the source and the problems for data reduction caused by this evolution.

2] To interpret the VLBI observations, to review other observations, and to review theoretical interpretations for GRO J1655−40.

The observations are described in § 6.2. The rapid evolution of the radio source and the problems in the data reduction caused by these effects are also described in § 6.2. The final results and interpretation of the SHEVE data are given in § 6.3. Finally in § 6.4, a brief review of observations of this object made at other wavelengths and several theories for the nature of the Galactic superluminal sources,

which have been presented since the discoveries of GRS 1915+105 and GRO J1655-40, are briefly reviewed.

6.2 Observations and data reductions

SHEVE observations of the radio source associated with GRO J1655-40 were obtained at short notice as a target of opportunity following the first detection of the radio source. Initially the real-time 275 km Parkes-Tidbinbilla interferometer (PTI) was used to determine that rapid changes were taking place in the source [Reynolds & Jauncey 1994]. Based on this information, the SHEVE array of telescopes, supplemented with several other telescopes, observed the source on the four days 1994 August 21, 22, 23, and 24 at a frequency of 2.3 GHz, for the purpose of imaging the source structure and following its evolution. The telescopes which participated were: Tidbinbilla (34 m, 70 m), Parkes, Hobart, Mopra, Narrabri, Hartebeesthoek, Goldstone (DSN, 70 m), and Mauna Kea (VLBA, 22 m). The data were all recorded in Mark II mode, obtained and processed as described in chapter 2.

The data tapes were quickly processed at the Caltech/JPL correlator, the data calibrated, and images produced. The entire experiment was turned around in less than two weeks.

During the correlation and fringe-fitting stages of data reduction it became apparent that the source was not detected on any inter continental baselines. The usable data were restricted to the baselines between the telescopes in Australia. On 1994 August 21 and 22, the source was detected at a useful signal to noise ($\geq$ 7σ) on all baselines except the longest baselines of the array, those from Mopra and Narrabri to Hobart. The Mopra-Hobart and Narrabri-Hobart baselines were removed due to this reason. Thus, several closure phase triangles were lost and all groups of 4 telescopes involving Hobart were lost. Therefore, during imaging, the Hobart data were used during the initial iterations of phase self-calibration but were not constrained when amplitude self-calibration was attempted, and were automatically removed from the dataset by the imaging software, DIFMAP. On 1994 August 23 and 24, no fringes on any baselines to Hobart were detected at a usable signal to noise.

Figures 6.1 (1994 August 21), 6.2 (1994 August 22), 6.3 (1994 August 23), and 6.4 (1994 August 24) show the images resulting from the data for each observation. The source consists of two components, each elongated along the position angle which joins them, 48°, and separated by approximately 0."5. The brightest component in the source is the south-west component, which is also the most compact component. The north-east component appears to have significant sub-structure at each of the four epochs. Over the first two days the north-east component contains three sub-components, but on the last two days only two remain. The middle component appears to have faded more quickly than its neighbours.

A comparison of the relative positions of the two components over the four day period indicates that they were separating at a rate of $\sim$ 60 mas/day, in general agreement with the results of the PTI observations. At the resolution of these observations the components were moving at a rate greater than one synthesised beam width per 12 hours, the time taken for a full synthesis observation.

Figure 6.1: Map peak, 0.4 Jy/beam. Contours, -1, 1, 2, 4, 8, 16, 32, and 64% of peak. Beam FWHM, 67.6×24.6 mas @ -84.9°.

Figure 6.2: Map peak, 0.3 Jy/beam. Contours, -1, 1, 2, 4, 8, 16, 32, 64% of peak. Beam FWHM, 80.9×26.8 mas @ -81.9°.
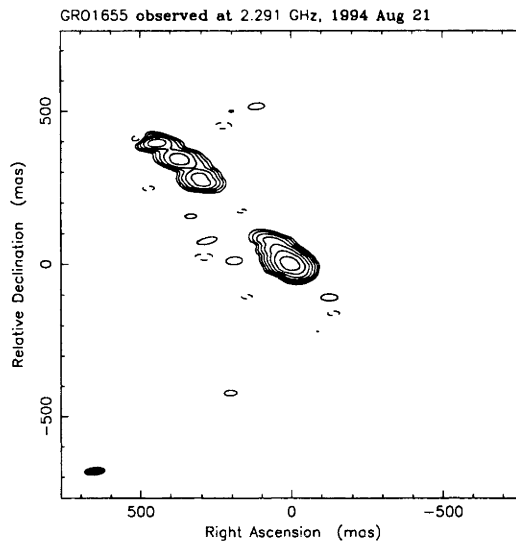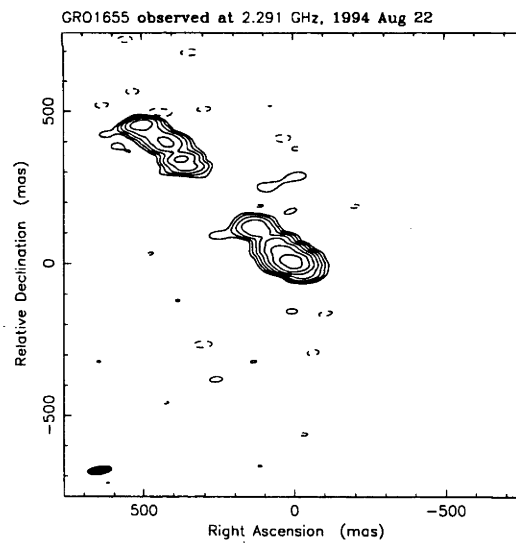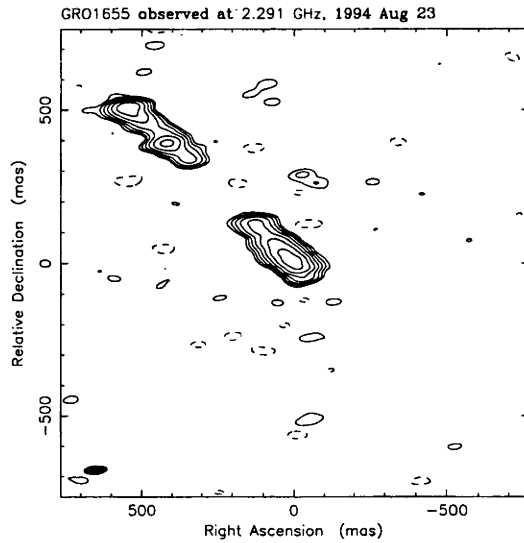
Figure 6.3: Map peak, 0.2 Jy/beam. Contours, -1, 1, 2, 4, 8, 16, 32, and 64% of peak. Beam FWHM, 74.8×27.1 mas @ -85.4°.
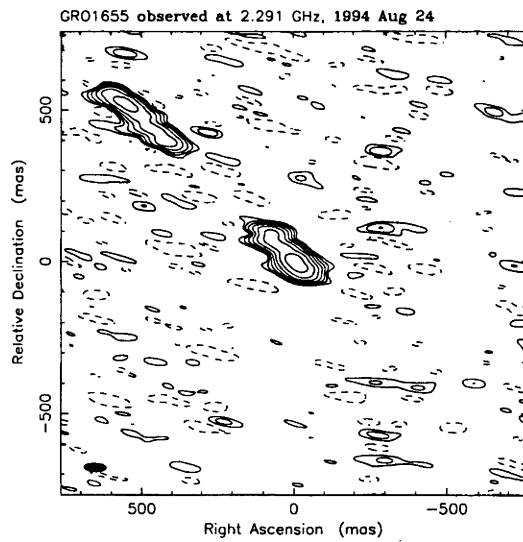

Figure 6.4: Map peak, 0.1 Jy/beam. Contours, -1, 1, 2, 4, 8, 16, 32, and 64% of peak. Beam FWHM, 71.4×27.9 mas @ 87.9°.

These observations create an unusual problem in that they violate a fundamental assumption of synthesis imaging, that the source structure remains constant over the period of the observation. The effect of a 60 mas/day motion of a source observed with the SHEVE array at 2.3 GHz is illustrated in Figure 6.5. The data shown in Figure 6.5 were simulated with the program FAKEM, a modified version of the Caltech VLBI program FAKE (A.K. Tzioumis 1994, private communication) which is used to generate the data expected at a given time, for a given source model, and a given array of telescopes. FAKEM accepts source models with two extra parameters. For each model component one can define an angular motion for the component in mas/day, relative to the phase tracking centre, d, and a position angle for the component motion, θ.

Figure 6.5 shows simulated data for a source with a model, similar in structure to GRO J1655−40, as given in Table 6.1, over a period of approximately 12 hours, on 1994 August 21, with the Tidbinbilla, Parkes, Mopra, and Narrabri antennae. The celestial coordinates for the source model are those of GRO J1655−40. The solid line shown in Figure 6.5 corresponds to the source model as it was at the beginning of the observation. The comparison between stationary model and data from the evolving model shows that a large change in the source structure is apparent between the start of the observation and the end of the observation.
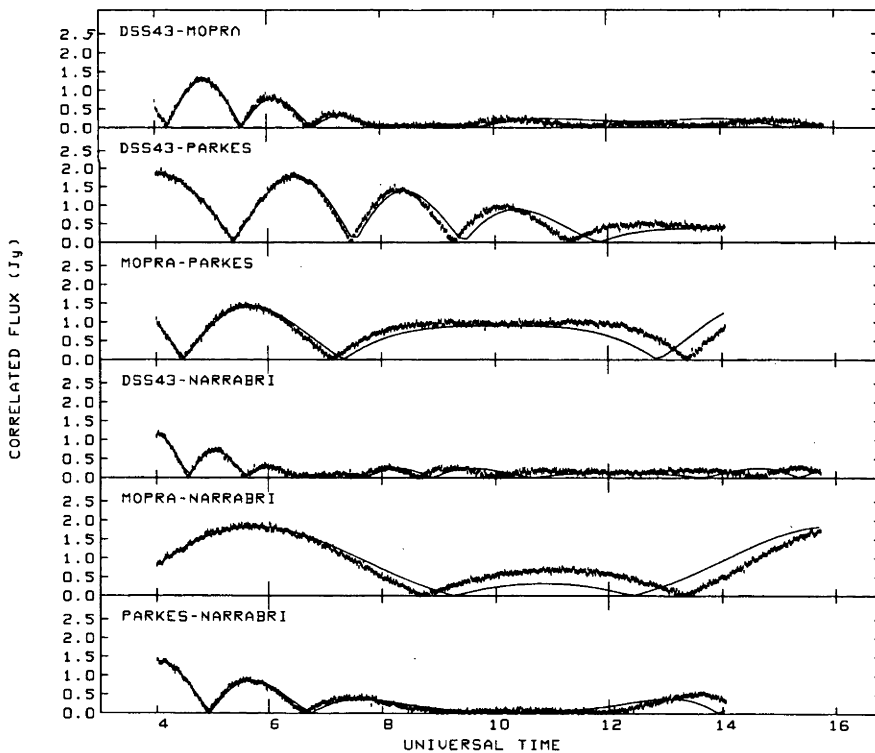
Figure 6.5: Stationary model and data from evolving model

S (Jy)	d (mas)	$\theta°$	A (mas)	B/A	$\phi°$	Type	d	θ_{motion}
0.6	0	0	200	0.3	48	1	0	0
0.4	400	48	200	0.3	48	1	60	48

Table 6.1: Dynamic model to illustrate motion in GRO J1655−40

Imaging simulations on data produced from FAKEM by A.K. Tzioumis (described in Tingay *et al.* 1995) revealed that data from sources which change their structure of the order of a beam width during the period of the observation produce significant distortions in the resultant images. Therefore, some strategy was required to ensure that reliable images could be produced from the real GRO J1655−40 data.

As yet, no general imaging or model-fitting algorithm exists to handle data for sources with rapidly varying structures. Therefore, guided by the simulation shown in Figure 6.5 and the data for GRO J1655−40, it was decided that the validity of the features in Figures 6.1 - 6.4 could be confirmed by considering only a subset of the original data. An inspection of Figure 6.5 shows that over the first 5 hours of observation the data and stationary model are a reasonable match. Only after this period do they become seriously discrepant. The first 5 hours of the observation also include the visibilities which contain the majority of the information constraining the source, as seen in the real data shown in Figure 6.10 from 1994 August 21.
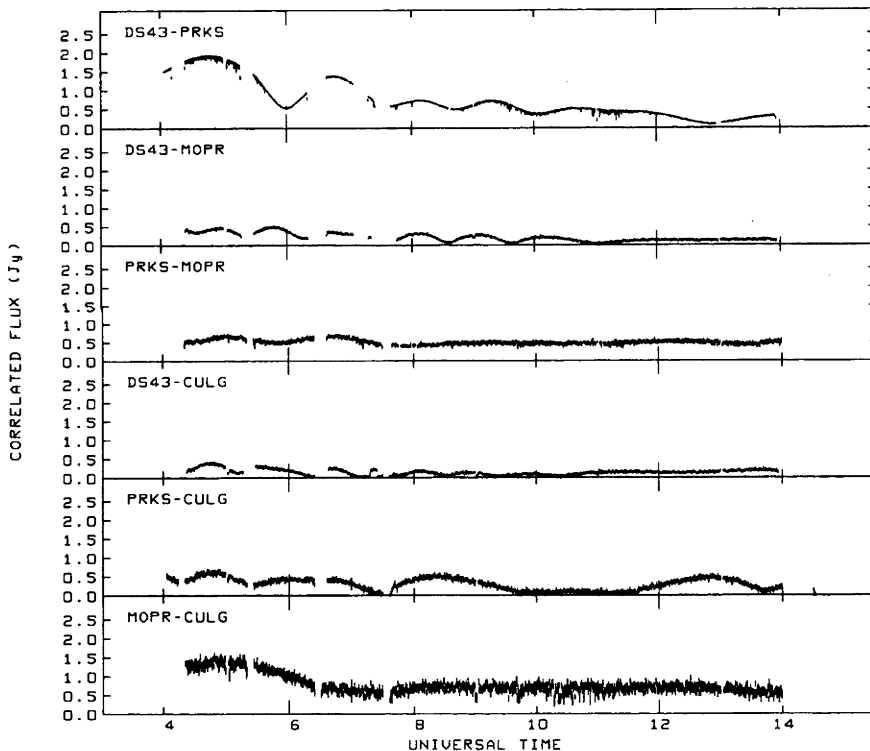
Figure 6.6: SHEVE GRO J1655−40 data, 1994 Aug. 21

From the 4 original data sets, 4 new data sets were produced which contained only the first 5 hours of data from each observation. From these data, the images in Figures 6.7, 6.8, 6.9, and 6.10 were produced. These new images confirm the overall structure of the source and in particular the sub-structure of the north-east and south-west components. Now, with 5 hours data, the source components separate only 13 mas over the observation period, approximately half of the small dimension of the restoring beam. The dynamic range and resolution of the images has been reduced however.
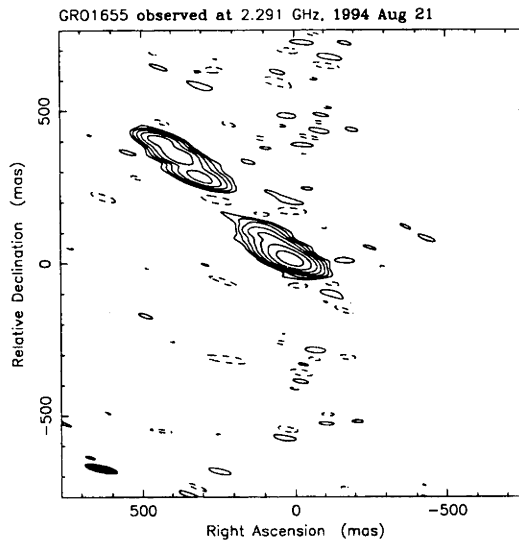
Figure 6.7: Map peak, 0.5 Jy/beam. Contours, -1, 1, 2, 4, 8, 16, 32, and 64% of peak. Beam FWHM, 106.0×23.4 mas @ 76.4°
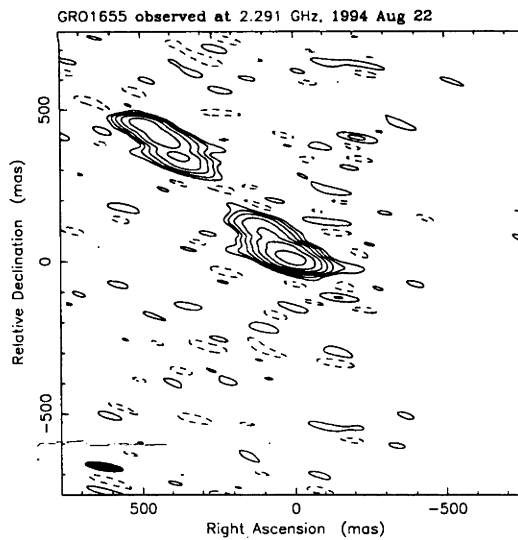
Figure 6.8: Map peak, 0.4 Jy/beam. Contours, -1, 1, 2, 4, 8, 16, 32, and 64% of peak. Beam FWHM, 123.0×25.7 mas @ 80.1°.
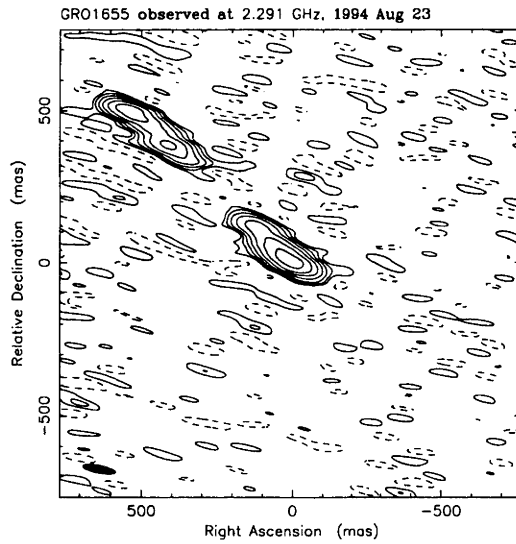
Figure 6.9: Map peak, 0.2 Jy/beam. Contours, -1, 1, 2, 4, 8, 16, 32, and 64% of peak. Beam FWHM, 106.0×25.6 mas @ 78.4°
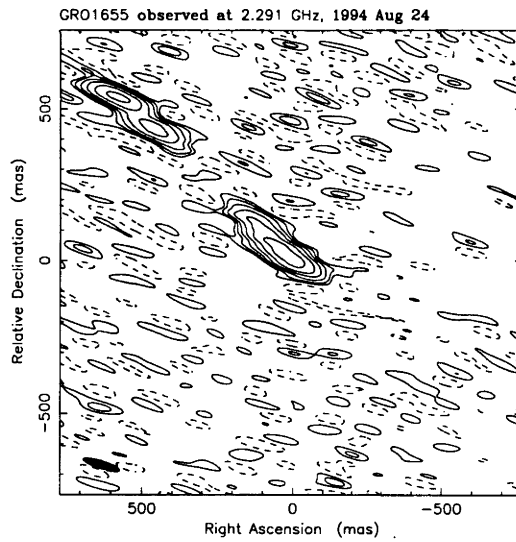
Figure 6.10: Map peak, 0.2 Jy/beam. Contours, -2, 2, 4, 8, 16, 32, and 64% of peak. Beam FWHM, 123.0×25.9 mas @ 72.2°

Finally, the four images resulting from the restricted data sets have been rotated by 42°, shifted vertically, aligned on the brightest component at the south-west end of the source, and plotted in Figure 6.11 on a common flux density scale. The peak flux density in the montage is 0.6 Jy/beam and the flux density contours are 1, 2, 4, 8, 16, 24, 32, 64, 80, and 95% of the peak. The restoring beam for the montage is 123×23 mas at a position angle of 72°. The measurement of the positions of the sub-components in the north-east component, relative to the south-west component, gives a value for the angular speed of expansion of the source of 65±5 mas/day.

If this expansion is extrapolated back in time to the point at which the two components were coincident, the zero separation date is 1994 August $13.5 \pm^{0.5}_{0.8}$. This date is approximately one day after the rapid rise in radio flux density [Campbell-Wilson & Hunstead 1994] and close to the end of the decline in X-ray luminosity [Wilson et al. 1994].
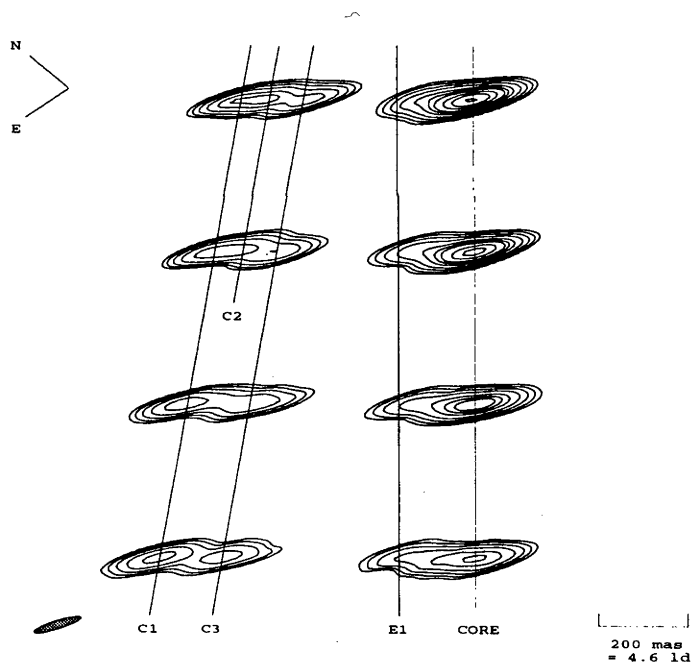
Figure 6.11: Final SHEVE images of GRO J1655-40

6.3   Interpretation

The distance to GRO J1655−40 is between 3 and 5 kpc, as determined from observations of Galactic HI toward the continuum source [Tingay *et al.* 1995]. The observed angular expansion of 65±5 mas/day then corresponds to an apparent speed, relative to the speed of light, of $\beta_{app} = 1.5 \pm 0.4$. The expansion of the source is apparently superluminal.

However, what is the intrinsic speed of separation after accounting for the relativistic effects which are responsible for the appearance of apparent superluminal motion? Before answering that question some assumptions must be made about the nature of the two components seen in the images. One possibility is that one of the components is the core of the source, coincident with the source of high energy X-rays and stationary. The other component may be moving away from the core after being ejected on approximately 1994 August 13 - 14. Thus the observed expansion of the source would be due to a one-sided motion.

The second possibility is that neither of the components are the core of the source and both are in motion away from an unseen core which ejected the components simultaneously on approximately 1994 August 13 - 14. Thus the observed expansion of the source would be due to two-sided motion.

These two possibilities cannot be distinguished on the basis of an absolute registration of the four images. Absolute positions cannot be recovered from the SHEVE data for the purposes of aligning the images in celestial coordinates and no information on the component spectra are available to allow the identification of the core. Both possibilities are also consistent with an ejection event near 1994 August 13 - 14. One argument in favour of one-sided expansion is that the brightest component in each image (the south-west component) is also the most compact, reminiscent of the compact core of an extragalactic radio source.

The two possibilities cannot be distinguished on the basis of the available data. Both possibilities must, therefore, be considered. First, a one-sided expansion with the south-west component as a stationary core yields a minimum intrinsic speed for the north-east component relative to the core of between 0.7 and 0.9 times the speed of light (e.g. Pearson and Zensus 1987), for the limits on the distance to GRO J1655−40.

Second, for a two sided expansion and assuming equal component speeds and opposite directions of motion, the intrinsic component speeds are between 0.5 and 0.8 times the speed of light [Tingay *et al.* 1995]. If either of the possible source geometries are adopted then the intrinsic speed of ejecta forming the radio source is at least mildly relativistic.

Hjellming and Rupen [1995] have published extensive VLBA observations of GRO J1655−40 over a period of weeks, rather than days, from which they plausibly identify the core of the radio source as the south-west component which appears in the images here. They derive an intrinsic speed of approximately 0.92 times the speed of light and an angle to the line of sight of approximately 85°. The observations presented here from 1994 August 21, 22, 23, and 24 are coincident in time with the second VLBA observation of Hjellming and Rupen [1995] and the images resulting from the SHEVE and VLBA observations agree very well.

Marked on the montage in Figure 6.5 is the position of the south-west component which has been aligned vertically. Also marked are the positions of the

sub-components of the north-east component, C1, C2 and C3 and an extension to the south-west component E1. A curious aspect of the evolution in GRO J1655−40 over these four days is the rapid disappearance of the component designated C2, the middle sub-component in the north-east component. C2 is the brightest feature in the north-east component on 1994 August 21 but weakens quickly and is absent from the image on 1994 August 24 whereas the leading sub-component C1 and the trailing sub-component C3 do not fade as quickly. Also interesting is the extension to the south-west component E1, which appears to be an extension of constant length and strength from the core.

In the absence of longer term daily monitoring it is difficult to explain the rapid evolution in GRO J1655−40. Perhaps the sub-component C1 remains bright since it is the head of the jet which is advancing through the interstellar medium, similar to the head of an FR II radio source. The constant extension from the core may be the base of the relativistic jet. However, these speculations do not explain why C2 should be a highly variable feature whereas C1, C2, and E1 are not.

6.4   Discussion

GRO J1655−40 was the second apparently superluminal radio source to be discovered in our Galaxy, after GRS 1915+105 [Mirabel & Rodriguez 1994], but the first to have very high resolution images reveal the detailed morphology of the source. The high and low resolution radio imaging [Tingay *et al.* 1995; Hjellming and Rupen 1995], the X-ray monitoring [Harmon *et al.* 1995], and optical observations [Bailyn *et al.* 1995a; Bailyn *et al.* 1995b] make GRO J1655−40 one of the best studied X-ray transients yet. The data, when taken together, make a strong empirical case for a direct connection between the accretion of material onto a compact, stellar mass object (possibly a black hole) and the production of relativistic jets. The relationship between evolution in the compact radio source and emissions at other wavelengths has been well demonstrated for this object.

The radio source associated with GRO J1655−40 has been shown to be produced at the time of the initial strong outburst in radio emission, following the first outburst in X-rays. Harmon *et al.* [1995] show a similar correspondence between X-ray outburst and relativistic jet production for two later outbursts from GRO J1655−40, in 1994 September and 1994 November. On each of these occasions a strong X-ray outburst was followed closely by a radio outburst and the ejection of a new component of radio emission from the core. However, interestingly, while the X-ray outbursts continued at the same strength, each subsequent radio outburst was approximately an order of magnitude weaker than its predecessor [Harmon *et al.* 1995]. GRO J1655−40 thus made the transition from an accreting radio loud source to an accreting radio quiet source.

Bailyn *et al.* [1995a; 1995b] reported optical observations of GRO J1655−40 during its quiescent state. They found variations in the total output at optical wavelengths typical of an eclipsing binary system. From the eclipses and optical spectroscopy they calculate the orbital period to be approximately 2.6 days. They also determined the mass function of the system to be 3.35 ± 0.14 $M_\odot$ and suggested that the primary mass of the system is in a black hole with mass $\sim5.3M_\odot$.

These conclusions make objects like GRO J1655−40 very interesting. All of

the activity associated with an accretion driven relativistic jet can be observed on very small spatial scales and over a short period in time. Since these systems may represent scaled-down versions of galaxy-scale galactic nuclei and radio jets, they may yield important clues to the process of accretion and jet production in galaxies and quasars. Since the discovery of GRS 1915+105 and GRO J1655−40 several investigators have made an attempt to understand the Galactic superluminals and their connection with AGN.

Levinson and Blandford [1996] investigated the physical conditions within the Galactic superluminal sources, their possible formation and the interactions with their environments. They contrast the properties of e - p and e^+ - e jets. From their calculations they derive for GRO J1655−40 an equipartition minimum pressure of $P_{min} \sim 5 \times 10^{-6}$ dyn cm^{-2}, magnetic field of $B \sim 10^{-2}$ G, a jet luminosity of $L_{jet} \sim 6 \times 10^{37}$ ergs s^{-1}, and an annihilation radius for electron positron pairs of greater than 7×10^8 cm, for an e^+ - e jet. The jet luminosity for an e - p jet is higher, $L_{jet} \sim 3 \times 10^{38}$ ergs s^{-1}.

Levinson and Blandford [1996] also predict the wavelength of blue and red shifted H_α lines which would support the case for an e - p jet, 1.4 and 1.8 μm respectively. No reports of red and blue shifted H_α lines have thus far been reported for GRO J1655−40 or GRS 1915+105.

Meier [1996] concentrates on a model of jet production for the Galactic superluminal sources and an explanation of the observed delay between X-ray outburst, signifying accretion, and the production of a relativistic jet. Meier [1996] suggests that the delay between the onset of accretion and jet production occurs when the accretion rate exceeds approximately one third of the Eddington limit, citing the Papaloizou-Pringle compressible shear instability as the agent which disrupts the jet producing region of the source during this high accretion phase. Once the accretion slows and stabilises the relativistic jet forms via the Blandford-Payne MHD acceleration process seeded by an e^+ - e wind. Meier [1996] gives a detailed application of this model to GRO J1655−40 in particular and to other objects such as GRS 1915+105, 1E 1740.7-2942, and Cygnus X-1.

Falke and Beirmann [1996] describe their hypothesis that jets and disks around compact accreting objects are symbiotic features and apply it to the new class of Galactic superluminal sources. They do this by comparing their predictions of disk to radio core luminosities to the observed values. From their model they find that the disk/jet symbiosis can explain the Galactic superluminals and other Galactic jet sources in a radio loud - radio quiet paradigm similar to what they find for radio loud and radio quiet AGN. Thus, they find that their model predictions are reasonable over approximately 15 orders of magnitude in radio power and 10 orders of magnitude in disk luminosity.

Observations of the Galactic superluminals have sparked a significant theoretical effort in attempting to explain their nature and possible relationship to the more powerful extragalactic jet sources. At present it appears that it is plausible that an underlying process controls jet production over a wide range in jet power and spatial scale, and that the process is strongly related to accretion. Strong results and observational predictions regarding the details of the production mechanism are still elusive however.

Chapter 7

The unusual radio galaxy, PKS 1718−649

7.1 Introduction

The radio source PKS 1718−649 lies at a distance of approximately 56 Mpc (z=0.014, adopting H_o=75 km/s/Mpc). It was optically identified as the galaxy NGC 6328 by Savage [1976] and has been extensively studied at optical wavelengths by Fosbury *et al.* [1977], Carswell *et al.* [1984], Filippenko [1985], and Keel and Windhorst [1991] since it is a nearby galaxy and a source of strong optical emission lines. The active nucleus at the centre of the galaxy is generally classified as a Low Ionisation Nuclear Emission Region (LINER). The optical morphology of the galaxy is unusual in that it appears to have a central brightness profile which follows an $r^{1/4}$ de Vaucoluers law typical for elliptical galaxies but has spiral arms which extend out approximately 20 kpc from the nucleus [Véron-Cetty *et al.* 1995].

The properties of the radio source, until recently, were not as well determined as the optical properties of the galaxy. The monochromatic luminosity of the radio source at 1.4 GHz is approximately 1.2×10^{24} W/Hz if a distance of 56 Mpc is assumed. Fosbury *et al.* [1977] observed the galaxy at the HI transition and inferred that a large fraction, 6%, of the galaxy mass consisted of neutral Hydrogen. Véron-Cetty *et al.* [1995] showed that the neutral Hydrogen exists in an incomplete ring, 37 kpc in diameter, and an envelope which extends over 180 kpc. Fosbury *et al.* [1977] also presented the radio spectrum between 408 MHz and 5 GHz, showing it to be inverted, indicating the presence of compact radio emission. The first VLBI observations of the compact radio source in PKS 1718−649 were undertaken as part of the first SHEVE experiment in 1982. The resulting data were sparse but could be modelled in terms of two components, separated by approximately 15 mas along a position angle of approximately −65° [Preston *et al.* 1989].

The combination of strong and active compact radio source and spiral galaxy is an unusual one. Fosbury *et al.* [1977] point out that PKS 1718−649 is among the few strong, flat or complex radio spectrum sources to be associated with a galaxy, although more extreme examples exist, such as PKS 1934−638. PKS 1718−649 is, therefore, an interesting target for a more comprehensive investigation of the radio source. In particular, the proximity of this object provides the opportunity for high spatial resolution imaging of the compact radio structure since 1 mas is approximately equal to 0.25 pc at the red shift of z=0.014 (H_o=75 km/s/Mpc).

Furthermore, the proximity of the galaxy allows relatively high resolution studies
of the emission from the host galaxy at other wavelengths.

The aims of this chapter are to:

**1] Present the first extensive investigation of the PKS 1718−649 radio
source and to review previous observations at other wavelengths.**

**2] Arrive at an interpretation for this unusual object from a
consideration of the available data.**

In this chapter the first VLBI imaging observations of the compact radio emis-
sion from PKS 1718−649 are presented in § 7.2. In § 7.3, the results from polari-
metric radio imaging at the ATCA are described. Also in § 7.3, total flux density
measurements which extend the PKS 1718−649 radio spectrum up to 230 GHz are
presented. Finally a discussion of the nature of the radio source and its host galaxy
is given in § 7.5, paying particular attention to two possible interpretations.

7.2   VLBI observations

The SHEVE data were obtained and processed as described in chapter 2. Table
7.1 gives a journal of the observation dates and the participating telescopes.

Figure 7.1 shows the image resulting from observations at 2.3 GHz. The source
appears unresolved with the 21.5×11.7 mas restoring beam. The total flux in the
image is 4.7 Jy and a dynamic range of approximately 100:1 was realised.

Figure 7.2 shows the image from observations at 4.8 GHz. With the 2.6×2.3
mas beam the source is resolved into a double with separation 6.8 mas and position
angle 135 degrees. The total flux density in the image is 4.3 Jy and a dynamic
range of approximately 100:1 was realised. The sizes, PA's and flux densities of the
two components (de-convolved from the beam) are given in Table 7.2, along with
the corresponding estimates of brightness temperature, radio luminosity and total
internal energy (calculated from equipartition considerations).

Figure 7.3 shows the results of observations at 8.4 GHz. The total flux density
in the image is 3.4 Jy and the dynamic range approximately 100:1. The clean
components resulting from both the 4.8 and 8.4 GHz data were convolved with a
6.4 mas FWHM circular Gaussian beam (corresponding to the major axis of the
formal 8.4 GHz beam) and the spectral indices of the two components estimated
(Table 7.2).

Epoch	Frequency	Telescopes
	(GHz)	
1994 Feb. 23	2.3	Pk,Hb,Na,Mr,Ht
1993 May 14	4.8	Pk,Hb,Na,Mr,Pr27,Ht
1993 July 4	8.4	Ds45,Pk,Hb,Na,Mr

Table 7.1: Observation log for PKS 1718−649
Ds45 = Tidbinbilla (34 m), Pk = Parkes, Hb = Hobart, Na = Narrabri,
Mr = Mopra, Pr27 = Perth (27 m), Ht = Hartebeesthoek

1718−649 observed at 2.291 GHz, 1994 Feb 23
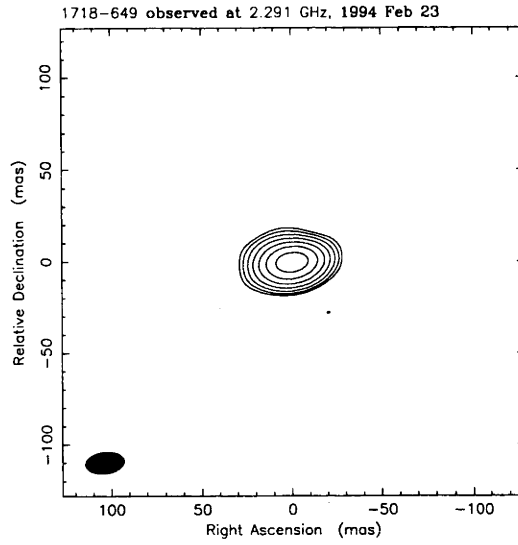
Figure 7.1: Map peak, 3.7 Jy/beam. Contours, 1, 2, 4, 8, 16, 32, 64% of peak. Beam FWHM, 21.5×11.7 mas @ -83.0°.
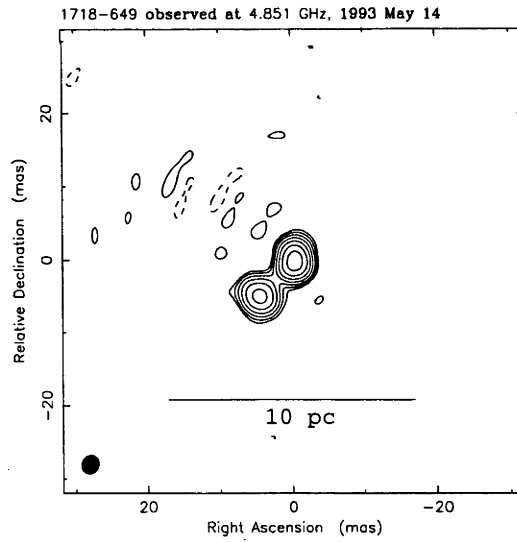
1718−649 observed at 4.851 GHz, 1993 May 14

10 pc

Figure 7.2: Map peak, 2.0 Jy/beam. Contours, -1, 1, 2, 4, 8, 16, 32, 64% of peak. Beam FWHM, 2.6×2.3 mas @ -29.5°.
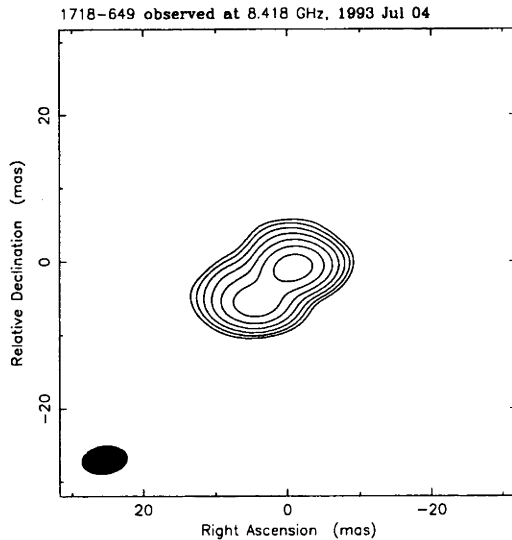
1718−649 observed at 8.418 GHz, 1993 Jul 04

Figure 7.3: Map peak, 1.8 Jy/beam. Contours, 1, 2, 4, 8, 16, 32, 64%. Beam FWHM, 6.4×3.8 mas @ -83.2°.

The small temporal difference between each of these epochs and the mismatch in frequency and resolution means that no estimate of the motion of components on the pc-scale can be made. The model derived by Preston *et al.* [1989] for the VLBI structure of PKS 1718−649 in 1982 has the two components at a significantly different position angle and at a much larger separation than the images in Figures 7.1, 7.2, and 7.3 indicate. These differences can be readily explained by the sparseness of the data available in the earlier experiment. Evolution in the source need not be invoked.

In addition to the data from 1982, observations of PKS 1718−649 were made with the SHEVE array at two other epochs, 1988 July 24 at 2.3 GHz and 1989 December 10, also at 2.3 GHz. These data have not been published. The 1988 and 1989 data were model-fit using the technique described in § 3.1 of chapter 5. Unfortunately, like the 1982 data, the 1988 and 1989 data were too sparse to sensibly constrain a model, although there is obvious structure on the long baselines at 2.3 GHz. No useful comparison could be made between the new set of images and the model-fitted data from 1982, 1988, or 1989.

Further imaging observations will be required before a useful estimate of the pc-scale evolution in PKS 1718−649 can be made.

As can be seen from Table 7.2 the north-west component is the brighter and more compact of the two components, although both components are comparable in size and marginally resolved by the beam. The north-west component has a steep spectrum and the south-east component has a flat spectrum. The components appear very similar at 4.8 GHz and neither strongly resemble the pc-scale jets seen in many other compact radio sources. The two components are also significantly misaligned in position angle, differing by approximately 49°, and neither are aligned along the position angle joining the two components.

The images in Figures 7.1, 7.2, and 7.3 were made without the data on baselines from the Australian antennae to Hartebeesthoek in South Africa. The two

components are prominent on these long baselines at 4.8 and 8.4 GHz, indicating that there exists emission from both components from regions more compact than about 0.3 mas (0.08 pc).

@ 4.8 GHz	NW comp.	SE comp.
Size (mas)	2.3×1.2	2.4×1.5
Major axis PA°	6	55
Flux density (Jy)	3.0	1.3
Brightness Temp. (K)	5×10^{10}	2×10^{10}
Luminosity (W/Hz)	1.0×10^{24}	4.7×10^{23}
E(total) (ergs)	5.6×10^{36}	1.3×10^{32}
$\alpha_{8.4}^{4.8}$ ($S_\nu \propto \nu^\alpha$)	-0.8	-0.3

Table 7.2: Radio properties of PKS 1718−649 at 4.8 GHz.

7.3   Low-resolution radio continuum observations

Continuum imaging at 2.37 GHz was carried out at the ATCA on 1993 September 5. The east-west array and maximum baseline of 6 km gave a nearly circular beam of approximately 3.8 arcseconds. A bandwidth of 128 MHz, 32×4 MHz, was used, the middle 50 percent retained for imaging. The data were initially edited in AIPS. A full polarimetric calibration was then made in multi-frequency synthesis mode with the MIRIAD imaging software. The ATCA primary calibrator, PKS 1934−638, was used throughout the observation. PKS 1718−649 itself is listed as a secondary calibrator for the ATCA. It appears that PKS 1718−649 is an excellent calibrator since it appears point-like and has a low fractional polarisation (Figure 7.4). No extended structure was observed at a dynamic range of 1000:1, or 4.6 mJy/beam. The total flux density in the image was 4.6 Jy and the fractional polarisation of the E vector approximately 0.35%. The polarisation position angle is -6°.

Figure 7.5 shows the radio spectrum of PKS 1718-649 between 408 MHz and 230 GHz (filled triangles). The data at 1.4, 2.3, 4.8 and 8.4 GHz are from co-eval observations with the ATCA in 1994 (L. Kedziora-Chudzer *et al.* 1995, private communication). The 408 MHz measurement comes from previously published work [Tzioumis 1987]. The 843 MHz datum was obtained with the Molonglo Observatory Synthesis Telescope (MOST) in 1994 (B. Gaensler *et al.* 1995, private communication) and the 22 GHz measurement from the 70 m Deep Space Network telescope at Tidbinbilla in 1996.

For the 22 GHz observations, an automated control program measured the on and off source system temperatures and calculated the ratio of source temperature to noise diode temperature for two sources, PKS 1718−649 (the target) and PKS 1934−638 (a calibrator). Both sources were observed in good weather and near the meridian. The 22 GHz flux density of PKS 1718−649 was arrived at by extrapolating the PKS 1934−638 spectrum [Tzioumis *et al.* 1989] to 22 GHz and using that value to calibrate the source to diode ratio. Correction was made for the small difference in elevation through a gain-elevation curve for the 70 m tele-
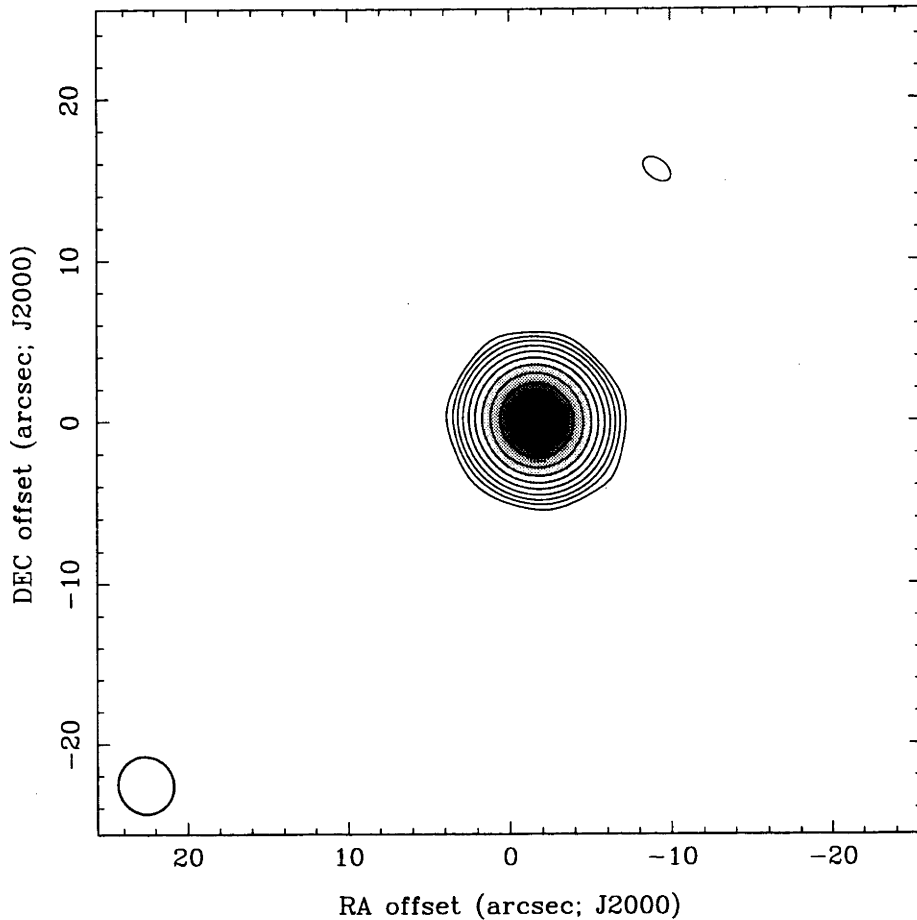
Figure 7.4: ATCA image of PKS 1718−649 from 1993 Sep 5. Map intensity peak, 4.60 Jy/beam. Contours, -0.1, 0.1, 0.25, 0.5, 1, 2, 4, 8, 16, 32, 50, 70, 95% of peak. Beam FWHM, 3."8. Map polarisation peak, 0.017 Jy/beam. Polarisation scale, 0.0022 Jy/beam/mm. The map centre is RA = 17 23 41.270, DEC = -65 00 36.80; J2000.

scope at 22 GHz (K. Fujisawa 1996, private communication). No beam dilution corrections were required since both sources are point-like.

The 90 and 230 GHz flux density measurements of PKS 1718−649, shown in Figure 7.5, were made at the Swedish ESO Sub-millimetre Telescope (SEST) in Chille (M. Tornikowski 1996, private communication) on 1996 February 26.

In addition to the total flux densities in Figure 7.5, the flux densities of the VLBI source at 2.3, 4.8, and 8.4 GHz are also plotted, with 10% errorbars (see chapter 2). At each of these frequencies the VLBI flux density can account for the entire flux density of the source. This supports the ATCA result that the radio source has no extended structure on the scale of arcseconds. For comparison, the radio spectrum of PKS 1934−638 is shown in Figure 7.5 (filled squares).

Only limited data is available on the variability of the total flux density of PKS 1718−649. No significant flux density variability is apparent at 843 MHz (D.
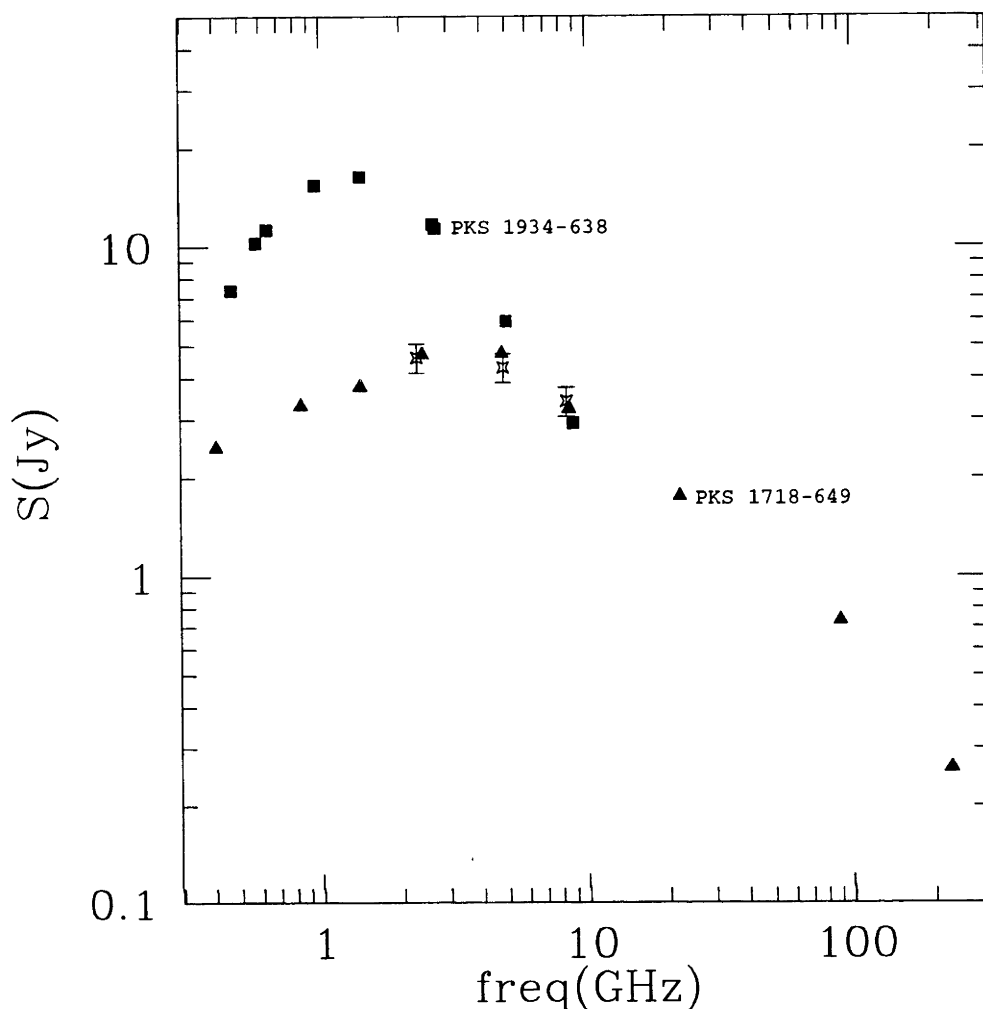
Figure 7.5: Radio spectrum of PKS 1718−649 (filled triangles) compared to the radio spectrum of PKS 1934−638 (filled boxes). Stars with errorbars are the VLBI fluxes for PKS 1718−649.

Campbell-Wilson 1996, private communication).

7.4   The nature of PKS 1718−649

7.4.1   A core-jet radio source?

The first possibility to consider for the interpretation of the data which are now available, is that PKS 1718−649 is a compact, flat-spectrum, core-jet radio source; the source consists of a relativistic jet of material which originates at a compact core and radiates at radio wavelengths .

   The radio source is certainly very compact, as can be seen from Figures 7.1, 7.4, and 7.5. The flux density at 2.3, 4.8, and 8.4 GHz in the VLBI images presented in Figures 7.1, 7.2, and 7.3 can account for the total flux density seen with much lower resolution observations. The core dominance parameter, R (the ratio of compact to extended flux density) cannot be estimated since no radio structure on scales

larger than approximately 20 mas (5 pc) has been detected. Under the core-jet interpretation this fact would make PKS 1718−649 a core dominated radio source, like a BL Lac type object or core dominated quasar.

The pc-scale structure itself consists of two components, one of which has a steep spectrum between 4.8 and 8.4 GHz ($\alpha = -0.8$), the other having a flat spectrum over the same range ($\alpha = -0.3$). The usual interpretation of this result would be that the flat-spectrum component is the active core of the radio source, coincident with the central engine and that the steep-spectrum component would be part of a jet which originates at the core. However, apart from the spectral indices, these two components do not resemble a typical core-jet structure. The two components have almost equal size and are both resolved with a 2.6×2.3 mas beam. The two components are discrete and have major axis position angles which are misaligned with each other and the position angle joining them. This contrasts with core-jet sources in that jet components are usually much more resolved than core components; jets are elongated and are usually linear and aligned.

Many core dominated radio sources show evidence for a significant emission component of beamed synchrotron radiation at radio and other wavelengths. One line of evidence is rapid variability in flux density. From the limited radio variability data available for PKS 1718−649, there is no evidence for significant variability at low frequencies.

Another line of evidence for beamed emission is the presence of a high brightness temperature radio core (see § 4.2). The candidate core of PKS 1718−649, the south-east component, has a brightness temperature of only 2×10^{10} K, two orders of magnitude below the nominal limit for synchrotron emission. Thus, beaming is not required to explain the pc-scale radio emission.

For PKS 1718−649, the non thermal emission component at optical wavelengths is very small, only approximately 6% of the continuum at $\lambda 5460$ [Filippenko 1985]. This can be compared to approximately 91% for the lobe dominated radio source PKS 0518−458 (Pictor A) [Filippenko 1985]. For a core dominated source like PKS 1514−241 (AP Libræ), the non thermal emission completely dominates at optical wavelengths [Visvanathan & Griersmith 1977].

The radio spectrum of PKS 1718−649 is inverted between 408 MHz and 4.8 GHz, typical for a core dominated radio source. Between 4.8 and 22 GHz the spectrum steepens so that the spectral index corresponds to optically thin synchrotron emission, $\alpha = -0.65$. Typically, for a core dominated radio source the spectrum will remain inverted or flat in this region, due to a strong flat-spectrum core component.

The environment of PKS 1718−649 is also unusual. It is rare to find a strong flat or complex radio spectrum source associated with a galaxy, especially a galaxy that appears to have a spiral structure. Fosbury *et al.* [1977] cites PKS 1934−649 as a more extreme example of complex radio spectrum source in a galaxy, but the host of PKS 1934−638 is an elliptical and the radio source itself is not a typical core-jet radio source, but a GHz Peaked-Spectrum (GPS) radio source. The powerful optical emission lines of PKS 1718−649 are also reminiscent of PKS 1934−638 [Fosbury *et al.* 1977].

PKS 1718−649 has some of the features expected of the core-jet paradigm, compact structure and a candidate flat-spectrum core. However, the morphology of the radio source and the galaxy, and the optical and radio spectra do not strongly

support the interpretation of PKS 1718−649 as a core dominated core-jet radio source.

7.4.2 A GHz Peaked-Spectrum type object?

The second possibility to consider for the interpretation of PKS 1718−649 is that it belongs to the class of extragalactic radio sources known as GHz Peaked-Spectrum (GPS) radio sources. These are a little understood class but distinct from flat-spectrum, core-jet radio sources in their properties. O'Dea, Baum, and Stanghellini [1991] reviewed the properties of GPS sources and list their defining characteristics: radio spectra peaked near 1 GHz, low radio polarisations, large radio luminosities, and mostly compact radio structure.

PKS 1718−649 meets the criteria set out for candidature of a sample of Northern Hemisphere GPS radio sources [Stanghellini et al. 1990]: $S_{5.0GHz} > 1$ Jy, 0.4 GHz $< \nu_{turnover} < 5.0$ GHz, $\alpha < -0.5$ ($S_\nu \propto \nu^\alpha$, $\nu > \nu_{turnover}$), and $|b| > 10°$. However, the radio spectrum of PKS 1718−649 is only an average example of a GPS spectrum. The archetypical GPS sources PKS 1934−638 and 0108+388 have very well defined spectral turnovers and narrow peaks. The PKS 1718−649 radio spectrum is broader but similar to some of the candidate GPS sources listed by O'Dea, Baum, and Stanghellini [1991].

O'Dea, Baum, and Stanghellini [1991] verify that low radio polarisation is a key characteristic of GPS sources. For 38 sources with measurements, the median fractional polarisation at 21 cm is approximately 0.2%. The value of 0.35% at 13 cm for PKS 1718−649 is consistent with this result.

PKS 1718−649 is a strong radio source but cannot rival the luminosities of any of the known GPS sources. PKS 1718−649 would be the lowest luminosity GPS source known. However, it would be by far the lowest red shift GPS source known also. Most known GPS sources lie at red shifts greater than 0.2 and only two are known at red shifts less than 0.1 (1404+286, O'Dea, Baum, and Stanghellini 1991; 1144+352, Snellen et al. 1995). However, the selection criteria for candidature of the GPS class introduces a severe bias favouring luminous, and therefore, high red shift sources. There is no reason to conclude that all GPS sources have very large luminosities. Weaker GPS sources may be prevalent but missed due to observational limitations.

As stated, PKS 1718−649 is a highly compact radio source, fulfilling the third criteria of O'Dea, Baum, and Stanghellini [1991]. Furthermore, the pc-scale morphology of PKS 1718−649 is typical for GPS sources which are found to be associated with galaxies. Phillips and Mutel [1980] first noted that GPS radio sources in galaxies (as opposed to quasars) consist of two pc-scale components of similar flux density and spectral shape. A prominent example of this type of GPS galaxy is PKS 1934−638 [Tzioumis et al. 1989]. The description of GPS galaxy applies very well to the pc-scale morphology of PKS 1718−649. However, the limited spectral information on the two components between 4.8 and 8.4 GHz shows that they probably do not have the same spectral shape.

Five possible physical interpretations for the characteristics of the GPS sources are currently favoured [O'Dea, Baum, and Stanghellini 1991; Stanghellini et al. 1993]. These interpretations are centred around the suggestion that the radio plasma is confined on the scale of the optical narrow-line region by an unusually

dense and clumpy interstellar medium which may also be kinematically compli-
cated, or at least that the radio plasma and its environment are interacting heavily.
In the case of the GPS quasars, a dense and clumpy protogalaxy environment may
be the cause. In GPS galaxies, the dense and clumpy environment may be caused
by recent merger activity and a disruption of the nuclear region caused by material
infall.

Unfortunately, constraints on the conditions in the narrow-line regions of GPS
hosts, to support the above suggestions, are rare. O'Dea, Baum, and Stanghellini
[1991] list only two GPS galaxies which have reasonably well determined optical
spectra, PKS 1934−638 [Fosbury et al. 1987] and 2021+614 [Bartel et al. 1984].
The data for these two sources support the notion that the environments of GPS
sources are unusually dense and highly reddened.

Stanghellini et al. [1993] have obtained optical images of a large sample of
GPS hosts and find evidence for a high incidence of mergers. This is perhaps
not surprising since most of the objects are at high red shifts and higher merger
rates are predicated at high red shifts. It is not clear yet that GPS sources have a
stronger tendency for being involved in mergers.

For PKS 1718−649, as mentioned in the introduction, extensive optical imaging
and spectroscopic observations have been made. Fosbury et al. [1977], Carswell et
al. [1984], Filippenko [1985], and Keel and Windhorst [1991] note the existence of
a strong LINER spectrum and the possibility that high electron densities exist in
the nuclear region. From high quality data and a careful analysis Filippenko [1985]
concludes that the electron density near the nucleus, in the narrow-line region, is
very high, approximately 10^6 - 10^7 cm^{-3}. He also concludes that the densest clouds
live close to the nucleus and move most rapidly.

Véron-Cetty et al. [1995] have investigated the large amount of HI gas around
PKS 1718−649 and conclude from the overall kinematics that the system probably
arose from the recent merger of two galaxies, at least one of which was a gas rich
spiral. This conclusion may also explain the optical morphology of the galaxy. Its
spiral arms may be the tidally disrupted remains of the gas rich spiral. The $r^{1/4}$
behaviour of the inner region of the optical galaxy can also be explained in the
merger picture. Barnes and Hernquist [1991] show, with numerical simulations of
mergers which account for stars and gas, that the central region of the merger
product quickly relaxes into an $r^{1/4}$ profile.

Many properties of the PKS 1718−649 radio source are shared with the class
of GPS radio sources associated with galaxies. Although it is not as well defined a
GPS source it bears many strong resemblances to PKS 1934−638, one of the best
known examples of a GPS source, the major lacking being the broadness of the
peaked spectrum of PKS 1718−649. Optical and HI observations of the host galaxy
of PKS 1718−649 show strong evidence for a high density radio source environment
and a galaxy merger origin. These results are qualitative support for the broader
paradigm that the nuclear radio sources in GPS galaxies are confined by a dense
and clumpy environment which may have been induced by merger activity.

7.5   Conclusions

New radio data has been presented for PKS 1718−649 and existing radio and optical data from the literature have been reviewed. Two interpretations for the nature of PKS 1718−649 based on these data have been discussed. The first interpretation, that PKS 1718−649 is a core-jet radio source which is core dominated, receives little support although it cannot be ruled out completely. The major reason for rejection of this interpretation is the lack of evidence for a beamed component of synchrotron emission at radio or optical wavelengths, and the morphology of the pc-scale radio source.

The second interpretation appears to be more plausible, that PKS 1718−649 is a GHz Peaked-Spectrum radio source associated with a galaxy. The major evidence supporting this interpretation is that PKS 1718−649 fulfils all of the major criteria for GPS sources bar one, that GPS sources are highly luminous. This last point can be readily explained in terms of the selection biases on current samples of GPS radio sources. PKS 1718−649 also provides qualitative support for the suggestion of radio source confinement.

However, this interpretation is still somewhat uncertain. Further observations would be helpful for confirmation. Future VLBI observations will allow a determination of the speed of separation of the pc-scale components. If the source is a core-jet, a substantial apparent motion is expected; if a GPS source, no substantial motion is expected (c.f. Tzioumis *et al.* 1989). Monitoring of the radio flux density simultaneously at low and high radio frequency will determine if variability is present.

If PKS 1718−649 can be confirmed as a GPS source it will be an important discovery. At a red shift of z=0.014, it would be by far the nearest GPS source and allow unprecedented opportunities for investigation of the radio source and its environment with high spatial resolution and high sensitivity observations. Models for the suggested confinement of the radio source have been, up to recently, largely qualitative in their predictions and untestable due to the difficulty of observing the generally very distant GPS sources. However, models are becoming more rigorous (e.g. Bicknell and Dopita 1996, in preparation). High quality observations of a low red shift GPS source and its environment would be very valuable for testing new detailed models.

Chapter 8

The jet/cloud interaction in PKS 2152−699

8.1   Introduction

PKS 2152−699, at a red shift of 0.0282 [Tadhunter *et al.* 1988], is a powerful radio galaxy with a monochromatic luminosity of 5×10^{25} W Hz^{-1} at 5 GHz. It is one of the brightest radio sources in the sky at 2.3 GHz [Wall 1994] and was identified optically by Westerlund and Smith [1966].

The ATCA image of the kpc-scale radio structure [Fosbury *et al.* 1990] shows the double-lobed structure of FR II type radio sources. PKS 2152−699 is also known to harbour a pc-scale radio core between the two lobes. The astrometric VLBI observations of Reynolds *et al.* [1994] show that the core possesses an unresolved component on 800 km baselines at 2.3 and 8.4 GHz (angular resolution of approximately 4 mas at 8.4 GHz).

The optical counterpart to the radio source has been the target of observations which have revealed, in addition to strong nuclear emission line activity, a region of extra-nuclear activity with high ionisation emission lines and a highly polarised blue continuum [Tadhunter *et al.* 1987; di Serego Alighieri *et al.* 1988].

Tadhunter *et al.* [1988] report on extensive observations of the emission line regions and the kpc-scale radio source. They find the extra-nuclear emission line region (ENELR) to lie 10″ (∼5 kpc for H_o=75 km/s/Mpc) from the nuclear region, covering position angles between 35° and 50°. The north-east and south-west radio lobes lie approximately 46″ and 19″ respectively from the nuclear region and are connected along a position angle of 23°±2° [Tadhunter *et al.* 1988; Norris *et al.* 1990]. The properties of the ENELR and its near alignment with the radio axis led Tadhunter *et al.* [1988] to suggest it as the site of interaction between the radio jet connecting the central core and extended lobes, and a cloud of gas away from the

nuclear region of the galaxy. They suggest that the 12-25° misalignment between the radio structure and ENELR could be caused by the deflection of the radio jet in the interaction.

Similarities have been found between PKS 2152−699 and 3C277.3, a source for which evidence of jet/cloud interactions is persuasive [Miley *et al.* 1981; van Breugal *et al.* 1985]: the emission line spectra are similar, both possess a strong ionising continuum local to the emission line region, the radio axes and the optical axes are misaligned by similar amounts. Tadhunter *et al.* [1988] found that the photoionisation models they considered showed that the ENELR in PKS 2152−699 could be ionised by the source of continuum radiation found local to the ENELR but not by a source at the site of the active nucleus, unless the radiation is strongly anisotropic and concentrated in the direction of the cloud. They suggested that the local ionising source could possibly be produced in the interaction between the radio jet and the cloud. However, primarily on the basis of the blue continuum and optical polarisation of the ENELR, di Serego Alighieri *et al.* [1988] and Fosbury *et al.* [1990] strongly favour a scenario in which the cloud is ionised by a highly anisotropic photon beam which originates at the galaxy nucleus.

The aims of this chapter are as follows:

1] To present the first VLBI imaging observations of PKS 2152−699, strengthening the evidence for a jet/cloud interaction in this source.

2] To present a model which, based upon observational data, plausibly explains the relationship between the optical and radio structures associated with this galaxy.

The results of the VLBI imaging observations of the compact central component at the core of the PKS 2152−699, which show that the nuclear radio jet is closely aligned with the ENELR are presented in § 8.2. The evidence for the previously suggested interaction is therein strengthened. A simple mechanism which plausibly explains the misalignment between radio axis and ENELR, consistent with the concept of an extra-nuclear interaction, is explored in § 8.3.

8.2   Observations and Results

The observations described here were made at a frequency of 8.4 GHz, on 1994 February 26, with the following array of telescopes: Tidbinbilla (70 m), Parkes, Hobart, Mopra, and Narrabri. The data were obtained and processed as described in chapter 2.

The radio source is resolved into the core-jet morphology typical of many compact radio sources (Figure 8.1). A model of simple Gaussian components was generated (by initial reference to the image) to represent the core and jet components, and the parameters of the model optimised to fit the visibility amplitudes and closure phases by using the Caltech package task MODELFIT. The jet (north-east component) was shown to lie at a position angle of 44° ± 5° from the core (south-west component). The jet position angle was verified by de-convolving the core and jet components in the image from the beam using the AIPS task JMFIT. The de-convolved core dimensions of 2.4 × 0.7 mas and the core flux of 0.82 Jy

2152−699 observed at 8.418 GHz, 1994 Feb 26
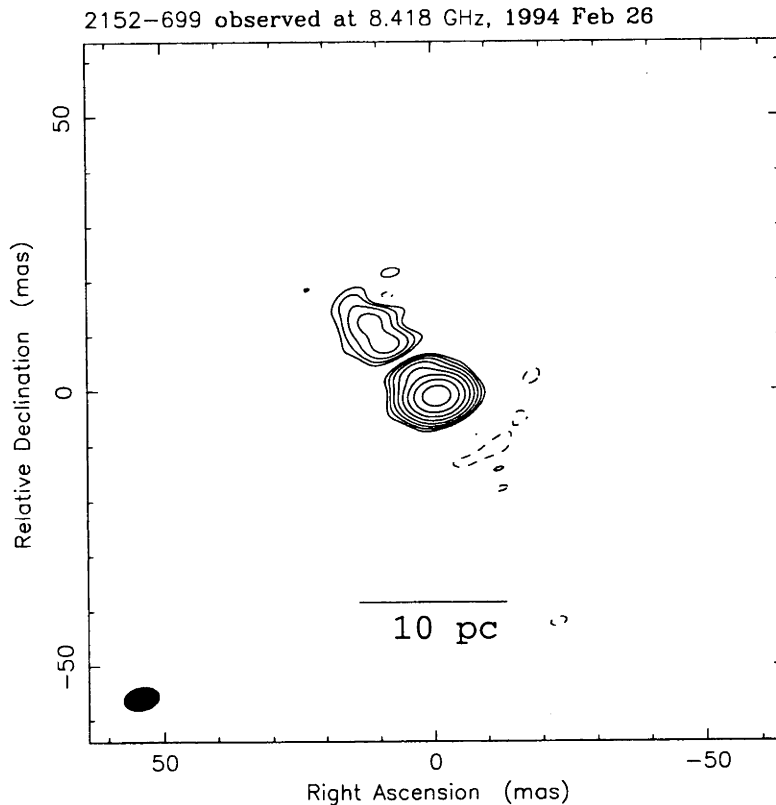
Figure 8.1: Map peak, 0.72 Jy/beam. Contours, -0.5, 0.5, 1, 2, 4, 8, 16, 32, 64% of peak. Beam FWHM, 6.4×4.2 @ -76.6°.

give a core brightness temperature of approximately 8.4×10^9 K at 8.4 GHz.

8.3   Discussion

The VLBI observations show that the position angle of the pc-scale jet aligns well with the ENELR but not with the north-east radio lobe. The position angle connecting the radio core and the north-east radio lobe is 27° ± 2° (adopting the error on the lobe-lobe position angle given by Tadhunter *et al.* [1988] as the error on the core-lobe position angle). Tadhunter *et al.* [1988] give the relative positions of the optical centroid and the radio lobes. Reynolds *et al.* [1994] and de Vaucouleurs *et al.* [1991] show the positions of the radio core and the optical centroid to be coincident ($\alpha_{radio} - \alpha_{optical} = -1.''02$, $\delta_{radio} - \delta_{optical} = -1.''05$. These radio/optical coordinate offsets are typical for sources at this declination, Jauncey *et al.* 1989). For comparison, the position angle connecting the radio core and the south-west radio lobe is 193°±2°. The position angles of the ENELR and the pc-scale radio jet from the core are 42°±7° and 44°±5° respectively.

    The suggestion of interaction between the radio jet and an extra-nuclear cloud is strengthened since the pc-scale jet does not simply align with the north-east radio lobe. The strong alignment of the pc-scale jet and the ENELR naturally

identifies the ENELR as the site of interaction. If this is the case, the radio jet
must be deflected through an angle of $20° \pm 5°$ so as to reach the radio lobe (see
Figure 8.2). Depending upon the three dimensional orientation of the radio source,
with respect to us, the true deflection angle will not be the same as the projected
deflection angle which we observe. Since no information on the orientation is
available, possible projection effects will be ignored here.
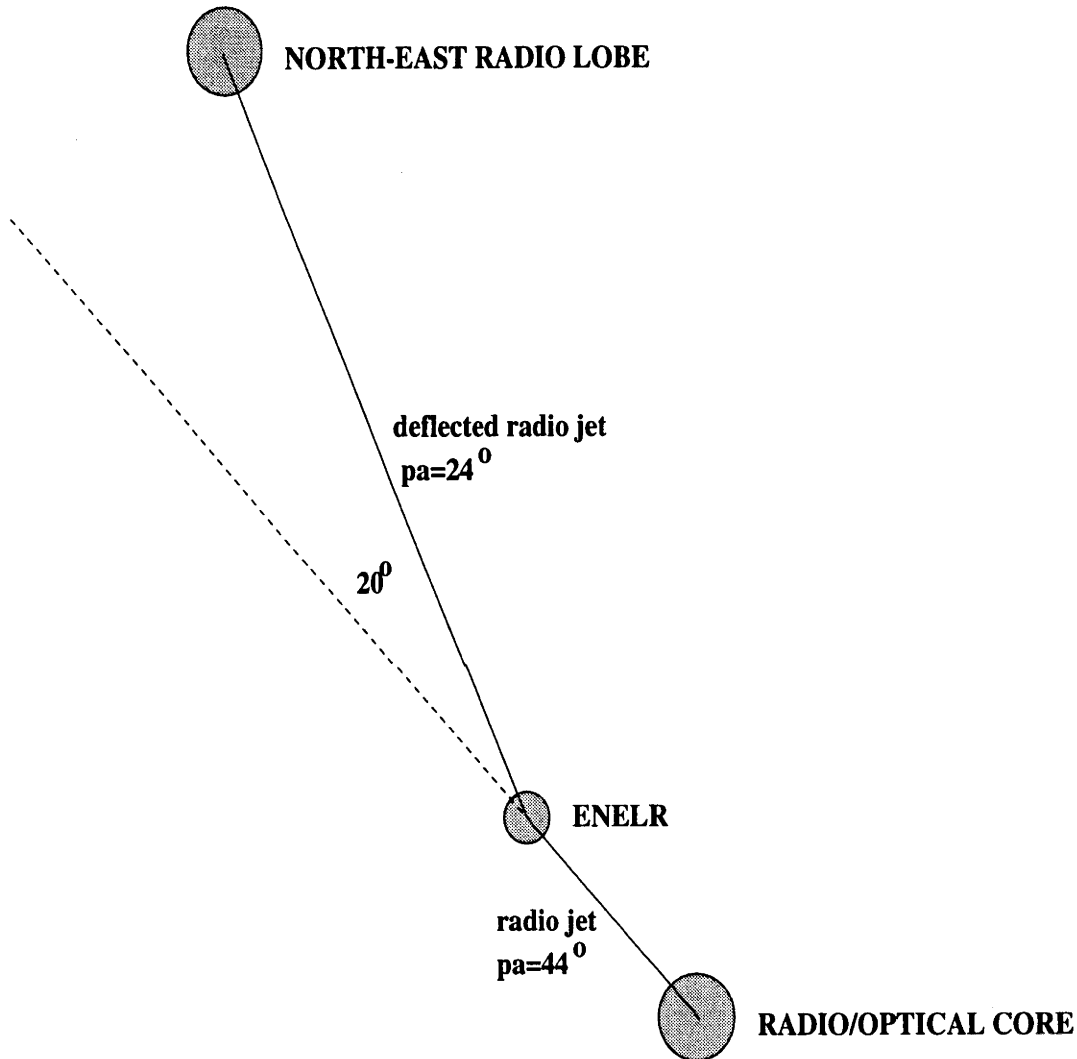
Figure 8.2: Schematic of jet/cloud interaction in PKS 2152—699

It is possible to characterise the deflection of a collimated jet with oblique
shocks (see Bicknell [1994], section 4.2, equations and references therein) which
can be set up when a low-density jet encounters an interface with a much denser
region. The deflection of a relativistic jet by a planar shock which lies obliquely
to the direction of flow in the jet has been modelled (Figure 8.3a). In particular,
this model has been used with the value for the jet deflection estimated above for
PKS 2152—699 to derive some parameters of the relativistic jet. In this case the
relativistic jet is the radio jet and the interface with the dense region is the surface
of the extra-nuclear cloud.

    The model constrains the shock strength (defined as the reciprocal of the com-
pression caused by the shock, $1/k$) and the Lorentz factors of the jet material in
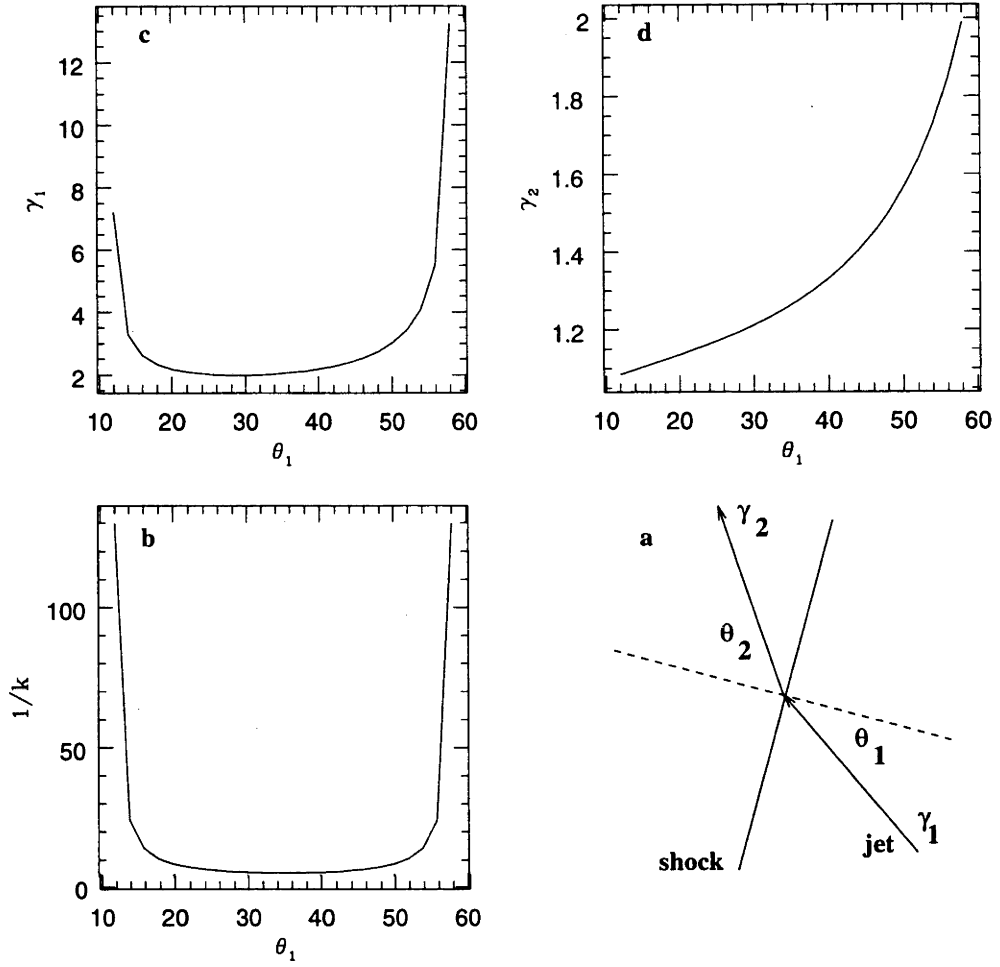
Figure 8.3: Results of oblique shock model for the PKS 2152−699 data

the pre-shock and post-shock regions, γ_1 and γ_2 respectively. The free parameter is the shock obliqueness θ_1 and the jet deflection is $\theta_d = \theta_2 - \theta_1$. The relationship between θ_1, θ_2, θ_d and k is

$$tan\theta_2 = \frac{3/k+1}{3+1/k} tan\theta_1 = tan(\theta_1 + \theta_d) \quad .$$

Following Landau and Lifshitz [1984] and Bicknell [1994], the x and y components of the jet speed with respect to the shock can be calculated. The x direction is perpendicular to the shock and the y direction is parallel to the shock:

$$\beta_{1x} = \frac{1}{\sqrt{f(k) + tan^2\theta_1}} \quad ,$$

$$\beta_{2x} = \frac{1}{\sqrt{g(k) + tan^2(\theta_1 + \theta_d)}} \quad ,$$

$$\beta_{1y} = \beta_{1x} tan\theta_1 = \beta_{2x} tan(\theta_1 + \theta_d) = \beta_{2y} = \beta_y \quad ,$$

where $f(k) = \frac{3(3+1/k)}{(3/k+1)}$ and $g(k) = \frac{3(3/k+1)}{(3+1/k)}$. For each value of the free parameter, θ_1, a unique value can be found for the compression caused by the shock, $1/k$, and consequently unique values of β_{1x}, β_{2x}, and β_y can be calculated. γ_1 and γ_2 can therefore be calculated.

The results of the model can be seen in Figures 8.3b, 8.3c and 8.3d. The plots show that the required deflection angle of 20° can be achieved for the values of shock strength and Lorentz factor shown by the solid lines as a function of shock obliqueness.

Notably, the required deflection can be achieved over a wide range in obliqueness ($\sim 30°$) with shock strengths of <10 and the Lorentz factor of a relativistic pre-shock jet ($\gamma < 3$) . These values are reasonable since higher Lorentz factors have been inferred for the pc-scale radio jets in quasars (eg Vermeulen and Cohen 1994). It may be that in high power radio sources, such as PKS 2152−699, the radio jet is still relativistic on kpc-scales (eg Bridle and Perley 1984).

Finally, these observations have relevance for the ionisation of the extra-nuclear cloud. Since evidence for a jet/cloud interaction has now been strengthened it appears plausible that some excitation of the extra-nuclear cloud may occur in the interaction. However, the alternative hypothesis that postulates ionisation by a photon beam from the nucleus is also supported by the VLBI observations since in all reasonable models the photon beam and the pc-scale radio jet share the same directionality. Hence the extra-nuclear cloud will lie in the path of any existing 'blazar' beam from the nucleus.

It is not unlikely that both mechanisms may play a role in the excitation of the extra-nuclear cloud.

8.4   Conclusions

The first VLBI image of the powerful radio galaxy PKS 2152−699 has been presented. This image shows that the pc-scale radio jet is aligned closely with the ENELR, but not the kpc-scale radio lobe to the north-east of the radio/optical core. These results favour the interpretation of Tadhunter *et al.* [1988], who suggest that the radio jet from the core could be interacting with an extra-nuclear cloud of gas, causing the radio jet to be deflected in the process. A mechanism, consistent with this interpretation, which can reproduce the observed misalignment between the kpc-scale radio structure and the ENELR has been explored. The resultant model uses oblique shocks and a relativistic jet to produce the observed (projected) 20° jet deflection. The excitation of the ENELR could be due to both the jet/cloud interaction and the effects of a photon beam from the nucleus.

Chapter 9

Concluding remarks

A study of 12 compact radio sources (11 extragalactic and 1 Galactic) was conducted over a period of approximately 4 years with the Southern Hemisphere VLBI Experiment array. The main focus of this work has been on six nearby, bright, and compact radio sources which make up the Southern Hemisphere component of a "Whole-Sky" sample of such sources.

Particular emphasis has been placed on determining the structure and evolution in these sources at high spatial resolution and investigating relationships between the compact structure/evolution and emission at other wavelengths.

Results from the Southern Hemisphere study are summarised in the next section. Then a brief summary of the Northern Hemisphere sources, from already published results, is given and the overall VLBI properties of the "Whole-Sky" sample are considered.

9.1 The Southern Hemisphere component

PKS 0518−458 (Pictor A) is a low red shift (z=0.035) Fanaroff-Riley type II radio galaxy. At pc-scale resolution a one-sided jet-like structure is orientated so that the jet is directed at the hot spot in the north-west radio lobe. From the SHEVE observations, and simulations, it was found that there is some difficulty accepting that the optical jet suggested from sub-arcsecond imaging with the HST is real.

PKS 0521−365 (2EG J0524−3630) is the second closest extragalactic (z=0.055) radio source to be identified as a source of greater than 100 MeV gamma-rays by the EGRET instrument. With multi frequency SHEVE observations, the core of the radio source was identified and with multi epoch observations evolution was searched for. Some evidence for motion in the pc-scale jet was obtained but the period over which the source was observed was not sufficient to show significant change. The pc-scale radio jet aligns accurately with a kpc-scale radio and optical jet. The brightness temperature of the radio core is approximately 1.0×10^{11} K, well below the nominal limit for synchrotron radiation. As such, PKS 0521−365 is not likely to be a highly beamed source. PKS 0521−365 is thus an example of a gamma-ray source which does not fit the paradigm of Salamon & Stecker [1994], in which gamma-ray sources have a relativistic jet aligned with our line of sight.

PKS 1322−427 (Centaurus A, NGC 5128) is the closest active extragalactic radio galaxy to us, at a distance of approximately 3.5 Mpc. The extensive SHEVE observations presented here have unambiguously identified the core of the radio

source for the first time and have followed over a period of approximately 4.3 years the evolution in the sub-pc-scale jet. The evolution in Centaurus A consists of the steady linear motion of one component close to the core, C2, as well as irregular and dramatic changes in the internal structure of a more complicated component further from the core, C1. High resolution and high quality VLBI images from the combination of SHEVE and VLBA data have revealed for the first time a sub-pc-scale radio counterjet. The dual frequency observations used to identify the core support the possible existence of a free-free absorbing structure which surrounds the core and may take the form of a pc-scale disk or torus of ionised material.

PKS 1514–241 (AP Libræ) is a low red shift (z=0.049) BL Lac type object which hosts a core dominated radio source. The SHEVE observations have revealed a slightly resolved pc-scale jet which is misaligned with the kpc-scale radio structure as seen with the VLA. Higher angular resolution observations will be required to determine more detail. The VLBI data on PKS 1514–241 was used in the investigation of gamma-ray emission from AGN as an example of a beamed radio source at low red shift which has not been identified as a gamma-ray source.

PKS 1718–649 (NGC 6328) is likely to be the lowest red shift (z=0.014) member of the GHz Peaked-Spectrum (GPS) class of radio sources found to date. Evidence for this comes from the pc-scale morphology as seen with the SHEVE observations, the kpc-scale radio structure and radio polarisation as seen with the ATCA, and the radio spectrum over almost 3 orders of magnitude in frequency, from 408 MHz to 230 GHz. Evidence that the radio source is not the typical core-jet source observed in many radio galaxies comes from optical imaging and optical spectroscopy. There is also some evidence from optical spectroscopy and HI imaging observations supporting suggestions that GPS radio sources are confined by an unusually dense or confused AGN environment which could possibly be caused by merger activity.

PKS 2152–699 (z=0.028) is a radio source which appears to be morphologically intermediate between the FR I and FR II classes, but above the FR I/FR II luminosity break. It is associated with a host galaxy which has the unusual property of nuclear-like optical emission some 5 kpc from the galaxy nucleus. There is a direct connection between the kpc-scale radio and optical structures, although they are misaligned. The SHEVE observations show that the inner radio jet in this galaxy is highly aligned with the extra-nuclear optical structure, strengthening the evidence supporting previous suggestions that the jet and a cloud of gas interact at the site of the extra-nuclear optical emission, the jet being deflected in the interaction. A model has been developed and presented which describes the deflection of the jet, showing that such an interaction is plausible, given the data from radio and optical observations.

9.2   The Northern Hemisphere component

0316+413 (3C84, Perseus A) is a nearby Seyfert galaxy (z=0.0172) with a compact radio source in excess of 30 Jy at 22 GHz, which accounts for the great majority of the total flux density of the source. The sub-pc-scale structure consists of a bright core component and a strong jet-like elongation extending approximately 10 mas from the core toward the south. A newly discovered component

to the north of the core has been detected at 8.4 and 22 GHz. This component has been identified as a pc-scale counterjet [Walker, Romney, & Benson 1994; Vermeulen, Readhead, & Backer 1994]. The spectral index of the counterjet suggests that a free-free absorbing disk or torus is partly obscuring our view of it [Vermeulen, Readhead, & Backer 1994]. Subluminal motions have been observed on the pc-scale ranging from 0.14 $h^{-1}c$ [Vermeulen, Readhead, & Backer 1994] to 0.58 $h^{-1}c$ [Marr *et al.* 1989].

0402+372 (z=0.0504) has a complex pc-scale morphology consisting of a jet-like structure approximately 40 mas long at a position angle of approximately 30° [Polatidis *et al.* 1995]. Only a single epoch of VLBI imaging was found from the literature. The kpc-scale radio structure has been imaged with the VLA [Xu *et al.* 1995], revealing a bright core component and a diffuse, double-lobed structure which straddles the core along a position angle of approximately 30° and has a lobe-to-lobe angular extent of approximately 15″.

0430+052 (3C120) is a Seyfert galaxy (z=0.033) with an associated radio structure consisting of a jet which is observable on scales between 0.5 pc and 100 kpc, and diffuse lobes on scales up to 400 kpc [Walker, Benson, & Unwin 1987]. The kpc-scale structure is complex, the jet bending significantly. On the pc-scale, a strong, one-sided, 50 mas jet is directed to the west, away from a bright core component. Measurements of the apparent motion of components in the jet have yielded speeds between 2 and 4 times the speed of light [Walker, Benson, & Unwin 1987]. 3C120 is therefore the lowest red shift extragalactic superluminal radio source. The closest superluminal source is, of course, GRO J1655−40.

1228+127 (M87, NGC 4486, Virgo A) is the closest active radio source which is easily accessible with Northern Hemisphere VLBI arrays, at a distance of approximately 16 Mpc. On the kpc-scale, a complex radio and optical jet has been imaged with the VLA and HST [Sparks, Biretta, & Macchetto 1994]. On the pc-scale, a strongly one-sided jet has been observed with VLBI [Reid *et al.* 1989]. A subluminal, ∼0.3c, speed has been measured for components within the pc-scale jet. Limb brightening and oscillations in the pc-scale surface brightness distribution have also been observed.

1652+398 (z=0.038) is a core dominated radio source associated with a BL Lac type object. The pc-scale morphology is extremely complex, consisting of a bright core component and a series of four elongated components (∼40 mas each) which extend away from the core for over 100 mas, separated by approximately 30 mas, at a position angle of approximately 45°. However, each of the components is orientated with major axes at position angles of approximately 135°. The kpc-scale radio structure has been imaged by Ulvestad, Johnston, & Weiler [1983], revealing a bright core and weak diffuse extended (∼10″) emission either side of the core at a position angle of approximately 45°.

1807+698 (z=0.051) is another core dominated radio source associated with a BL Lac type object. The pc-scale morphology consists of a bright core component and a straight jet at a position angle of approximately −100° and extending 50 mas. The kpc-scale radio structure has been imaged [Ulvestad & Johnston 1984], revealing a bright core component with a surrounding diffuse halo of radius approximately 1′.

9.3 VLBI properties of the "Whole-Sky" sample

For the first time, VLBI observations of a "Whole-Sky" sample of radio sources at low red shift and with compact radio emission at or above the level of 1 Jy can be assembled. The sample, summarised in § 9.1 and § 9.2, consists of 12 sources. 6/12 lie in the Northern Hemisphere and 6/12 lie in the Southern Hemisphere. The six Southern Hemisphere sources have been studied in this thesis for the first time.

The 12 sources can be broken down into the following sub-classes: 3/12 are associated with BL Lac type objects (PKS 1514−241, 1652+398, and 1807+698), 2/12 are associated with Seyfert galaxies (0316+413 and 0430+052), 2/12 are FR I type radio galaxies (1228+127 and PKS 1322−427), 3/12 show evidence for kpc-scale jets and lobes but cannot be easily classified as type FR I or FR II (0402+379, PKS 0521−365, and PKS 2152−699), 1/12 is an FR II type radio galaxy (PKS 0518−458), and 1/12 is a GHz Peaked-Spectrum radio source (PKS 1718−649).

This sample contains a rich diversity of radio sources and an equally rich diversity in the properties of the host galaxies. This diversity is encouraging since examples of all major classes of extragalactic radio source are present in the sample.

The "Whole-Sky" sample may already be able to guide our understanding in some areas. For instance, only one source in the sample, 0430+052, is an apparently superluminal source. The remaining sources in the sample which have had well measured pc-scale component motions (0316+413, 1228+127, and PKS 1322−427) have subluminal speeds, until recently conflicting with the strong one-sidedness of the pc-scale jets, which indicates a highly relativistic motion for the emitting material.

Some of this conflict has recently been resolved with the discovery of pc-scale counterjets in 0316+413 (3C84, Perseus A) and PKS 1322−427 (NGC 5128, Centaurus A). However, the work presented in chapter 5 shows that the measured speed in PKS 1322−427 is still inconsistent with the observed counterjet. For 1228+127 very high dynamic range VLBI maps reveal no counterjet, again inconsistent with the measured component speeds if those speeds are assumed to be the true speed of the jet. The often cited escape from this problem is to allow the jet to travel at a much faster speed than the components which are observed, the component speeds suggested to be pattern speeds on top of an underlying faster flow.

However, the problem may be complicated somewhat by the suggestion that large amounts of free-free absorbing material can cause apparent asymmetries in pc-scale radio sources, in addition to the effects of Doppler beaming. Evidence for significant free-free absorption on the pc-scale has been presented for two sources in the "Whole-Sky" sample, 0316+413 and PKS 1322−427.

These results show that the pc and sub-pc-scales in radio galaxies are extremely complicated, with the jets and their environments intimately connected. Further observations of the nearby radio galaxies offer the best opportunities for a better understanding of the conditions in the jet and its environment within a few pc of the core.

Another area where we can gain a better understanding is in the study of the GHz Peaked-Spectrum radio sources. The discovery of the lowest red shift GHz Peaked-Spectrum radio source is a very significant result from this thesis. PKS 1718−649 is at a red shift which allows highly detailed radio imaging with

VLBI but more importantly high spatial resolution optical investigations. With HST resolution the inner 100 pc of the AGN could be imaged, revealing for the first time the region close to the radio source.

Models for GPS sources rely upon a confining medium to constrain the radio source to sub-galactic dimensions, implying heavy interactions between the expanding radio source and its environment. It is this interaction which may drive the strong optical emission observed for GPS sources. High spatial resolution, narrowband optical imaging of PKS 1718−649 may allow direct tests of models for GPS sources. PKS 1718−649 is unique in this respect. Other GPS sources are too far away to allow the appropriate resolution to be achieved.

Finally, in a broader sense, VLBI observations of the nearby sources may add to our understanding in unexpected ways. For instance, the SHEVE observations of PKS 2152−699 revealed a relationship between the optical and radio structure over 4 orders of magnitude in spatial scale, from the pc-scale to the scale of tens of kpc.

Future observations of all the objects in the "Whole-Sky" sample will be important for our understanding of similar sources which lie at higher red shifts and hence do not allow such detailed investigations. This is perhaps where the greatest value of the "Whole-Sky" sample lies, in providing a list of sources to attack with observations over a wide range in wavelength and resolution. In this way we can strive to understand individual sources in detail and hence improve our understanding of the rest of the radio loud AGN population.

9.4 Other results

Although the emphasis of this thesis was on the "Whole-Sky" sample, two related investigations included in this thesis have produced significant results. The first of these was the comparison of the VLBI properties of the EGRET-identified radio sources with the VLBI properties of similar radio sources not identified by EGRET. This work was prompted by the identification of PKS 0521−365 by EGRET. The properties which were compared were the apparent speeds in VLBI jets, the radio core brightness temperatures and pc-scale to kpc-scale jet misalignment angles. These properties are indicators of relativistic beaming which might be used to determine the differences or similarities in the beaming properties between the populations of gamma-ray loud and quiet radio sources. Relativistic beaming lies at the heart of many models for AGN gamma-ray emission.

The comparison in chapter 4 finds no significant evidence to support a difference in the beaming properties based on apparent jet speeds or misalignment angles. Some evidence exists suggesting that EGRET-identified radio sources have higher radio core brightness temperatures than similar radio sources not identified by EGRET. The comparison was based on new observations and observations from the literature.

A strong conclusion of the work was that a very wide variety of properties are associated with gamma-ray radio sources, and that a one-to-one relationship between beamed radio emission and beamed gamma-ray emission is not tenable.

The second additional investigation was the study of GRO J1655−40 with the SHEVE array. GRO J1655−40 was discovered as a new, bright X-ray source with

BATSE on 1994 July 27. The SHEVE array was used to image the compact radio source which subsequently appeared.

The SHEVE observations revealed a jet-like structure which expanded at the rate of 65 mas/day, causing difficulties in the data reduction which were overcome by reducing the size of the imagable data sets. The high angular rate was confirmed. With distance measurements the angular motion corresponded to an apparent speed of expansion of between 1.1 and 1.9 times the speed of light. GRO J1655−40 was the second Galactic superluminal source to be discovered after GRS 1915+105. Taking the geometry of the GRO J1655−40 jet into account, the intrinsic speed was shown to be at least mildly relativistic.

The combination of multi frequency observations with the SHEVE and other VLBI observations reveal a strong empirical link between the accretion of material onto a compact mass and the production of relativistic jets.

9.5   Future work

The first and most obvious avenue for future work is the continued monitoring of the radio sources mentioned here, to follow any evolution in the sources over an extended period of time. These observations will be important for all of the sources but especially important for PKS 1718−649 since they may further confirm the GPS nature of the source. This type of observation is also particularly important for the gamma-ray loud and gamma-ray quiet radio sources since apparent superluminal motions provide some indication of the importance of relativistic beaming. These observations have already been approved as future SHEVE experiments.

The value of monitoring sources over an extended period is illustrated through the work presented in chapter 5 on Centaurus A. In the particular case of Centaurus A, this work has indicated that very rapid evolution is taking place on the sub-pc-scale. The future monitoring of Centaurus A should be undertaken with a higher temporal frequency, so that the rapid evolution can be better sampled. These observations are currently underway (1996 February - 1996 June) at the VLBA with a frequency of 8.4 GHz and a temporal spacing of approximately one month.

A major opportunity for future investigations of the sources described in this thesis will be provided by the VLBI Space Observatory Programme (VSOP) space VLBI mission, which will be launched into Earth orbit in 1996 September. This mission will result in an imaging VLBI array with a maximum resolution of approximately 50μas, at 22 GHz. One of the goals of the mission is to provide very high resolution images of the unresolved radio cores of AGN. This capability will be used to the best advantage for Centaurus A, the closest active radio source and hence the best target for the high resolution investigation of a radio core. The SHEVE team has been awarded VSOP time to investigate the Centaurus A radio core.

A major goal of the VSOP mission is to extend VLBI baselines to the extent where accurate high radio core brightness temperatures can be measured and used as an indicator of relativistic beaming. These observations perhaps represent the best opportunity to test models which attempt to explain the differences between gamma-ray loud and gamma-ray quiet AGN in terms of relativistic beaming. The observation of radio core brightness temperatures above approximately 10^{12} K give

a direct estimate of the Doppler factor for relativistic beaming. The author is principal investigator on a successful VSOP proposal to investigate gamma-ray loud and gamma-ray quiet blazars in the Southern Hemisphere.

9.6   Refereed Publications

Jones, D.L., Tingay, S.J., Murphy, D.W., Meier, D.L., Jauncey, D.L., Reynolds, J.E., Tzioumis, A.K., Preston, R.A., McCulloch, P.M., Costa, M.E., Kemball, A.J., Nicolson, G.D., King, E.A., Lovell, J.E.J., Clay, R.W., Ferris, R.H., Gough, R.G., Sinclair, M.W., Ellingsen, S.P., Edwards, P.G., & Jones, P.A.
Submitted to ApJLett (March 1996)
Discovery of a sub-parsec-scale counterjet in the nucleus of Centaurus A

Mollenbrock, G.A., Fujisawa, K., Preston, R.A., Gurvits, L.I., Dewey, R.J., Hirabayashi, H., Inoue, M., Iwata, T., Jauncey, D.L., Kameno, S., Migenes, V., Roberts, D.H., Schilizzi, R.T., & Tingay, S.J.
1996, AJ accepted (to appear June 1996)
A 22 GHz VLBI survey of 140 compact extragalactic radio sources

Tingay, S.J., Edwards, P.G., Costa, M.E., Lovell, J.E.J., McCulloch, P.M., Jauncey, D.L., Reynolds, J.E., Tzioumis, A.K., Migenes, V., Gough, R., King, E.A., Jones, D.L., Preston, R.A., Murphy, D.W., Meier, D.L., van Ommen, T.D., St John, M., Hoard, D.W., Nicolson, G.D., Wan, T.-S., & Shen, Z.-Q.
1996, ApJ accepted (to appear June 10).
VLBI Observations of Southern EGRET Identifications. I. PKS 0208−512 PKS 0521−365, and PKS 0537−441

Tingay, S.J., Jauncey, D.L., Reynolds, J.E., Tzioumis, A.K., Migenes, V., Gough, R., Lovell, J.E.J., McCulloch, P.M., Costa, M.E., Preston, R.A., & Harbison, P.
1996, AJ 111, 718
Parsec-Scale Morphology of PKS 2152-699 and the Radio/Optical Misalignment

Tingay, S.J.
1996, Pub.Ast.Soc.Aust 13, 103
Some Intrinsic Properties of VLBI Jets.

Jauncey, D.L., Tingay, S.J., Preston, R.A., Reynolds, J.E., Lovell, J.E.J., McCulloch, P.M., Tzioumis, A.K., Costa, M.E., Murphy, D.W., Meier, D.L., Jones, D.L., Amy, S.W., Biggs, J.D., Blair, D.G., Clay, R.W., Edwards, P.G., Ellingson, S.P., Ferris, R.H., Gough, R.G., Harbison, P., Jones, P.A., King, E.A., Kemball, A.J., Migenes, V., Nicolson, G.D., Sinclair, M.W., Van Ommen, T., Wark, R.M., & White, G.L.
1995, Proc.Nat.Acad.Sci.USA, 92, 11368
Sub-Parsec-Scale Structure and Evolution of Centaurus A.

Continued over page

Norris, J.E., da Costa, G., and Tingay, S.J.
1995, ApJS 99, 637
Equivalent Widths for 54 Globular Cluster Red Giants.

Tingay, S.J., Jauncey, D.L., Preston, R.A., Reynolds, J.E., Meier, D.L., Murphy,
D.W., Tzioumis, A.K., McKay, D.J., Kesteven, M.J., Lovell, J.E.J., Campbell-
Wilson D., Ellingsen, S.P., Gough, R., Hunstead, R.W., Jones, D.L., McCulloch,
P.M., Migenes, V., Quick, J., Sinclair, M.W., & Smits, D.
1995, Nature 374, 141
Relativistic Motion in a Nearby Bright X-ray Source.

Tingay, S.J., Jauncey, D.L., Preston, R.A., Reynolds, J.E., Meier, D.L., Tzioumis,
A.K., Jones, D.L., King, E.A., Amy, S.W., Biggs, J.D., Blair, D.G., Campbell-
Wilson, D., Clay, R.W., Costa, M.E., Edwards, P.G., Ferris, R.H., Gough, R.G.,
Harbison, P., Hoard, D.W., Jones, P.A., Lovell, J.E., Kemball, A.J., McAdam,
W.B., MacCleod, G., McCulloch, P.M., Migenes, V., Murphy, D.W., Nicolson,
G.D., Quick, J.F.H., Sinclair, M.W., Skjerve, L., St John, M.E., Van Ommen, T.,
Wark, R.M., & White, G.L.
1994, Aust.J.Phys 47, 619-624.
Centaurus A, the Core of the Problem.

9.7   Conference Proceedings

Tingay, S.J., Jauncey, D.L., Preston, R.A., Meier, D.L., Reynolds, J.E., Tzioumis,
A.K., Lovell, J.E.J., Jones, D.L., McCulloch, P.M., Murphy, D.W., & Nicolson,
G.D.
1996, in Proc. IAU symposium 175 (Bologna), in press
VLBI Observations of Low-Redshift Radio Galaxies

Tzioumis, A., Morganti, R., Tadhunter, C., Dickson, R., Fanti, C., Dalacasa, D.,
Reynolds, J., Jauncey, D., Preston, R., McCulloch, P., King, E., Tingay, S., Ed-
wards, P., Costa, M., Jones, D., Lovell, J., Clay, R., Meier, D., Murphy, D., Gough,
R., Ferris, R., White, G., & Jones, P.
1996, in Proc. IAU symposium 175 (Bologna), in press
High-Resolution Structure of Southern Compact Steep Spectrum Sources

Preston, R.A., Tingay, S.J., Jauncey, D.L., Reynolds, J.E., Lovell, J.E.J., McCul-
loch, P.M., Tzioumis, A.K., Costa, M.E., Murphy, D.W., Meier, D.L., Jones, D.L.,
Clay, R.W., Edwards, P.G., Ellingsen, S.P., Ferris, R.H., Gough, R.G., Harbison,
P., Jones, P.A., King, E.A., Kemball, A.J., Migenes, V., Nicolson, G.D., Sinclair,
M.W., van Ommen, T.D., Wark, R.M., & White, G.L.
1996, in Proc. IAU symposium 175 (Bologna), in press
Monitoring the Jet in Centaurus A at 0.1 pc Resolution

Jones, D.L., Tingay, S.J., Preston, R.A., Jauncey, D.L., Reynolds, J.E., Lovell, J.E.J., McCulloch, P.M., Tzioumis, A.K., Costa, M.E., Murphy, D.W., Meier, D.L., Clay, R.W., Edwards, P.G., Ellingsen, S.P., Ferris, R.H., Gough, R.G., Harbison, P., Jones, P.A., King, E.A., Kemball, A.J., Migenes, V., Nicolson, G.D., Sinclair, M.W., van Ommen, T.D., Wark, R.M., & White, G.L.
1996, in Proc. IAU symposium 175 (Bologna), in press
A Counterjet in the Nucleus of Centaurus A

Lovell, J.E.J., Tingay, S.J., Edwards, P.G., Jauncey, D.L., & Preston, R.A.
1996, in Proc. IAU symposium 175 (Bologna), in press
VLBI Observations of Southern EGRET Identifications

Tingay, S.J., Jauncey, D.L., Reynolds, J.E., Tzioumis, A.K., King, E.A., Preston, R.A., Meier, D.L., Murphy, D.W., Jones, D.L., McCulloch, P.M., Lovell, J.E.J., Costa, M.E., & Nicolson, G.D.
1996, in Energy Transport in Quasars and Radio Galaxies, ASP Conf. Series, Vol. 100, eds. P.E. Hardee, A.H. Bridle, & J.A. Zensus, in press
Sub-Parsec-Scale Structure and Evolution of the Centaurus A Radio Jet

Tingay, S.J., Jauncey, D.L., Preston, R.A., Reynolds, J.E., Tzioumis, A.K., Lovell, J.E.J., Costa, M.E., Murphy, D.W., Meier, D.L., McCulloch, P.M., Jones, D.L., Amy, S.W., Clay, R.W., Edwards, P.G., Ellingsen, S.P., Ferris, R.H., Gough, R.G., Harbison, P., Jones, P.A., King, E.A., Kemball, A.J., Migenes, V., Nicolson, G.D., Sinclair, M.W., van Ommen, T.D., Wark, R.M., & White, G.L.
1996, in Proc. Jets from Stars and AGN (Bad Honnef)
The Sub-Parsec-Scale Structure and Evolution of the Jet in Centaurus A

Tingay, S.J., Jauncey, D.L., Preston, R.A., Reynolds, J.E., Meier, D.L., Murphy, D.W., Tzioumis, A.K., McKay, D.J., Kesteven, M.J., Lovell, J.E.J., Campbell-Wilson, D., Ellingsen, S.P., Gough, R.G., Hunstead, R.W., Jones, D.L., McCulloch, P.M., Migenes, V., Quick, J., Sinclair, M.W., & Smits, D.
1996, in Proc. Jets from Stars and AGN (Bad Honnef)
Southern Hemisphere VLBI Observations of GRO J1655−40

Moellenbrock, G., Fujisawa, K., Preston, R., Gurvits, L., Dewey, R., Hirabayashi, H., Inoue, M., Jauncey, D., Migenes, V., Roberts, D., Schilizzi, R., Tingay, S., & Zensus, A.
1995, In proceedings of 2nd EVN/JIVE symposium. Eds Kus, A.J., Schilizzi, R.T., Borkowski, K.M., and Gurvits, L.I., Torun Radio Astronomy Observatory.
22 GHz VLBI Survey: Status Report and Preliminary Results.

Tingay, S.J.
1995, Southern Sky May/June
A black hole in our galaxy?: High resolution radio observations of the Galactic X-ray source GRO J1655-40.

Mollenbrock, G., Fujisawa, K., Preston, R., Gurvits, L., Dewey, R., Hirabayashi, H., Inoue, M., Jauncey, D., Migenes, V., Roberts, D., Schilizzi, R., Tingay, S., & Zensus, A.
1995, BAAS, 27, 822
A 22 GHz Baseline VLBI Survey of 142 AGN

Murphy, D.W., Tingay, S.J., Jauncey, D.L., Preston, R.A., Reynolds, J.E., Meier, D.L., Tzioumis, A.K., & Jones, D.L.
1994, BAAS vol. 26, no. 4, 1518
A Relativistically Expanding Radio Source associated with GRO J1655-40.

Bibliography

[Antonucci & Ulvestad 1985] Antonucci, R.R.J & Ulvestad, J.S. 1985, ApJ, 294, 158

[Bailyn et al. 1995a] Bailyn, C.D. et al. 1995a, Nature, 374, 701

[Bailyn et al. 1995b] Bailyn, C.D. et al. 1995b, IAU Circ 6173

[Barnes & Hernquist 1991] Barnes, J.E. & Hernquist, L.E. 1991, ApJ, 370, L65

[Bartel et al. 1984] Bartel, N., Shapiro, I.I., Huchra, J.P., & Kuhr, H. 1984, ApJ, 279, 112

[Barthel et al. 1995] Barthel, P.D., Conway, J.E., Myers, S.T., Pearson, T.J., & Readhead, A.C.S. 1995, ApJ, 444, L21

[Bertsch et al. 1993] Bertsch, D.L. et al. 1993, ApJLett, 405, L21

[Bicknell 1994] Bicknell, G.V. 1994, ApJ, 422, 542

[Bignami & Hermsen 1983] Bignami, G.F. & Hermsen, W. 1983, ARA&A, 21, 67

[Biretta, Moore & Cohen 1986] Biretta, J.A., Moore, R.L., & Cohen, M.H. 1986, ApJ, 308, 93

[Blandford & Konigl 1979] Blandford, R.D. & Konigl, A. 1979, ApJ, 232, 34

[Bolton, Clarke & Ekers 1965] Bolton, J.G., Clarke, M.E., & Ekers, R.D. 1965, Aust.J.Phys., 18, 627

[Bolton, Stanley, & Slee 1949] Bolton, J.G., Stanley, G., & Slee, O.B. 1949, Nature, 164, 101

[Botti & Abraham 1993] Botti, L.C.L. & Abraham, Z. 1993, MNRAS, 264, 807

[Bowden et al. 1993] Bowden, C.C.G. et al. 1993, in 'Proc. 23rd ICRC' (Calgary), 1, 294

[Bridle & Perley 1984] Bridle, A.H. & Perley, R.A. 1984, ARA&A, 22, 319

[Broderick et al. 1972] Broderick, J.J., Kellermann, K.I., Shaffer, D.B., & Jauncey, D.L. 1972, ApJ, 172, 299

[Burns, Feigelson, & Schreier 1983] Burns, J.O., Feigelson, E.D., & Schreier, E.J. 1983, ApJ, 273, 128

[Campbell-Wilson & Hunstead 1994] Campbell-Wilson, D. & Hunstead, R. 1994, IAU Circ. 6052

[Carswell et al. 1984] Carswell, R.F., Baldwin, J.A., Atwood, B., & Phillips, M.M. 1984, ApJ, 286, 464

[Cohen et al. 1975] Cohen, M.H. et al. 1975, ApJ, 201, 249

[Clark 1995] Clark, B.G. 1995, in 'Very Long Baseline Interferometry and the VLBA', ASP conference series (Eds J.A. Zensus, P.J. Diamond, & P.J. Napier), 82, 3

[Clark 1973] Clark, B.G. 1973, Proc. IEEE, 61, 1242

[Clarke, Burns, & Norman 1992] Clarke, D.A., Burns, J.O., & Norman, M.L. 1992, ApJ, 395, 444

[Conway & Blanco 1995] Conway, J.E. & Blanco, P.R. 1995, ApJ, 449, L131

[Danzinger et al. 1979] Danziger, I.J., Fosbury, R.A.E., Goss, W.M., & Ekers, R.D. 1979, MNRAS, 188, 415

[Dondi & Ghisellini 1995] Dondi, L. & Ghisellini, G. 1995, MNRAS, 273, 583

[de Pater, Schloerb & Johnston 1985] de Pater, I., Schloerb, F.P., & Johnston, A.H. 1985, AJ, 90, 846

[de Vaucouleurs et al. 1991] de Vaucouleurs, G., de Vaucouleurs, A., Corwin, Jr., H.G., Buta, R.G., Paturel, G., & Fouque, P. 1991, 'Third Reference Catalog of Bright Galaxies' (Springer Verlag: New York)

[di Serego Alighieri et al. 1988] di Serego Alighieri, S., Binette, L., Courvoisier, T. J.-L., Fosbury, R.A.E., & Tadhunter, C.N. 1988, Nature, 334, 591

[Falke & Biermann 1996] Falke, H. & Biermann, P.L. 1996, Submitted to AA

[Falomo 1994] Falomo, R. 1995, ESO Messenger, no. 77, 49

[Falomo et al. 1995] Falomo, R., Ghisellini, G., Maraschi, L., Pian, E., Sambruna, R.M., Treves, A. & Scarpa, R. 1995, Adv. Space Res., 15, (5) 69

[Fanaroff & Riley 1974] Fanaroff, B.L. & Riley, J.M. 1974, MNRAS, 167, 31P

[Fichtel et al. 1994] Fichtel, C.E. et al. 1994, ApJS, 94, 551

[Filippenko 1985] Filippenko, A.V. 1985, ApJ, 289, 475

[Fosbury et al. 1990] Fosbury, R.A.E., di Serego Alighieri, S., Courvoisier, T. J.-L., Snijders, M.A.J., Tadhunter, C.N., Walsh, J., & Wilson, W. 1990, in 'Evolution in astrophysics: IUE astronomy in the era of new space missions', ESA SP 310, 513

[Fosbury et al. 1987] Fosbury, R.A.E., Bird, M.C., Nicholson, W., & Wall, J.V. 1987, MNRAS, 225, 761

[Fosbury *et al.* 1977] Fosbury, R.A.E., Mebold, U., Goss, W.M., & van Woerden, H. 1977, MNRAS, 179, 89

[Harmon *et al.* 1995] Harmon, B.A. *et al.* 1995, Nature, 374, 703

[Hirosawa 1991] Hirosawa, H. 1991, in 'Frontiers of VLBI' Ed. H. Hirabayashi *et al.* (Universal Academy Press: Tokyo), 21

[Hjellming & Rupen 1995] Hjellming, R.M. & Rupen, M.P 1995, Nature, 375, 464

[Hooimeyer *et al.* 1992] Hooimeyer, J.R.A., Schilizzi, R.T., Miley, G.K., & Barthel, P.D. 1992, AA, 261, 5

[Hui *et al.* 1993] Hui, X., Ford, H.C., Ciardullo, R., & Jacoby, G.H. 1993, ApJ, 414, 463

[Impey & Tapia 1988] Impey, C.D. & Tapia, S. 1988, ApJ, 333, 666

[Impey & Tapia 1990] Impey, C.D. & Tapia, S. 1990, ApJ, 354, 124

[Jauncey *et al.* 1989] Jauncey, D.L., Savage, A., Morabito, D.D., Preston, R.A., Nicolson, G.D., & Tzioumis, A.K. 1989, AJ, 98, 54

[Jennison 1958] Jennison, R.C. 1958, MNRAS, 118, 276

[Jones *et al.* 1996] Jones, D.L. *et al.* 1996, in 'IAU 175: Extragalactic Radio Sources' (Bologna), in press

[Jones, McAdam, & Reynolds 1994] Jones, P.A., McAdam, W.B., & Reynolds, J.E. 1994, MNRAS, 268, 602

[Junkes *et al.* 1993] Junkes, N., Haynes, R.F., Harnett, J.I., & Jauncey, D.L. 1993, AA, 269, 29

[Karzas & Latter 1961] Karzas, W. & Latter, R. 1961, ApJS, 6, 167

[Keel 1986] Keel, W.C. 1986, ApJ, 302, 296

[Keel & Windhorst 1991] Keel, W.C. & Windhorst, R.A. 1991, ApJ, 383, 135

[Kellermann & Pauliny-Toth 1969] Kellermann, K.I. & Pauliny-Toth, I.I.K. 1969, ApJ, 155, L71

[Kifune *et al.* 1996] Kifune T. *et al.* 1996, in 'Proc. 24th Int. Cosmic Ray Conf.' (Rome) in press

[King 1994] King, E.A. 1994, PhD thesis (University of Tasmania, Australia)

[Kinman 1976] Kinman, T.D. 1976, ApJ, 205, 1

[Landau & Lifshitz 1987] Landau, L.D. & Lifshitz, E.M. 1984, 'Fluid Mechanics' (Pergamon press: Oxford), chapter IX

[Lang 1986] Lang, K.R. 1986, 'Astrophysical Formulae' (Springer Verlag: Berlin), 26

[Levy et al. 1986] Levy, G.S. et al. 1986, Science, 234, 117

[Levinson & Blandford 1996] Levinson, A. & Blandford, R.D. 1996, ApJ, 456, L29

[Lin et al. 1995] Lin, Y.C. et al. 1995, ApJ, 442, 96

[Linfield et al. 1989] Linfield, R.P. et al. 1989, ApJ, 336, 1105

[Linfield et al. 1990] Linfield, R.P. et al. 1990, ApJ, 358, 350

[Lovell 1996] Lovel, J.E.J. 1996, PhD thesis in preparation (University of Tasmania, Australia)

[Lovell, McCulloch, & Jauncey 1995] Lovell, J.E.J., McCulloch, P.M., & Jauncey, D.L. 1995, in Proceedings of the IAU 173: 'Astrophysical Applications of Gravitational Lensing', Kluwer Academic Publishers, Eds.: C.S. Kochanek & J.N. Hewitt, in press

[Macchetto et al. 1991] Macchetto, F. et al. 1991, ApJ, 369, L55

[Marr et al. 1989] Marr, J.M., Backer, D.C., Wright, M.C.H., Readhead, A.C.S., & Moore, R. 1989, ApJ, 337, 671

[Meier 1996] Meier, D.L. 1996, ApJ, 459, 185

[Meier et al. 1993] Meier, D.L. et al. 1993, in 'Sub-arcsecond Radio Astronomy', eds. R.J. Davis & R.S. Booth (Cambridge: Cambridge University Press), 201

[Meier et al. 1989] Meier, D.L. et al. 1989, AJ, 98, 27

[Miley et al. 1981] Miley, G.K., Heckman, T.M., Butcher, H.R., & van Breugal, W.J.M. 1981, ApJ, 247, L5

[Mirabel & Rodriguez 1994] Mirabel, I.F. & Rodriguez, L.F. 1994, Nature, 371, 46

[Mollenbrock et al. 1996] Mollenbrock, G.A. et al. 1996, AJ, accepted for publication

[Morganti et al. 1993] Morganti, R., Killeen, N.E.B., & Tadhunter, C.N. 1993, MNRAS, 263, 1023

[Murphy 1993] Murphy, D.W. 1993, JPL interoffice memorandum, 'Model-fitting with RadioAstron'

[Murphy, Browne & Perley 1993] Murphy, D.W., Browne, I.W.A, & Perley, R.A. 1993, MNRAS, 264, 298

[Murphy et al. 1993] Murphy, D.W. et al. 1993, in 'Sub-arcsecond radio astronomy', Cambridge University Press, Eds.: R.J. Davis & R.S. Booth, 243

[Norris et al. 1990] Norris, R.P., Kesteven, M.J., Sramek, R.A., Wilson, W.E., Brooks, J.W., Calabretta, M.R., Ekers, R.D., Nelson, G.J., Sinclair, M.W., & Young, A.C. 1990, Proc. ASA, 8 (3), 252

[O'Dea, Baum, & Stanghellini 1991] O'Dea, C.P., Baum, S.A., & Stanghellini, C. 1991, ApJ, 380, 66

[Padovani & Urry 1992] Padovani, P. & Urry, C.M. 1992, ApJ, 387, 449

[Pearson 1991] Pearson, T.J. 1991, BAAS, 23, 991

[Pearson & Readhead 1988] Pearson, T.J. & Readhead, A.C.S. 1988, ApJ, 328, 114

[Pearson & Readhead 1984] Pearson, T.J. & Readhead, A.C.S. 1984, ARA&A, 22, 97

[Pearson & Zensus 1987] Pearson, T.J. & Zensus, J.A. 1987, in 'Superluminal Radio Sources' Eds: T.J. Pearson & J.A. Zensus (Cambridge University Press), 1

[Perley 1982] Perley, R.A. 1982, AJ, 87, 859

[Perley 1985] Perley, R.A. 1985, private communication in Preston et al. [1989]

[Peterson et al. 1976] Peterson, B.A., Jauncey, D.L., Wright, A.E., & Condon, J.J. 1976, ApJ, 207, L5

[Phillips & Mutel 1980] Phillips, R.B. & Mutel, R.L. 1980, ApJ, 244, 19

[Pica et al. 1988] Pica, A.J., Smith, A.G., Webb, J.R., Leacock, R.J., Clements, S., & Gombola, P.P. 1988, AJ, 96, 1215

[Polatidis et al. 1995] Polatidis, A.G. et al. 1995, ApJS, 98, 1

[Preston et al. 1989] Preston, R.A. et al. 1989, AJ, 98, 1

[Preston et al. 1985] Preston, R.A. et al. 1985, AJ, 90, 1599

[Preston et al. 1983] Preston, R.A., Wehrle, A.E., Morabito, D.D., Jauncey, D.L., Batty, M.J., Haynes, R.F., & Wright, A.E. 1983, ApJ, 266, L93

[Punch et al. 1992] Punch, M. et al., 1992, Nature 358, 477

[Reid et al. 1989] Reid, M.J., Biretta, J.A., Junor, W., Muxlow, T.W.B., & Spencer, R.E. 1989, ApJ, 336, 112

[Reynolds & Jauncey 1994] Reynolds, J.E. & Jauncey, D.L. 1994, IAU Circ. 6063

[Reynolds et al. 1994] Reynolds, J.E., Jauncey, D.L., Russell, J.L., King, E.A., McCulloch, P.M., Fey, A.L., & Johnston, K.J. 1994, AJ, 108, 725

[Rogers et al. 1983] Rogers, A.E. et al. 1983, Science, 219, 51

[Rogers et al. 1974] Rogers, A.E.E. et al. 1974, ApJ, 193, 293

[Romney 1995] Romney, J.D. 1995, in 'Very Long Baseline Interferometry and the VLBA', ASP conference series (Eds J.A. Zensus, P.J. Diamond, & P.J. Napier), 82, 17

[Rybicki & Lightman 1979] Rybicki, G.B. & Lightman A.P. 1979, 'Radiative Processes in Astrophysics' (John Wiley & Sons: New York)

[Salamon & Stecker 1994] Salamon, M. & Stecker, F.W. 1994, ApJ, 430, L21

[Sambruna et al. 1994] Sambruna, R.M., Barr, P., Giommi, P., Maraschi, L., Tagliaferri, G., & Treves, A. 1994, ApJS, 95, 371

[Savage 1976] Savage, A. 1975, MNRAS, 174, 259

[Schwab & Cotton 1983] Schwab, F. & Cotton, W. 1983, AJ, 88, 688

[Shepherd, Pearson & Taylor 1994] Shepherd, M.C., Pearson, T.J., & Taylor, G.B. 1994, BAAS, 26, 987

[Simkin, Robinson, & Sadler 1992] Simkin, S.M., Robinson, P., & Sadler, E.M. 1992, BAAS, 24, 727

[Simkin, Sadler, & Sault 1994] Simkin, S.M., Sadler, E.M., & Sault, R. 1994, BAAS, 26, 874

[Snellen et al. 1995] Snellen, I.A.G., Zhang, M., Schilizzi, R.T., Röttgering, H.J.A., de Bruyn, A.G., & Miley, G.K. 1995, AA, 300, 359

[Sparks, Biretta, & Macchetto 1994] Sparks, W.B., Biretta, J.A., & Macchetto, F. 1994, ApJS, 90, 909

[Stannard & McIlwrath 1982] Stannard, P. & McIlwrath, B.K. 1982, Nature, 298, 140

[Stanghellini et al. 1990] Stanghellini, C., Baum, S.A., O'Dea, C.P., & Morris, G.B. 1990, in 'Proc. Dwingeloo Workshop on Compact Steep Spectrum and GHz Peaked-Spectrum Radio Sources' ed. C. Fanti, R. Fanti, C.P. O'Dea & R.T. Schilizzi (Bologna: Istituto di Radioastronomia), 55

[Stanghellini et al. 1993] Stanghellini, C., O'Dea, C.P., Baum, S.A., & Laurikainen, E. 1993, ApJS, 88, 1

[Stickel, Meisenheimer, & Kühr 1994] Stickel, M., Meisenheimer, K., & Kühr, H. 1994, AASupp, 105, 211

[Sulentic et al. 1995] Sulentic, J.W., Marziani, P., Zwitter, T., & Calvani, M. 1995, ApJ, 438, L1

[Tadhunter et al. 1988] Tadhunter, C.N., Fosbury, R.A.E., di Serego Alighieri, S., Bland, J., Danziger, I.J., Goss, W.M., McAdam, W.B., & Snijders, M.A.J. 1988, MNRAS, 235, 403

[Tadhunter et al. 1987] Tadhunter, C.N., Fosbury, R.A.E., Binette, L., Danziger, I.J., & Robinson, A. 1987, Nature, 325, 504

[Tanzi et al. 1986] Tanzi, E.G., Barr, P., Bouchet, P., Chiappetti, L., Cristiani, S., Falomo, R., Giommi, P., Maraschi, L., & Treves, A. 1986, ApJ, 311, L13

[Thompson, Crane, & MacKay 1995] Thompson, R.C., Crane, P., & MacKay, C.D. 1995, ApJ, 446, L93

[Thompson et al. 1995] Thompson, D.J. et al. 1995, ApJS, 101, 259

[Tingay et al. 1994] Tingay, S.J. et al. 1994 Aust.J.Phys. 47, 619

[Tingay et al. 1995] Tingay, S.J. et al. 1995, Nature, 374, 141

[Treves et al. 1993] Treves, A., Belloni, T., Falomo, R., Fink, H., Maraschi, L., Sambruna, R.M., Tagliaferri, G., & Zimmermann, H.U. 1993, ApJ, 406, 447

[Tzioumis 1987] Tzioumis, A.K. 1987, PhD thesis (University of Sydney, Australia)

[Tzioumis et al. 1989] Tzioumis, A.K. et al. 1989, AJ, 98, 36

[Ulvestad & Johnston 1984] Ulvestad, J.S. & Johnston, K.J. 1984, AJ, 89, 189

[Ulvestad, Johnston, & Weiler 1983] Ulvestad, J.S., Johnston, K.J., & Weiler, K.W. 1983, ApJ, 266, 18

[Unwin et al. 1985] Unwin, S.C., Cohen, M.H., Biretta, A. Pearson, T.J., Seilstad, G.A., Walker, R.C., Simon, R.S., & Linfield, R.P. 1985, ApJ, 289, 109

[van Breugal et al. 1985] van Breugal, W., Miley, G., Heckman, T., Butcher, H., & Bridle, A. 1985, ApJ, 290, 496

[Vermeulen & Cohen 1994] Vermeulen, R.C. & Cohen, M.H. 1994, ApJ, 430, 467

[Vermeulen, Readhead, & Backer 1994] Vermeulen, R.C., Readhead, A.C.S., & Backer, D.C. 1994, ApJ, 430, L41

[Véron-Cetty et al. 1995] Véron-Cetty, M.P., Woltjer, L., Ekers, R.D., & Staveley-Smith, L. 1995, AA, 297, L79

[Vestrand et al. 1996] Vestrand, W.T., Stacy, J.G., Mukherjee, R., & Streekumar, P. 1996, IAU Circ. 6348

[Visvanathan & Griersmith 1977] Visvanathan, N. & Griersmith, D. 1977, ApJ, 215, 759

[von Montigny et al. 1995a] von Montigny, C. et al. 1995, ApJ, 440, 525

[von Montigny et al. 1995b] von Montigny, C. et al. 1995, AA, 299, 680

[Wade et al. 1971] Wade, C.M., Hjellming, R.M., Kellermann, K.I., & Wardle, J.F.C. 1971, ApJ, 170, L11

[Walker, Benson, & Unwin 1987] Walker, R.C., Benson, J.M., & Unwin, S.C. 1987, in 'Superluminal Radio Sources', Eds J.A. Zensus & T.J. Pearson (Cambridge University Press: Cambridge), 48

[Walker, Romney, & Benson 1984] Walker, R.C., Romney, J.D., & Benson, J.M. 1984, ApJ, 430, L45

[Wall 1994] Wall, J.V. 1994, Aust.J.Phys., 47, 625

[Webb *et al.* 1988] Webb, J.R., Smith, A.G., Leacock, R.J., Fitzgibbons, G.L., Gombala, P.P., & Shepherd, D.W. 1988, AJ, 95, 374

[Westerlund & Smith 1966] Westerlund, B.E. & Smith, L.F. 1966, Aust.J.Phys., 19, 181

[Wietfeldt *et al.* 1991] Wietfeldt, R.D. *et al.* 1991, in 'Frontiers of VLBI', Eds H. Hirabayashi, M. Inoue, & H. Kobayashi (Universal Academy: Tokyo), 21

[Wilson *et al.* 1994] Wilson, C.A. *et al.* 1994, IAU Circ 6056

[Xu *et al.* 1995] Xu, W., Readhead, A.C.S., Pearson, T.J., Polatidis, A.G., & Wilkinson, P.N. 1995, ApJS, 99, 279